

# Elastic Interactions of Cellular Force Patterns

## Dissertation

zur Erlangung des akademischen Grades  
Doktor der Naturwissenschaften (Dr. rer. nat.)  
in der Wissenschaftsdisziplin Theoretische Physik

eingereicht an der  
Mathematisch–Naturwissenschaftlichen Fakultät der Universität Potsdam

angefertigt am  
Max–Planck–Institut für Kolloid- und Grenzflächenforschung in Potsdam

von

**Ilka Bettina Bischofs**

geboren am 12. Oktober 1976 in Frankfurt am Main

Potsdam, im Juli 2004



# Abstract

Adherent cells constantly collect information about the mechanical properties of their extracellular environment by actively pulling on it through cell–matrix contacts, which act as mechanosensors. In recent years, the sophisticated use of elastic substrates has shown that cells respond very sensitively to changes in effective stiffness in their environment, which results in a reorganization of the cytoskeleton in response to mechanical input.

We develop a theoretical model to predict cellular self-organization in soft materials on a coarse grained level. Although cell organization in principle results from complex regulatory events inside the cell, the typical response to mechanical input seems to be a simple preference for large effective stiffness, possibly because force is more efficiently generated in a stiffer environment. The term effective stiffness comprises effects of both rigidity and prestrain in the environment. This observation can be turned into an optimization principle in elasticity theory. By specifying the cellular probing force pattern and by modeling the environment as a linear elastic medium, one can predict preferred cell orientation and position.

Various examples for cell organization, which are of large practical interest, are considered theoretically: cells in external strain fields and cells close to boundaries or interfaces for different sample geometries and boundary conditions. For this purpose the elastic equations are solved exactly for an infinite space, an elastic half space and the elastic sphere. The predictions of the model are in excellent agreement with experiments for fibroblast cells, both on elastic substrates and in hydrogels.

Mechanically active cells like fibroblasts could also interact elastically with each other. We calculate the optimal structures on elastic substrates as a function of material properties, cell density and the geometry of cell positioning, respectively, that allows each cell to maximize the effective stiffness in its environment due to the traction of all the other cells. Finally, we apply Monte Carlo simulations to study the effect of noise on cellular structure formation.

The model not only contributes to a better understanding of many physiological situations. In the future it could also be used for biomedical applications to optimize protocols for artificial tissues with respect to sample geometry, boundary condition, material properties or cell density.



# Zusammenfassung

Gewebezellen sammeln ständig Informationen über die mechanischen Eigenschaften ihrer Umgebung, indem sie aktiv an dieser ziehen. Diese Kräfte werden an Zell–Matrix–Kontakten übertragen, die als Mechanosensoren fungieren. Jüngste Experimente mit Zellen auf elastischen Substraten zeigen, dass Zellen sehr empfindlich auf Veränderungen der effektiven Steifigkeit ihrer Umgebung reagieren, die zu einer Reorganisation des Zytoskeletts führen können.

In dieser Arbeit wird ein theoretisches Model entwickelt, um die Selbstorganisation von Zellen in weichen Materialien vorherzusagen. Obwohl das Zellverhalten durch komplexe regulatorische Vorgänge in der Zelle gesteuert wird, scheint die typische Antwort von Zellen auf mechanische Reize eine einfache Präferenz für große effektive Steifigkeit der Umgebung zu sein, möglicherweise weil in einer steiferen Umgebung Kräfte an den Kontakten effektiver aufgebaut werden können. Der Begriff Steifigkeit umfasst dabei sowohl Effekte, die durch größere Härte als auch durch elastische Verzerrungsfelder in der Umgebung verursacht werden. Diese Beobachtung kann man als ein Extremalprinzip in der Elastizitätstheorie formulieren. Indem man das zelluläre Kraftmuster spezifiziert, mit dem Zellen mit ihrer Umgebung wechselwirken, und die Umgebung selbst als linear elastisches Material modelliert, kann damit die optimale Orientierung und Position von Zellen vorhergesagt werden.

Es werden mehrere praktisch relevante Beispiele für Zellorganisation theoretisch betrachtet: Zellen in externen Spannungsfeldern und Zellen in der Nähe von Grenzflächen für verschiedene Geometrien und Randbedingungen des elastischen Mediums. Dafür werden die entsprechenden elastischen Randwertprobleme in Vollraum, Halbraum und Kugel exakt gelöst. Die Vorhersagen des Models stimmen hervorragend mit experimentellen Befunden für Fibroblastzellen überein, sowohl auf elastischen Substraten als auch in physiologischen Hydrogelen.

Mechanisch aktive Zellen wie Fibroblasten können auch elastisch miteinander wechselwirken. Es werden daher optimale Strukturen als Funktion von Materialeigenschaften und Zelldichte bzw. der Geometrie der Zellpositionen berechnet. Schließlich wird mit Hilfe von Monte Carlo Simulationen der Einfluss stochastischer Störungen auf die Strukturbildung untersucht.

Das vorliegende Model trägt nicht nur zu einem besseren Verständnis von vielen physiologischen Situationen bei, sondern könnte in Zukunft auch für biomedizinische Anwendungen benutzt werden, um zum Beispiel Protokolle für künstliche Gewebe im Bezug auf Substratgeometrie, Randbedingungen, Materialeigenschaften oder Zelldichte zu optimieren.



# Contents

<b>List of Figures</b>	<b>ix</b>
<b>List of Symbols</b>	<b>xi</b>
<b>1 Introduction</b>	<b>1</b>
1.1 Self-Organization of Cells and Tissues . . . . .	1
1.2 Cells, Forces and Elasticity . . . . .	4
1.2.1 Cells in Soft Environments: Observations . . . . .	4
1.2.2 Force, Regulation and Mechanosensation . . . . .	6
1.3 Elastic Interactions . . . . .	9
1.4 Objective, Outline and Main Results . . . . .	11
<b>2 Modeling</b>	<b>13</b>
2.1 Basic Concepts . . . . .	13
2.1.1 Effective Stiffness and Linear Elasticity Theory . . . . .	13
2.1.2 Force Multipoles . . . . .	17
2.2 Elastic Interactions of Defects . . . . .	19
2.3 Elastic Interactions of Cells . . . . .	21
2.3.1 An Extremum Principle . . . . .	21
2.3.2 Contributions to the Effective Stiffness . . . . .	23
2.3.3 Mechanosensing and Effective Stiffness . . . . .	25
2.4 Summary . . . . .	31
<b>3 Examples of Cell Organization</b>	<b>33</b>
3.1 External Strain . . . . .	33
3.2 Sample Boundaries: The Elastic Half Space . . . . .	35
3.2.1 The Elastic Boundary Value Problem . . . . .	36
3.2.2 Interactions with the Boundary . . . . .	39
3.3 Sample Geometry: The Elastic Sphere . . . . .	41
3.3.1 The Elastic Boundary Value Problem . . . . .	41
3.3.2 Effects in an Elastic Sphere . . . . .	46
3.4 Summary and Discussion . . . . .	48

<b>4</b>	<b>Elastic Interactions of Cells</b>	<b>51</b>
4.1	Elastic Interactions of Force Dipoles . . . . .	51
4.1.1	Dipoles on Elastic Half Space . . . . .	53
4.1.2	Dipoles in Elastic Full Space . . . . .	56
4.1.3	Discussion: A Biomechanical Feedback Loop . . . . .	58
4.2	Strings of Dipoles . . . . .	59
4.2.1	Single String . . . . .	60
4.2.2	Interactions with Strings . . . . .	61
4.2.3	Discussion . . . . .	69
<b>5</b>	<b>Structures on Elastic Substrates</b>	<b>71</b>
5.1	Structures on Micropatterned Substrates . . . . .	71
5.1.1	Optimal Lattice Structures . . . . .	72
5.1.2	Effect of Noise: Monte Carlo Simulations . . . . .	81
5.2	Structures for Positional Disorder . . . . .	88
5.3	Discussion and Outlook . . . . .	96
	<b>Bibliography</b>	<b>101</b>
	<b>Acknowledgements</b>	<b>113</b>

# List of Figures

1.1	Self-organizing principles of adherent cells . . . . .	2
1.2	Examples for cell organization in soft media . . . . .	5
1.3	Fluorescence staining of a fibroblast and schematic zoom into cell–matrix contacts . . . . .	8
1.4	Comparison of classical defects and cells interacting with their elastic environment. . . . .	10
2.1	Phenomenological modeling approach . . . . .	14
2.2	Schematic representation of defect and cellular force dipoles . . .	18
2.3	Simple model for force build-up at cell–matrix contacts . . . . .	27
2.4	Force build-up dynamics at a single bond . . . . .	29
3.1	$\Delta W^e$ in a homogeneous strain field. . . . .	34
3.2	Image fields $\vec{u}^b$ in an elastic half space . . . . .	38
3.3	$\Delta W^b$ (angular dependence) in an elastic half space . . . . .	40
3.4	Cartoon of cell organization close to boundaries or interfaces. . .	42
3.5	Deformation of an elastic sphere by a contraction dipole. . . . .	45
3.6	$\Delta W^b$ (radial dependence) in an elastic sphere. . . . .	47
4.1	Force pattern of a fibroblast . . . . .	52
4.2	Density plots of $\Delta W^{PP'}$ for dipoles on an elastic half space (2D)	54
4.3	Basic structures for force dipoles on an elastic half space. . . . .	55
4.4	Density plots of $\Delta W^{PP'}$ for dipoles in an infinite medium (3D) .	57
4.5	Biomechanical feed-back loop for cell alignment . . . . .	58
4.6	Optimal configurations for force dipoles in 2D and 3D . . . . .	59
4.7	Geometric sketch of strings and stacks . . . . .	61
4.8	Contour used for integration in the Poisson sum rule . . . . .	63
4.9	$\Delta w^{\parallel}$ for string–string interactions . . . . .	65
4.10	$\Delta w^{\parallel}$ -oscillations with offset between strings . . . . .	66
4.11	$\Delta w^{\perp}$ for string-stack interactions . . . . .	68
5.1	Sketch of different lattice structures . . . . .	75
5.2	$w^{\text{tot}}(\nu)$ for structures in Fig. 5.1 . . . . .	77
5.3	Sketch of the T-lattice and the Herringbone pattern . . . . .	79

5.4	$v^{\text{tot}}(\nu)$ for the structures in Fig. 5.3 . . . . .	80
5.5	Monte Carlo snapshots of force dipoles on a square lattice. . . . .	83
5.6	Monte Carlo snapshots for force dipoles on a hexagonal lattice. . . . .	84
5.7	$\langle p \rangle$ as a function of $T^*$ for dipoles on a square and hexagonal lattice . . . . .	86
5.8	Monte Carlo snapshots for dipoles on a disordered square lattice . . . . .	87
5.9	$g(r)$ for various values of $\rho^*$ . . . . .	90
5.10	Monte Carlo snapshots for dipoles with disordered positions . . . . .	92
5.11	$\langle p \rangle$ as a function of $\rho^*$ for various values of $\nu$ and $T^*$ . . . . .	93
5.12	Schematic phase–diagram for structure formation on elastic sub- strates . . . . .	94
5.13	Collective effects in 3D elastic substrates . . . . .	99

# List of Symbols

$u_{ij}$	elastic strain tensor
$\vec{u}, (u_i)$	(component of) the displacement vector
$\sigma_{ij}$	elastic stress tensor
$C_{ijkl}$	elastic constant tensor
$E$	Young modulus
$\nu$	Poisson ratio
$c$	elastic constant, page 17
$\Lambda$	elastic constant, page 17
$P_{ij}$	force dipole tensor
$W$	effective interaction potential for cells, inverse of effective stiffness, page 21
$V^t$	total potential energy for a defect in an elastic medium
$G_{ij}^\infty$	Green tensor in infinite space, see equation (3.3)
$G_{ij}^{\text{im}}$	image Green tensor of isotropic half space, see equation (3.7)
$G_{ij}^{2D}$	$xy$ -Green tensor on elastic half space, see equation (4.1)
$a_1^\infty$	constant in $G_{ij}^\infty$ , see equation (3.4)
$a_2^\infty$	constant in $G_{ij}^\infty$ , see equation (3.4)
$a_1$	constant in $G_{ij}^{2D}$ , see equation (4.2)
$a_2$	constant in $G_{ij}^{2D}$ , see equation (4.2)
$\rho^*$	reduced density, see equation (5.9)
$T^*$	reduced temperature of MC simulation, see equation (5.5)

$\langle \rho \rangle$  absolute average particle density

$\langle p \rangle$  averaged nematic order parameter, see equation (5.7)

# Chapter 1

## Introduction

### 1.1 Self-Organization of Cells and Tissues

Cells are the basic units of life and the first primordial cells existed on earth about 3.5 billion years ago. During the course of evolution life took ever more complex forms and about 1.5 billion years ago, the first multi-celled eukaryotes developed. Today the human body comprises about  $10^{13}$  cells with more than 200 different cell types [1]. All complex organisms are hierarchically structured: the organism is composed of several organs each fulfilling a specialized function. Organs contain specialized tissues and a tissue consists of cells of different types as well as the extracellular matrix (ECM). The ECM is a network of protein filaments (like collagen or fibronectin) secreted by the tissue's resident cells and is constantly remodeled by cells. What distinguishes a clot of cells and matrix from a tissue is the well defined organization of cells and ECM, which is closely associated with the tissue's function. Within a tissue cells adopt well defined morphologies, positions and orientations, and loss of cell organization leads to tissue malfunction.

Tissues form *de novo* during embryonic development. In adult organisms, major tissue reconstructing and replacement occurs after injury. Moreover, tissue is constantly remodeled by cells, e.g. fibroblasts remodel the connective tissue and osteoblasts and osteoclasts the bone tissue, respectively. The goal of the emerging field of tissue engineering is the construction, repair or replacement of damaged tissue, which may take place in the body or a bioreactor [2]. The key question in understanding—and also technologically exploiting—tissue formation is how cells communicate with each other and the environment to build up organized structures. The research in cell and tissue organization principles has a long history and today we know that cells communicate through many different channels. Fig. 1.1 shows an overview of known factors influencing cell and tissue organization.

The best studied way for cells to exchange specific information is via

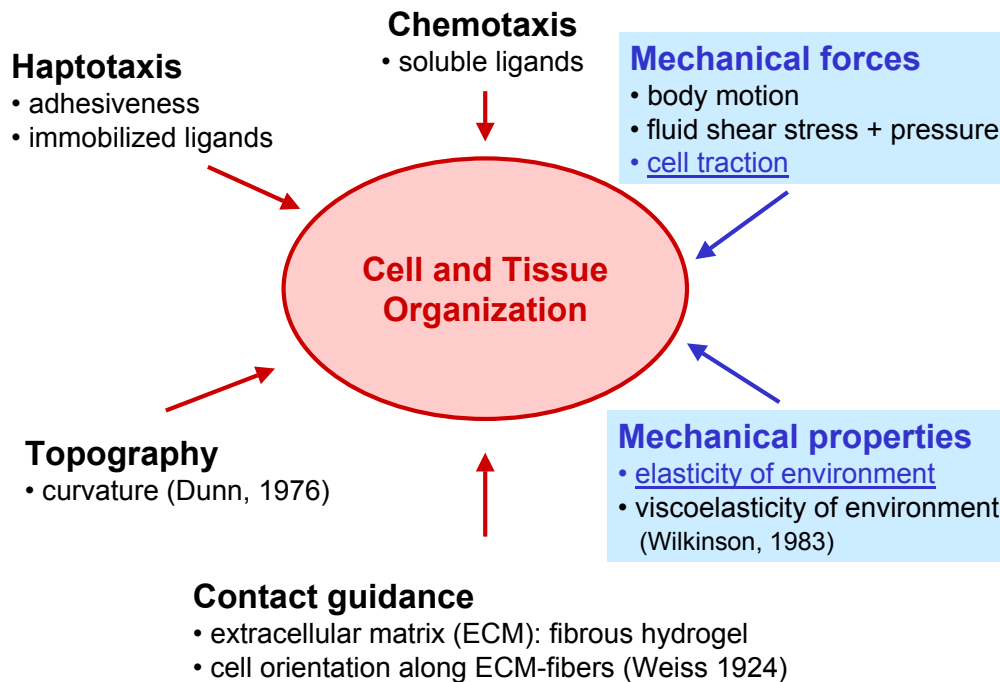


Figure 1.1: Self-organization principles of adherent cells. The focus of this work is on cell and tissue self-organization driven by the mechanical properties of the environment and through cellular traction forces.

release and uptake of biochemical molecules at specific cell receptors [3]. Gradients in ligand concentration encode spatial information, e.g. in development morphogen gradients can induce spatially dependent cell differentiation [1]. Moreover, attractor or repellent gradients can induce directed cell locomotion towards or away from the emitter (chemotaxis). For instance, after wounding neutrophils and monocytes crawl into the wounded site attracted by a variety of chemotactic signals released by platelets. In case of an infection, they are attracted by chemotactic signals originating from the presence of pathogens [4].

In the early 20th century biologists favored the idea of cell–cell communications via diffusible chemicals and it was mainly through the work of Peter Weiss that biologists became aware of the importance of biophysical signals originating from the environment, in particular the ECM. Weiss observed that cells preferentially orient along ECM-fibers, an organization principle he termed *contact guidance* [5,6]. Moreover, he observed that two tissue explants “condense” the collagen gel between them into aligned parallel fiber bundles and that cells leaving the explants migrate and orient along the aligned fibers (“two center effect”) [5]. Contact guidance therefore could serve both as a cue for organization on cellular scales and as a large-scale organization principle

in tissue development by guiding motile cells along aligned ECM-bundles [5]. Although Weiss associated contact guidance with differential adhesiveness and interfacial tensions [6, 7], the term has now gained a strong topographical connotation: in 1976 Dunn conclusively demonstrated that cells react to surface curvature and prefer to align along the axis of minimal curvature, where minimal distortion of the cytoskeleton occurs [8, 9]. This mechanism also favors orientation of cells along thick fiber bundles. However, contact guidance provides only a bidirectional cue for cell migration. A unidirectional cue could originate from spatial variations in adhesiveness (haptotaxis) [10]. Haptotaxis could be supplemented by specific biochemical information encoded in an inhomogeneous spatial distribution of immobilized ligands. Contact guidance and haptotaxis were the first cell organizing principles discovered for adherent cells that attributed a role to biophysical cues in the environment.

Moreover, it has long been implied that adherent cells could also respond to mechanical properties of their environment [11]. However, for a long time this idea received little attention, mainly because convincing model systems have been lacking. During recent years the sophisticated use of elastic substrates has provided strong evidence that cells respond to purely elastic features in their environment, including rigidity, rigidity gradients and pre-strain in the environment [12–14]. Recent work using tools from molecular biology to study biochemical signaling now provides strong evidence that cells are able to actively sense and respond to the mechanical properties of their environment [15–17].

Finally, it is well known—especially in the medical and bioengineering communities—that mechanical forces play a major role in tissue development, remodeling and reconstruction. Cells in the body are constantly subject to external forces like those induced by body motion or fluid shear stress. These forces are essential to ensure proper functioning for many different tissues including bone, lung and blood capillaries. Besides, anchorage-dependent cells like fibroblasts in the connective tissue show a remarkable degree of mechanical activity. The large traction forces exerted by fibroblasts were first quantified by Harris in 1980, pioneering the elastic substrate method [18]. Fibroblasts are believed to maintain the integrity of connective tissue by mechanically pulling on the collagen fibers. Moreover, they are an integral part of the wound contraction process. Harris and coworkers also noticed that cells react to mechanical changes in their environment caused by traction of other cells. Since cells align along topographical features in their environment, they suggested that cells react to traction-induced reorganization of collagen fibers via contact guidance. In this way they reinterpreted the Weiss two center effect, as caused by traction induced fiber rearrangement and not by a matrix compaction due to a local dehydration of the matrix through cells. This mechanism therefore amounts to a mechanical interaction of cells [19, 20].

## 1.2 Cells, Forces and Elasticity

### 1.2.1 Cells in Soft Environments: Observations

While much attention is focused on biochemistry for the design of artificial tissues, physical cues like topography, force or the mechanical properties of the environment might be equally important for cellular decision making. During recent years, rapid advances in materials science, including the development of microcontact printing, soft lithography, micro-fluidics and nano-technology, improved the control of cues in the micro-environment of adherent cells and thereby provided new tools to study the basic principles of cell organization and to design new artificial and biomimetic environments for cells. The development of technologies to control surface chemistry and topography has allowed to systematically study their effects on cell organization [21–23]. In contrast, the influence of substrate mechanics on cell organization has been appreciated by a wider community only very recently and much less is known about it. A systematic study of substrate elasticity on cell behavior requires new technologies to create substrates with well defined mechanics on micro- and mesoscale in combination with accurate measurement methods to quantify the local mechanical properties of the substrates on the microscale [24]. Today, three materials are commonly used as model substrates to study the effects of substrate elasticity on cell organization: polyacrylamide (PAAM), polydimethylsiloxane (PDMS) and agarose gels. All materials are synthetic hydrogels and by adjusting the degree of cross-linking their mechanical properties can be easily tuned within and beyond the physiologically relevant rigidity ranges of sub-kPa (nerve tissue) up to several MPa (pressurized arteries). In order to promote cell adhesion, the gel surfaces have to be modified, usually by covalent modification with specific ligands, since these surfaces usually are resistant to protein absorption from solution [24]. This allows to vary mechanics independently from surface chemistry.

The first strong evidence that substrate compliance could be used to modulate cell behavior came from Yu-li Wang’s group in 1997 [12]. They observed that cell morphology changed remarkably when reducing the substrate rigidity of a PAAM gel. In Fig. 1.2 a) and b) we show the typical change of fibroblast morphology from a round unspread cell on a very soft PAAM substrate to a well spread cell morphology with several distinct adhesion sites on a stiff substrate. Note the reorganization of the actin cytoskeleton (stained in red), which on very soft substrates is localized beneath the cell membrane in a cortical shell (similarly to non-adherent cells). On stiffer substrates long straight actin bundles (*stress fibers*) form, which run straight through the cytoplasm, often connecting two adhesion sites. The distinct morphology change was first observed in Ref. [12] for endothelial cells and fibroblasts and recently a

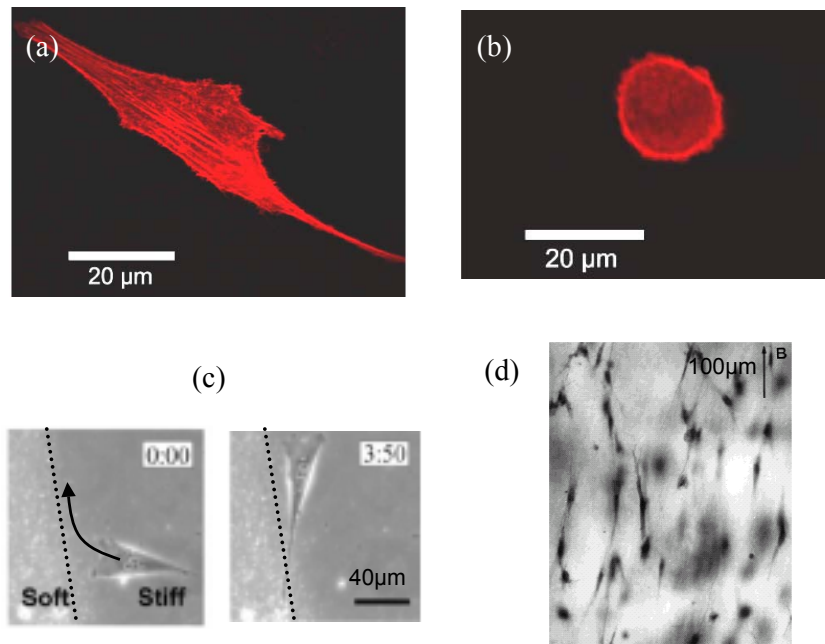


Figure 1.2: Examples for cell organization in soft media. (a, b) Cell morphology on elastic substrates depends on substrate rigidity. Images from Jens Gerdemann, University of Leipzig, Germany. (a) On stiff substrates cells spread and actin organizes to form stress-fibers typically connecting two adhesion sites. (b) Fibroblasts on a very soft PAAM gel are round and actin localizes beneath the cell membrane to form a cortical shell similar to non-adherent cells. (c) Durotaxis: cells respond to rigidity gradients. In a step gradient fibroblasts migrate from the soft to stiff side, but reorient to move along the boundary when placed on the stiff side as shown here [13]. (d) Cells in collagen gels orient along the direction of external strain [26].

similar observation has been reported for vascular smooth muscle cells (VSMC) by Dennis Discher's group [25].

Wang's group also showed that migrating cells respond to rigidity gradients and tensile strain in the substrate [13]. They termed this phenomenon *durotaxis*. In the vicinity of a step gradient in rigidity, fibroblasts migrated from the soft to the stiff side. However, cells on the stiff part did not cross over to the soft side, but rather reoriented by 90 degrees to move along the interface as shown in Fig. 1.2c). Moreover, by gently pulling or pushing the substrate with a micro-needle, the direction of locomoting cells could be reversed through substrate strain.

Very recently, a lot of progress has been made in the field through the application of micro-fabrication techniques to control the mechanical proper-

ties of the substrate on the micron scale. Joyce Wong was able to modulate substrate compliance of elastic substrates on a micron scale using a combination of photopolymerization and micropatterning/microfluidics tools, which allows for spatial control of the degree of gel crosslinking [14,27]. Her lab observed durotaxis for VSMCs on a continuous radial gradient substrate and also observed an accumulation of cells on the stiff parts of the gel [14]. Christopher Chen's lab created an orientational variation in compliance by culturing cells on a bed of small compliant ellipsoidal posts of PDMS [28]. They observed that cells preferentially orient along the long axis of the posts [29]. In this case however, topography may also contribute to the orientation effect because of the anisotropic post shape. Mathis Riehle used micro-fabrication to create an angular anisotropy in rigidity in a compound gel by pouring a soft gel on top of a topographically structured stiffer gel. Cells aligned along the stiffer lines, when lines were separated by  $25\mu\text{m}$  or more [30]. Taken together these experimental results provide strong evidence that cells respond to the mechanical properties of their environment. While more systematic studies are clearly needed, it appears that many cell-types show similar phenomena with a common dependence on substrate properties.

Interestingly, similar observations have been reported numerous times also for tissue cells in physiological hydrogels. In 1979 Eugene Bell and coworkers introduced 3D collagen assays as model systems for studying tissue equivalents [31]. For fibroblasts in collagen gels, they not only found that traction considerably contracts the gel, but also reported orientational effects: cells align along the direction of pull between fixed points and parallel to free surfaces [31]. As shown in Fig. 1.2d), when a collagen gel is stretched uniaxially, cells polarize in the direction of principal strain [26]. Moreover, cells align in a nose-to-tail configuration, thus forming strings running in parallel to the direction of external strain. If a collagen gel is cut perpendicular to the direction of tensile strain and if cells are present in sufficient numbers, they round up and reorient parallel to the free surface introduced [32].

### 1.2.2 Force, Regulation and Mechanosensation

How do adherent cells respond to mechanics? This question is at the heart of understanding cellular self-organization due to mechanical effects on a sub-cellular level. Moreover, it is also of interest to cell biologists interested in cell motility, which is an important process involved e.g. in development and metastasis. In order for the cell to interact with the substrate mechanically there must be forces involved.

In 1980 Harris and coworkers succeeded in giving a first estimate of cellular traction forces by studying cells on thin cross-linked polymer films, which buckle under the action of cellular tractions due to their small thickness [18]

(see also Fig. 1.4, left panel). They found an inverse relationship between the degree of cellular motility and the magnitude of overall cellular forces. For instance, they estimated that fibroblasts exert 100-1000 times larger forces than actually needed for cell locomotion and concluded that these large cellular forces must be required to fulfill the cell's specific function in the organism. Clearly, force is important for many physiological processes including cell locomotion, wound contraction, tissue remodeling or body motion.

During recent years, the elastic substrate method for traction force measurements has been improved considerably [33, 34]. In particular, it turned out that many cell types from higher organisms exert forces in a highly non-homogeneous fashion, i.e. localized at discrete adhesion spots [16]. These discrete cell-matrix contacts preferentially localize to the cell periphery. Cell-matrix contacts are based on transmembrane proteins from the integrin family, which bind to the RGD-motif presented by several extracellular ligands, including collagen, fibronectin and vitronectin. On the cytoplasmic side they connect to the actin cytoskeleton via linker proteins like talin or  $\alpha$ -actinin. Since integrins connect to both the extracellular matrix and the actin cytoskeleton, they can transmit internal forces to the environment and external forces to the cell. According to their location, size and maturation cell-matrix contacts are classified into focal complexes ( $< 1\mu\text{m}^2$ ), focal adhesions and fibrillar adhesions [35]. The dynamics of cell-matrix contacts is a subject of much current research [36]. Anchorage-dependent cells constantly assemble and disassemble focal adhesions, thereby probing the mechanical properties of their environment. Initial focal adhesions (*focal complexes*) are local processes based on integrin clustering. If initial clustering is stabilized by the properties of the extracellular environment, focal complexes can mature into focal adhesions. In this case, they connect to the actin cytoskeleton and a contractile force pattern builds up that is actively generated by myosin II molecular motors interacting with the actin cytoskeleton. Often one bundle of actin filaments (*stress fiber*) connects two focal adhesions that leads to a pinch-like force pattern. In some sense, stress fibers act like little cellular muscles and indeed, cross-striation, a characteristic feature of skeletal muscle cells, has been observed for stress fibers by staining for  $\alpha$ -actinin.

Using a new variant of traction force measurements, involving micro-patterned elastic substrates, individual forces exerted at single focal adhesions could be resolved [16, 37]. It was found that fibroblasts typically exert forces of 10 nN at mature focal adhesions [16, 37]. Using a bed of flexible micro-needles, similar values were found for smooth muscle cells [28]. Since adherent cells can have up to hundreds of focal adhesions, the overall force exerted by the cell can amount to  $\mu\text{N}$ . The forces exerted by cells on their environment result from non-equilibrium processes inside the cell and are *actively* generated by myosin-II molecular motors interacting with the actin cytoskeleton. Myosin

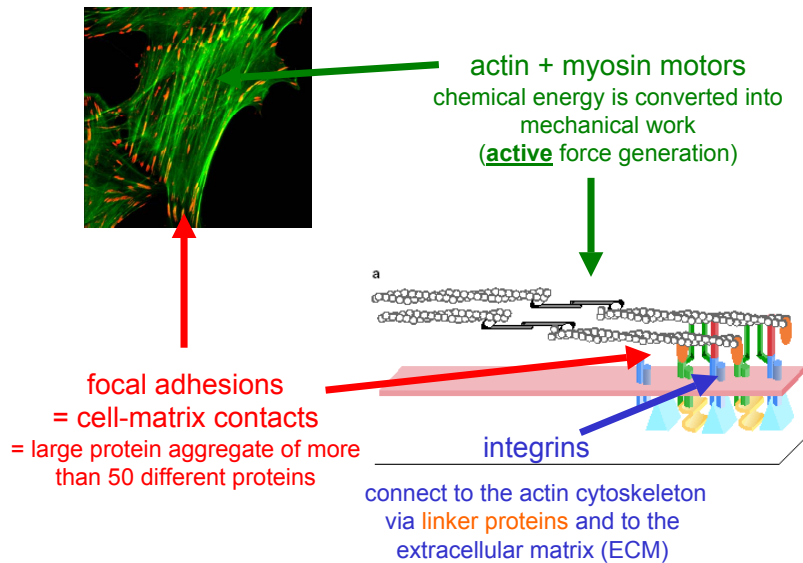


Figure 1.3: Left: Fluorescence staining of an adherent fibroblast with actin (green) and the focal adhesion protein vinculin (red). Numerous stress-fibers connecting two focal adhesions are clearly visible. Stress-fibers cause a pinched force pattern. Image: Weizman Institute, Israel. Right: Schematic zoom into a cell-matrix contact: force is actively generated by myosin II molecular motors interacting with actin filaments. Force is transmitted to the extracellular environment at cell-matrix contacts. Cell-matrix contacts contain numerous proteins with different functions and are spots of high signaling activity. Cell-matrix contacts have been shown to act as mechanosensors. Cartoon taken from Ref. [39].

motors convert chemical energy in form of the cellular fuel ATP into mechanical work. As part of stress fibers, they are known to be activated by signals from focal adhesions, in particular by the small GTPase RhoA. Since typical forces produced by molecular motors are in the pN-range [38], there must be up to  $10^6$  myosin II molecular motors contributing to overall cell traction. In Fig. 1.3 we show an image of an adherent fibroblast with numerous contractile stress fibers usually connecting two focal adhesions. The actin cytoskeleton is stained in green and the focal adhesion protein vinculin is stained in red.

A growing body of evidence suggests that focal adhesions act as mechanosensors which directly feed into cellular regulation [36]. In particular, it has been shown that application of external force leads to growth of focal adhesions and therefore to strong signaling activity [15, 17, 40]. The same aggregation has been found for mature focal adhesions under internally gen-

erated force [16, 28, 37], suggesting that focal adhesions act as mechanosensors that convert force into biochemistry and vice versa. Therefore, the mechanical activity of cells is not only related to the physiological function of their specific cell type, as Harris and coworkers concluded from their first traction force measurements [18], but is also a general way to collect information about the mechanical properties of the environment (*active mechanosensing*). There is strong evidence that this mechanism is involved in many important physiological situations, including tissue maintenance, wound healing, angiogenesis, development and metastasis [41–43]. Although focal adhesions are characteristic for cells cultured on flat and rigid substrates, cells in a soft environment develop similar cell-matrix contacts which presumably have the same mechanosensory function [44]. As a result of active mechanosensing at cell-matrix contacts, cells remodel their contacts and cytoskeleton. In particular, they might change position and become polarized in a certain direction, depending on the mechanical properties of their environment.

### 1.3 Elastic Interactions

In order for the cell to learn about its mechanical environment, there has to be some kind of interaction of the cell with the elastic medium. From a physicist's point of view, *elastic interactions* are very well known from the theory of point defects in traditional condensed matter materials, including hydrogen in metal [45], atoms adsorbed to crystal faces [46] and intercalation compounds [47]. Indeed, Fig. 1.4 suggests that there exists a strong analogy between a fibroblast distorting a soft elastic substrate and a defect-atom distorting its elastic environment.

The interaction of a classical defect with its elastic environment is specified by a defect-substrate interaction potential, which might originate from e.g. Born repulsion or van der Waals interactions. Independent of the exact interaction mechanism, the basic nature of the interaction is reflected by the specific *force pattern* exerted by the defect on the environment. The equilibrium configuration follows by minimizing the sum of the elastic energy of the strained medium and the direct interaction energy between defect and elastic environment. This results in an indirect, *elastic interaction* between the defect and other defects, sample boundaries or external strain fields and allows to study self-assembly of defects by minimizing the total (free) energy. For artificial or inert cells, that is for physical particles with a static force pattern, but without any internal dynamic or regulatory response, a similar behavior might be expected [48].

In contrast, the interaction of active cells with their elastic environment is clearly more complicated than for physical defects. In particular, the forces

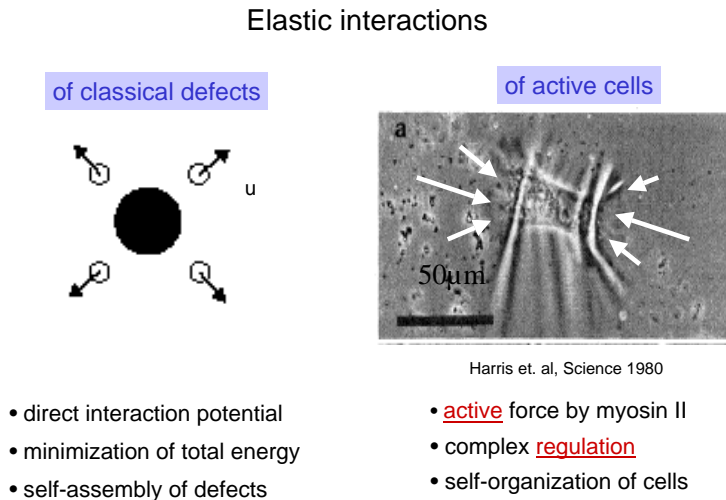


Figure 1.4: Schematic comparison of the interactions of a classical defect (black) with its elastic host lattice (left) and an active cell with its elastic environment (right). Right image: traction forces of a (single) fibroblast cause compression wrinkles of a thin elastic silicone rubber film [18]. Arrows included for illustration purposes.

exerted by the fibroblast in Fig. 1.4 are *actively* generated and involve dynamic and tightly regulated non-equilibrium processes inside the cell. In addition, cellular behavior in principle results from very complex *regulatory* processes. Therefore, the reaction of cells to input signals usually cannot be described with an energy functional as for passive particles. The organization of cells in and on soft materials follows from true self-organization rather than self-assembly.

The theoretical description of active particles provides a huge challenge for theoretical physicists. Stochastic equations are one promising approach to treat these systems [49, 50]. In this work, we will present a different approach and describe the active response of cells to elastic input by deriving an "effective interaction potential" for cells with their elastic environment. For this purpose, a certain, careful analogy of the interaction of cells with their environment to the case of classical defects might still prove very helpful: firstly, the interaction of the defect with its elastic environment is specified by the defect *force pattern*. Similarly, during mechanosensation the cell interacts with the medium by force and the probing force pattern will determine how and what kind of mechanical information the cell is able to interpret. Secondly, defect self-assembly follows from energy minimization. Although cellular behavior in principle results from very complex regulatory processes,

we will show that the typical cellular reaction to mechanical input seems to be a simple preference for large *effective stiffness*. Hence, the overall principle underlying self-organization of cells in soft materials is not energy minimization, but maximization of effective stiffness, which similarly to the physical case can be expressed as an *extremum principle in linear elasticity theory*. This defines our effective interaction potential for cells with their environment.

## 1.4 Objective, Outline and Main Results

While the study of cell and tissue organizing principles has a long history, systematic studies of the effects of mechanical properties of the environment on cell behavior is a relatively new field. New methods from materials science allow to study cell organization with respect to physical cues now in much more detail than previously possible. Ideally, one would like to have a predictive model, which not only would contribute to a better understanding of many physiological situations, but also would be of large practical value for application in tissue engineering. Whereas the role of contact guidance and haptotaxis in tissue organization have been theoretically addressed in coupled transport equations for cell and fiber degrees of freedom [51,52], there exists little theory for elastic effects. The main objective of this thesis is to investigate how the mechanical information gathered at cell-matrix contacts translates into cell behavior and to develop a predictive model for cell organization in soft media [53,54].

In Chapter 2 we introduce the basic concepts of our modeling: *effective stiffness* to describe the mechanical properties of the environment and *anisotropic force contraction dipoles* to model the mechanical action of cells. We then present a unifying formalism using extremum principles in linear elasticity theory to model elastic interactions of both passive defects and active cells. While the basis of the extremum principle for defects is energy minimization, the effective behavior of cells is to maximize the effective stiffness in their environment. This allows to calculate optimal cell organization as a function of cell position and orientation. In particular, we consider interactions with external strain fields, sample boundaries and other cells or defects, respectively. Although there are marked conceptual differences between the physical and cellular cases, they both require to solve the elastic boundary value problem to predict the resulting structure formation. Finally, we propose a mechanism that links the concept of effective stiffness to active mechanosensation at cell-matrix contacts and which could explain why cells prefer stiffness. Cells can make use of the fact that the mechanical properties of the environment modulate the build-up of their own force patterns. In a stiff environment, the build-up of force at focal adhesions is more efficient, which leads to a stronger

signaling response at these sites. This could trigger a corresponding reorganization of the cytoskeleton to (bi)polarize along the direction of maximal effective stiffness.

In Chapter 3 we theoretically consider various situations of cell organization in soft media, which are of large practical interest: cells in external strain fields and cells close to boundaries or interfaces for different geometries and boundary conditions. For this purpose, the elastic equations for an infinite space, the elastic half space and the elastic sphere are solved exactly. The results are then used to predict optimal cell and defect configurations. Our predictions are in excellent agreement with experiments for fibroblasts both on elastic substrates and in hydrogels: e.g. in strained substrates fibroblasts orient along the direction of external strain and close to interfaces they orient perpendicular and in parallel with respect to clamped and free boundaries, respectively. In the case of classical defects, this behaviour is inverted, in accordance with earlier findings [45, 55]. We finally argue that our results indicate that the principle of contact guidance might have to be re-evaluated and compare our theory to existing models for cell organization in the literature [51, 52].

In Chapter 4 we consider elastically mediated interactions between cells. We derive elastic interaction laws and potentials for cells and physical defects, respectively, and study the resulting basic structure formation. While defects with anisotropic force patterns show aggregation behavior similar to electric quadrupoles, cells prefer to align in *strings* similar to electric dipoles because each cell maximally stiffens its environment along the direction of pull. Elastic interactions are long-ranged, i.e. they decay with a power-law. However, we find that the elastic fields generated by a string of aligned cells screen each other very effectively, such that the interaction between strings is short-ranged and decays exponentially on a length scale only determined by geometry.

In Chapter 5 we study pattern formation of cells on elastic substrates due to elastic effects as a function of material properties, cell density and the geometry of cell positioning, which could be controlled experimentally by restricting cell positions using microcontact printing on elastic substrates. We calculate the optimal structures on a lattice semi-analytically and apply Monte Carlo simulations to study the effect of noise and positional disorder on cellular structure formation. Our calculations suggest that cellular force patterns can be engineered to yield qualitatively different structures. For example, we predict the formation of a nematic structure on highly compressible substrates at high cell densities, while on incompressible substrates isotropic patterns dominate. We expect that our theory will be used for biomedical applications in the future, for example to optimize protocols for the design of artificial tissues or implants with respect to sample geometry, boundary condition, material properties and cell density.

# Chapter 2

## Modeling

In this chapter we introduce the basic concepts, which will be applied in the following chapters in order to model cell behavior in a soft environment. In particular, we compare the interactions of physical defects and active cells with an elastic environment and show that they can be modeled within the same theoretical framework using force multipoles and extremum principles in linear elasticity theory. The extremum principle for cells follows from the experimental observation that their effective behavior amounts to a simple preference for large effective stiffness in their environment. At the end of this chapter we will discuss one possible subcellular mechanism in more detail, which could provide an explanation for this effective behavior.

### 2.1 Basic Concepts

#### 2.1.1 Effective Stiffness and Linear Elasticity Theory

##### Effective Stiffness and Effective Interaction Potential

Cell organization in soft media is an active and regulated process which involves mechanosensation at cell-matrix contacts and subsequent information processing in the cellular signal transduction machinery. This certainly implies a severe complication for theoretical modeling. However, it depends on the kind of questions one is interested in, how many details of the regulatory machinery have to be taken into account. The focus of tissue engineering is on the overall cell response (e.g. preferred cell orientation and cell position). Typical questions asked by a tissue engineer are: “What are the environmental stimuli a cell responds to ?” and “How must we design the environment in order to obtain a well defined cell and tissue organization ?”. To answer questions on a tissue scale a coarse-grained, phenomenological modeling is better suited than a detailed biochemical one. Thus, in our model we do not consider any internal biochemistry. Instead, motivated by recent experiments with cells

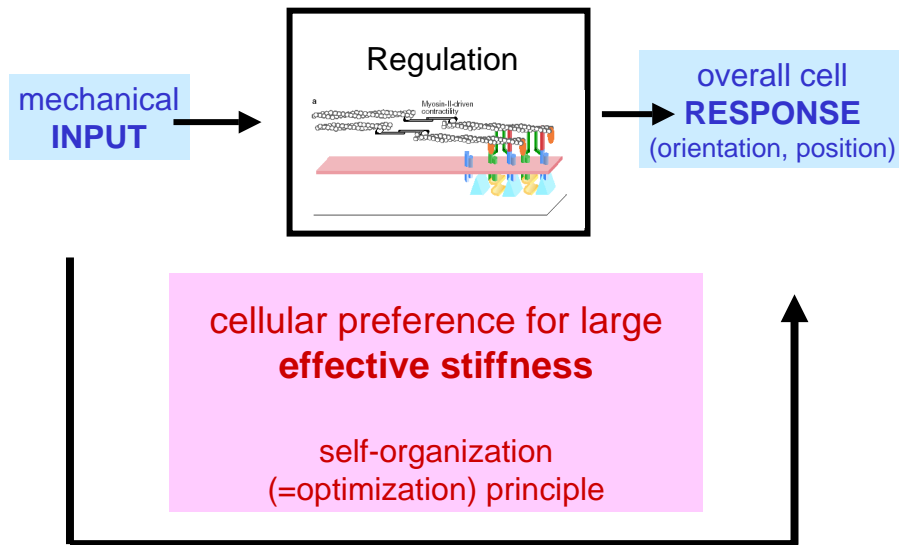


Figure 2.1: Cell organization results from complex regulatory processes inside the cell. However, the typical cell response to mechanical input seems to be a simple preference for large effective stiffness. In our model the concept of stiffness preference is expressed as an extremum principle in linear elasticity theory. This allows to predict preferred cell position and orientation in response to different kinds of mechanical input.

on elastic substrates [12–14], we suggest that the typical overall cell response to mechanical input seems to be simple preference for large *effective stiffness*. At this stage, stiffness preference enters our model as an assumption that mediates a relationship between the mechanical “input” and the overall cellular “output”, i.e. cell orientation and position, as shown in Fig. 2.1. Starting from this principle, we are able to explain many experimental results, which have been reported in the literature both for cells on elastic substrates and in physiological hydrogels, within a unifying theoretical framework.

We will focus on describing the mechanical input rather than on complex regulation issues. In particular, we aim to define a quantity which describes the kind of information which the cell can extract from its soft environment with the help of its contractile machinery. We suggest that an appropriate scalar quantity to characterize the environment is the work  $W$  the cell has to perform in order to build up a certain level of force against the elastic environment. Experimental observations suggest that active cell behaviour amounts to a simple preference for large effective stiffness, which corresponds to

a minimization of this energy. Therefore,  $W$  can be interpreted as an *effective interaction potential* for cells interacting with their elastic environment.

As a simple analogue, consider a linear spring. In order to build up a certain force  $F$ , the energy  $W = Kx^2/2 = F^2/2K$  has to be invested into the spring, where  $x$  is the displacement and  $F = Kx$  is the force at equilibrium. If there is a choice of different springs with different spring constants  $K$ , the smallest amount of energy  $W$  to build up  $F$  has to be invested into the spring with the largest value for  $K$ . Thus,  $W$  and  $K$  are inversely related. In the case of cells, the different springs correspond to different directions as probed by different stress fibers as depicted e.g. in Fig. 2.2, and, on the long run, the cell will orient in that direction that corresponds to the largest value of  $K$  (smallest  $W$ ), possibly because in this direction, the build-up of force is most efficient.

The example of the linear spring can also be used to illustrate the main difference to the interactions of defects with their elastic environment. In this case, the defect–substrate interaction potential is  $V^d = -Fx$  and the final configuration is determined by the overall energy  $V^t = Kx^2/2 - Fx = -F^2/2K = -W$ . Thus, in contrast to the case of cells, for defects minimal values of  $K$  are most favorable.

There are two main reasons why we characterize the environment by the energy  $W$  rather than the spring constant  $K$ . First, as we will show in Section 2.3.2, the quantity  $W$  can be used to describe the effects of increased rigidity (here,  $K$ ) *and* strain in the elastic environment on an equal basis, i.e.  $W$  allows to describe various sources of mechanical input within a *unified* theoretical framework. Thus,  $W$  is a measure for the effective properties of the material as probed by the cell and thereby defines an effective interaction potential. The effective stiffness is *inversely* related to  $W$ , i.e. minimization of  $W$  corresponds to maximization of effective stiffness. Secondly,  $W$  may not only serve as a characterization of the external environment, but might be a relevant quantity for some internal mechanism in the cell. Thus,  $W$  could be used to connect our coarse-grained modeling to the subcellular scale in the future.

It is important to note that conceptually the principle suggested here does not imply that the cell actually minimizes the work  $W$  invested into its soft environment. Instead we suggest that calculating the quantity  $W$  for different situations of interest is an appropriate measure for the kind of information a cell can extract from its elastic environment through active mechanosensing. The real justification of our model will be its success in explaining a large body of experimental data (see Chapter 3). Nevertheless, in Section 2.3.3 we will also present some potential microscopic mechanism to explain the cellular preference for large effective stiffness.

## Linear Elasticity Theory

In order to describe the mechanical properties of the extracellular environment, we model it as a linear, isotropic elastic material. This is a good assumption for elastic substrates. It also captures some of the properties of physiological hydrogels and will keep our analytic calculations in the upcoming chapters feasible.

Elasticity theory as part of continuum mechanics describes the influence of external forces on the shape and the volume of solid bodies. Under deformation a body point located initially at  $\vec{r}$  is displaced by a vector  $\vec{u}(\vec{r}) = \vec{r}' - \vec{r}$ . Changes in the relative distance between points after deformation define the strain tensor  $u_{ij}(\vec{r})$ , which for small deformations can be linearized according to [56]:

$$u_{ij}(\vec{r}) = \frac{1}{2}(u_{i,j} + u_{j,i}). \quad (2.1)$$

The indices after the comma denote partial derivatives with respect to position, i.e.  $u_{j,i} = \frac{\partial u_j}{\partial r_i}$ . The eigenvalues of the symmetric tensor  $u_{ij}$  give the local relative length changes along the principal axes and the trace  $u_{ii}$  gives the relative volume change. Here and in the following, summation over repeated indices is always implied. Every deformation can be decomposed in a homogeneous dilation or hydrostatic compression mode  $u_{ii}$ , where only the volume changes, and a shear mode  $u_{ij} - \frac{1}{3}\delta_{ij}u_{kk}$ , specifying shape changes only.

Elastic bodies resist deformations, i.e. strain leads to internal stress that tries to push molecules back to their initial positions. The internal forces can result either from atomic or molecular interactions, the main contribution in hard solids, or from entropy, the main source of elasticity in many soft matter materials like rubber. We will assume a linear elastic material, characterized by a generalized Hooke's law, i.e. stress is a linear function of strain [56]:

$$\sigma_{ij}(\vec{r}) = C_{ijkl}u_{lk}(\vec{r}), \quad (2.2)$$

where  $C_{ijkl}$  is the elastic constant tensor. For an isotropic material  $C_{ijkl}$  is invariant under arbitrary translations and rotations, i.e.  $C_{ijkl} = \lambda\delta_{ij}\delta_{kl} + \mu(\delta_{ik}\delta_{jl} + \delta_{il}\delta_{jk})$ , where  $\mu$  and  $\lambda$  are the so called Lamé coefficients. Thus, there are only two elastic constants characterizing the two elastic modes. An alternative set are the shear rigidity  $\mu$  and the compression modulus  $\kappa = \lambda + \frac{2}{3}\mu$ .

Experimental values for elastic constants of materials are often given as the Young modulus  $E = 9\kappa\mu/(3\kappa + \mu)$  (*elastic rigidity*) and the Poisson ratio  $\nu = (3\kappa - 2\mu)/(6\kappa + 2\mu)$  (which describes the relative weight of shear and compression mode), since they can be determined from a simple uniaxial stretch experiment.  $E$  can be measured from the relative lengthening along the direction of stretch, i.e.  $\frac{\Delta l_z}{l_z} = \frac{F}{EA}$ , where  $F/A$  is the applied stress, i.e. the force  $F$  acting on the area  $A$ . The Poisson ratio corresponds to the lateral

contraction coefficient,  $\nu = -\frac{\Delta l_x/l_x}{\Delta l_z/l_z}$ . The value of  $\nu$  ranges from  $\nu = 0$  to  $\frac{1}{2}$  for highly compressible to incompressible media, respectively. In practice  $E$  will be of the order of a few kPa (the typical range of tissue rigidity) and  $\nu$  close to 0.5 both for elastic substrates and physiological hydrogels. However, future developments in material science may well lead to materials with smaller values of  $\nu$ .

For our purpose, it is convenient to define another pair of elastic constants,  $\Lambda = \lambda/\mu$  and  $c = 2\mu + \lambda = \mu(2 + \Lambda)$ . The Poisson ratio is then given by  $\nu = \Lambda/2(\Lambda + 1)$  and  $\nu = 1/2, 1/4$  and  $0$  correspond to  $\Lambda \rightarrow \infty, \Lambda = 1$  and  $\Lambda = 0$ , respectively.

### 2.1.2 Force Multipoles

In order for the cell to learn about the mechanical properties of its environment there must be forces involved. In the following, we model a mechanically active cell as a localized force distribution in an elastic medium. In order to describe its mechanical action, we use the concept of a force multipolar expansion, which has been applied before for the description of point defects in condensed matter systems [45–47]. Consider a force distribution localized around the origin. Then the force multipoles are defined as [57, 58]

$$P_{i_1 \dots i_n i} = \int s_{i_1} \cdots s_{i_n} f_i(\vec{s}) d^3 s, \quad (2.3)$$

where  $f_i$  is the force density and  $d^3 s$  denotes a volume integral. The first order term is the vector of overall force,  $P_i$ , and the second order term is the force dipole,  $P_{ij}$ , a tensor of rank two.

For both cells and defects we are interested in, we can assume local forces. For point-like defects, one can moreover assume that the overall force vanishes, because due to Newton's Third Law, the forces exerted by the defect on the elastic medium and by the elastic medium on the defect have to balance each other (the same argument applies to point defects in a fluid medium [59–61]). For cells, the situation is more complicated because they are at the same time in contact with the elastic matrix and an aqueous medium. Thus, unbalanced forces might appear in the elastic matrix, which are balanced by viscous forces in the aqueous medium. However, viscous processes in the fluid medium decay very rapidly on the timescale of cell movement. Therefore unbalanced forces might occur for short periods of time, e.g. during back retraction of a locomoting cell, but during most of the time, cells can be expected to be in mechanical equilibrium, as suggested by experiments measuring force patterns of both stationary and locomoting cells on elastic substrates [34, 37]. Then overall force vanishes and the force dipole is the first relevant term in the multipolar expansion Eq. (2.3).

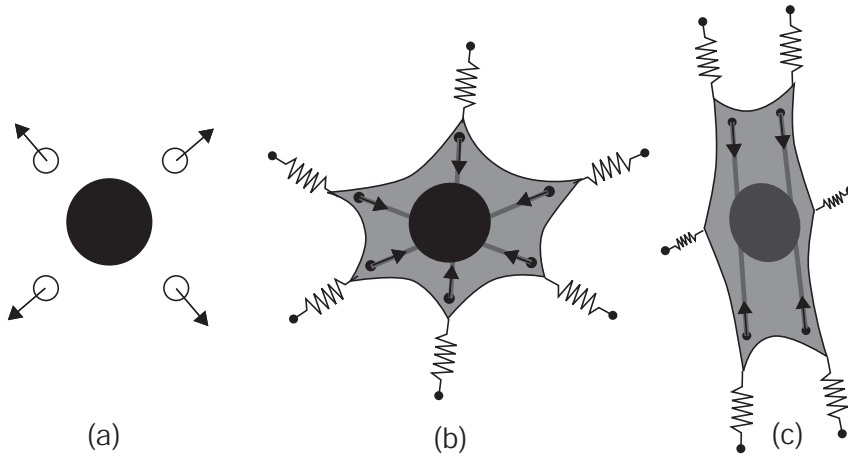


Figure 2.2: Schematic representation of physical and cellular force dipoles (a) Physical case: an intercalated defect deforms the simple cubic host lattice, thus acting as an isotropic force expansion dipole. (b) Cellular case: anchorage dependent cells probe the mechanical properties of their environment through their contractile machinery. Actin stress fibers (lines) are contracted by myosin II molecular motors and connected to the environment through focal adhesions (dots). In isotropic environments cells often show round or stellate morphology. Even in this case, different stress fibers probe different spatial directions and the probing process can be modeled by anisotropic contraction dipoles. (c) In an elastic anisotropic environment cells orient along the direction of maximal effective stiffness in the environment. Cells may also spontaneously break symmetry, e.g. during locomotion or during periods of large mechanical activity. Then most stress fibers run in parallel and the whole cells appears as an anisotropic contraction dipole.

In general, force dipoles are classified according to their symmetry properties into isotropic dipoles (centers of contraction or dilation), anisotropic dipoles without moment and anisotropic force dipoles with moment [58]. Force dilation and force contraction dipoles have only positive and only negative eigenvalues, respectively. For example, in three dimensions three pairs of juxtaposed forces, one for each coordinate direction, form an isotropic force dipole, where  $P_{ij} = P\delta_{ij}$ . Such a force dipole describes a spherical inclusion in a simple cubic lattice, see Fig. 2.2(a) [45]. Applied to two dimensions, it describes atomic defects adsorbed onto a substrate [46]. An anisotropic force dipole without moment is a non-diagonal, but symmetric tensor. For example, for a couple of juxtaposed forces with a dipole strength  $P$  and an orientation in direction  $\vec{l}$ , we can write the force dipole tensor as  $P_{ij} = P\hat{l}_i\hat{l}_j$ . An anisotropic force dipole without moment oriented in the  $z$ -direction reads  $P_{ij} = P\delta_{iz}\delta_{jz}$  and describes for example an atomic defect intercalated in graphite [47]. Fi-

nally, an anisotropic force dipole with an angular moment describes a set of two opposing forces  $\vec{F}$  separated by a distance  $\vec{l}$  oriented arbitrarily with respect to  $\vec{F}$ , which leads to  $P_{ij} \neq P_{ji}$ . In this work, we only consider force dipoles without such moments.

The basic cellular probing force pattern during mechanosensing is a contractile stress fiber connecting two focal adhesions. Obviously this minimal system obeys mechanical equilibrium and can be described as an *anisotropic force contraction dipole*. Cells in an isotropic environment often show isotropic (i.e. round or stellate) morphologies as shown in Fig. 2.2(b). However, since the focal adhesion dynamics is local, even in this case there is an anisotropic probing process that can be modeled by anisotropic force contraction dipoles. As we will argue below, only an anisotropic probing process can react to anisotropies in the environment. The anisotropy of focal adhesion dynamics becomes apparent when stress fibers start to orient in one preferential direction, either spontaneously during a period of large mechanical activity, or as a response to some external anisotropy (e.g. stiffness variation), or during cell locomotion (Fig. 2.2(c)). In this case, cellular dipoles have been measured to be of the order of  $P \approx -10^{-11} \text{J}$  (this corresponds to two forces of 200 nN each, separated by a distance of 60  $\mu\text{m}$ ) [37, 62].

## 2.2 Elastic Interactions of Defects

The elastic medium surrounding a particle can mediate an *elastic* interaction with other particles, sample boundaries or external strain fields. It is important to note that this effect requires a *direct* interaction of the particle with its elastic environment. In traditional condensed matter systems, the direct interaction is usually a quantum effect (e.g. Born repulsion for defects intercalated into a crystal lattice or van der Waals attraction for defects adsorbed onto a crystal lattice). The interaction of a single particle localized at  $\vec{r}$  with the elastic medium can be described by an interaction potential  $V^d(\vec{r}, \vec{u})$ , which not only depends on position  $\vec{r}$ , but which also is a functional of the displacement field  $\vec{u}(\vec{r})$  of the elastic medium. For a fixed particle position  $\vec{r}$ , we can expand the interaction potential with respect to the displacement field:

$$V^d(\vec{r}, \vec{u}) \approx - \int f_i(\vec{r} + \vec{s}) u_i(\vec{r} + \vec{s}) d^3s, \quad (2.4)$$

where  $f_i = -\delta V^d / \delta u_i|_{u_i=0}$  is the force density exerted by the defect onto the elastic medium in its undeformed reference state. The expansion can be terminated after the linear term because we assume small deformations, or, equivalently, small forces. This linearized interaction potential is widely used in the literature on elastic defects in traditional condensed matter materials

[45–47]. For later use, we also note that Eq. (2.4) can be rewritten in terms of the force multipoles defined in Eq. (2.3), if one makes the assumption that the interaction of the defect with the medium is short-ranged. Then

$$V^d(\vec{r}, \vec{u}) \approx - \sum_{n=0}^{\infty} \frac{1}{n!} P_{i_1 \dots i_n} u_{i_1 \dots i_n}(\vec{r}). \quad (2.5)$$

In this way, all the details of the direct interaction between medium and defect are subsumed in the defect force pattern and one can study elastic effects in different materials within a common theoretical framework, as long as the two assumptions of small and localized forces are valid.

The displacements of the elastic medium are controlled by a competition between the direct interaction between defect and medium and the elastic strain energy of the medium under the constraints of adequate boundary conditions. The strain energy is [56]

$$V^e = \frac{1}{2} \int d^3r C_{ijkl} u_{ij}(\vec{r}) u_{kl}(\vec{r}). \quad (2.6)$$

Consider now the general case of an elastic medium subject to loading with defects with an overall volume force density  $\vec{f}(\{\vec{r}^\alpha\}, \vec{r}) = \sum_\alpha \vec{f}^\alpha(\vec{r})$ , where  $\alpha$  numbers the different defects and  $\{\vec{r}^\alpha\}$  specifies the defect configuration. Then the total energy of the system is

$$\begin{aligned} V^t &= \frac{1}{2} \int d^3r C_{ijkl} u_{ij}(\vec{r}) u_{kl}(\vec{r}) - \int d^3r f_i(\{\vec{r}^\alpha\}, \vec{r}) u_i(\vec{r}) \\ &- \oint dS f_i^s(\vec{r}) u_i(\vec{r}), \end{aligned} \quad (2.7)$$

where the first term is the strain energy  $V^e$  and the second term the direct interaction  $V^d = \sum_\alpha V^d(\vec{r}^\alpha)$ . The surface force density  $\vec{f}^s$  in the third term acts as a Lagrange multiplier that enforces the boundary conditions at the sample surface  $S$ . For a fixed defect configuration, the displacements  $\vec{u}(\vec{r})$  are determined from  $\delta V^t / \delta \vec{u} = 0$ , which defines mechanical equilibrium:

$$C_{ijkl} u_{kl,j}(\vec{r}) = -f_i(\{\vec{r}^\alpha\}, \vec{r}) \quad \vec{r} \text{ in } V, \quad (2.8)$$

and the boundary condition at the surface of the elastic material:

$$C_{ijkl} u_{kl}(\vec{r}) n_j(\vec{r}) = f_i^s(\vec{r}) \quad \vec{r} \text{ on } S, \quad (2.9)$$

where  $\vec{n}$  is the outward directed surface normal of the surface element  $dS$ . For an isotropic elastic material, Eq. (2.8) is conveniently rewritten using a vector notation as:

$$\Delta \vec{u}(\vec{r}) + (1 + \Lambda) \nabla \nabla \cdot \vec{u}(\vec{r}) = -\frac{\vec{f}(\vec{r})}{\mu} \quad \vec{r} \text{ in } V. \quad (2.10)$$

By combining Eq. (2.8) and Eq. (2.6), one finds  $V^e = \frac{1}{2} \int d^3r f_i u_i = -\frac{1}{2} V^d$ . Therefore the overall energy  $V^t = V^d + V^e = \frac{1}{2} V^d = -V^e$  and the overall energy can be written as function of the defect configuration only. In this way, the *direct* interactions of the particles with the medium can be transformed into an *indirect* interaction between defects. This also allows the calculation of the interaction of a single defect with a boundary induced strain field or an external strain field applied at the boundary. The ground state configuration of elastically interacting defects is obtained by minimizing the total energy  $V^t$ .

## 2.3 Elastic Interactions of Cells

### 2.3.1 An Extremum Principle

The forces exerted by mechanically active cells on the environment are mainly due to actomyosin contractility. Thus, in contrast to the interaction of physical force dipoles with the elastic medium, where the force can be derived from conventional interaction potentials, cellular forces are continuously and actively generated by the cell and involve non-equilibrium processes, that are tightly regulated by biochemical events inside the cell. Hence, the interactions of cells with an elastic environment are more complicated than for physical defects and there is little a priori reason why they should be described by Eq. (2.4). Motivated by recent experiments with cells on elastic substrates [12–14], we have already argued that despite these complications, a similar description as for defects can be employed for cells. In Section 2.1 we introduced the concept of effective stiffness and effective stiffness preference as a self-organization principle for cells. We now explain our reasoning in more detail for the case of cells in a three-dimensional environment described by continuum elasticity theory. In analogy to the simple harmonic spring model, the *local effective stiffness* of the elastic environment is the inverse of the work  $W$  required to build up a given force pattern in the elastic medium. The deformation work  $W$  required to build up an arbitrary force distribution  $\vec{f}(\vec{r})$  is given by:

$$W = \int d^3r \int_0^{u_{ij}^{\vec{f}}} C_{ijkl} u_{kl}(\vec{r}) du_{ij}(\vec{r}), \quad (2.11)$$

which in the absence of external prestrain is equivalent to the energy stored in the elastic medium given in Eq. (2.6). Then integration by parts gives

$$W = -\frac{1}{2} \int d^3r u_i(\vec{r}) C_{ijkl} u_{kl,j}(\vec{r}) + \frac{1}{2} \oint dS n_j C_{ijkl} u_{kl}(\vec{r}) u_i(\vec{r}). \quad (2.12)$$

Applying the mechanical equilibrium conditions of the elastic medium, Eqs. (2.8,2.9), yields

$$W = \frac{1}{2} \int d^3r u_i(\vec{r}) f_i(\vec{r}) + \frac{1}{2} \oint dS u_i(\vec{r}) f_i^s(\vec{r}). \quad (2.13)$$

In an infinite medium the boundary condition at the surface yields a vanishing surface integral. Hence for a force distribution centered around  $\vec{r}$ , the volume integral can be turned into a local expression by using the definitions of Eq. (2.3):

$$W^\infty = \frac{1}{2} \int f_i(\vec{r} + \vec{s}) u_i(\vec{r} + \vec{s}) d^3s = \frac{1}{2} \sum_{n=0}^{\infty} \frac{1}{n!} P_{i_1 \dots i_n} u_{i_1 \dots i_n}(\vec{r}). \quad (2.14)$$

In particular, for a force monopole and a force dipole one finds  $W^\infty = \frac{1}{2} P_i u_i^\infty(\vec{r})$  and  $W^\infty = \frac{1}{2} P_{ij} u_{ij}^\infty(\vec{r})$ , respectively, where  $\vec{u}^\infty$  and  $u_{ij}^\infty$  are the displacement and strain tensor fields caused by the respective force multipole in an infinite homogeneous medium. Formally,  $W^\infty$  is a self-energy term and diverges for a point force, but this divergence can easily be removed by assuming distributed force.

Since strain scales inversely with elastic constants,  $W^\infty$  decreases if the elastic constants increase. For an elastically anisotropic medium,  $W^\infty$  varies with the direction of force application, which provides an orientational clue for cell orientation. As we will see below, tensile prestrain or boundary-induced tensile image strain also leads to an increased  $W^\infty$ . Therefore minimization of  $W^\infty$  as a function of position and orientation of force application corresponds to the experimentally observed cellular preference for large effective stiffness. In this way,  $W$  can be interpreted as an *effective interaction potential* that describes the elastic interaction of cells with their environment.

In analogy to the case of elastic interactions of physical defects, where the overall interaction energy could be written as a function of the defect configuration only, one can calculate the strain tensor in Eq. (2.14) by solving the elastic boundary value problem. The mechanical equilibrium condition Eq. (2.8,2.10) states that the body forces  $f_i(\vec{r})$  applied to an elastic medium are balanced by the internal restoring forces  $\sigma_{ij,j}(\vec{r})$ . This equation has to be solved under the appropriate boundary conditions. Since the differential equation Eq. (2.10) is linear, the superposition principle applies and the boundary value problem is formally solved by determining the Green tensor  $G_{ij}(\vec{r}, \vec{r}')$ , i.e. the kernel for a point-like body force  $f_i(\vec{r}) = f_i \delta(\vec{r} - \vec{r}')$ . The elastic fields of more complicated force distributions can be obtained by convolution of the Green tensor with the force density, i.e.  $u_i(\vec{r}) = \int G_{ij}(\vec{r}, \vec{r}') f_j(\vec{r}') d^3r'$ . The elastic fields resulting from force dipoles are obtained by differentiation of  $G_{il}$ ,  $u_i(\vec{r}) = G_{il,k}(\vec{r}, \vec{r}') P_{kl}$  and  $u_{ij}(\vec{r}) = G_{il,kj}(\vec{r}, \vec{r}') P_{kl}$ . In general, the determination of Green functions in elasticity theory for a given geometry and boundary condition is rather difficult, since the second term in Eq. (2.10) couples different components of the displacement field. By taking the Laplacian of Eq. (2.10), one arrives at the biharmonic equation  $\Delta \Delta \vec{u} = 0$  for the displacements. Thus, harmonic potential theory is frequently used, for instance in the stress function  $\chi$ -method [56] and in the Galerkin-vector approach [63], in addition to

other methods like expansion of  $\vec{u}$  in terms of a suitable complete basis set of orthonormal functions [55].

### 2.3.2 Contributions to the Effective Stiffness

#### External Strain

We now consider how a cell establishes a force pattern in a prestrained homogeneous medium. The work required to generate a force pattern  $\vec{f}$ , which results in strain  $u_{ij}^{\vec{f}}$ , in the presence of an externally imposed strain field  $u_{ij}^e(\vec{r})$  is given by:

$$\begin{aligned} W &= \int d^3r \int_0^{u_{ij}^e + u_{ij}^{\vec{f}}} C_{ijkl} u_{kl}(\vec{r}) du_{ij}(\vec{r}) \\ &\quad - \int d^3r \int_0^{u_{ij}^e} C_{ijkl} u_{kl}(\vec{r}) du_{ij}(\vec{r}) = W^\infty + \Delta W^e \end{aligned} \quad (2.15)$$

with

$$\Delta W^e = \int d^3r C_{ijkl} u_{ij}^{\vec{f}} u_{kl}^e(\vec{r}) = \sum_{n=0}^{\infty} \frac{1}{n!} P_{i_1 \dots i_n} u_{i_1 i_1 \dots i_n}^e(\vec{r}). \quad (2.16)$$

The derivation of Eq. (2.16) proceeds along the same lines as for Eq. (2.14). In particular, for a single force dipole one gets  $\Delta W^e = P_{ij} u_{i,j}^e(\vec{r})$ . Because of contractile cell activity,  $P_{ij}$  has negative eigenvalues ( $P < 0$ ). Thus, tensile prestrain ( $u_{ij}^e > 0$ ) decreases  $W$  as does a larger rigidity  $E$  and hence is interpreted by the cell as an increase in effective stiffness (*strain-stiffening*). In contrast, compressive prestrain corresponds to a decrease in effective stiffness and hence is avoided by the cell.

#### Boundary-induced Image Strain

We now consider the energy involved to deform an elastic medium in the presence of a sample boundary. In order to quantify the effect introduced by the boundary, we split  $u_{ij} = u_{ij}^\infty + u_{ij}^b$  into a contribution arising in an infinite medium  $u_{ij}^\infty$  and a boundary induced strain field  $u_{ij}^b$  (*image strain*) that depends on sample geometry and boundary condition.  $\vec{u}^\infty$  ensures that the force balance is satisfied everywhere in the sample volume  $V$ . However,  $\vec{u}^\infty$  will not satisfy the boundary condition at  $S$ . For this purpose  $\vec{u}^b$  has to be introduced. In order to keep the force balance in the sample, the image displacements  $\vec{u}^b$  have to be homogeneous solutions of Eq. (2.10). Otherwise they can be chosen in such a way that the boundary conditions are satisfied. Now  $W = W^\infty + \Delta W^b$ , where  $W^\infty$  is the energy of the infinite medium and

$\Delta W^b$  is the additional energy due to the boundary effect. For the latter, we have

$$\Delta W^b = \frac{1}{2} \int d^3r f_i(\vec{r}) u_i^b(\vec{r}) + \frac{1}{2} \oint dS f_i^s(\vec{r}) u_i(\vec{r}) \quad (2.17)$$

which includes both the effects of fixed boundary strain and fixed boundary forces. In principle, the boundary conditions in a physiological context can be very complicated. In our calculations we will restrict ourselves to two fundamental reference cases, namely *free boundaries*, where the normal traction vanishes at the boundary, i.e.  $f_i^s(\vec{r}) = 0$ , and *clamped boundaries*, where the displacements vanish at the boundary, i.e.  $u_i(\vec{r}) = 0$ . We will refer to the former as the *Neumann problem* and to the later as the *Dirichlet problem*. In both cases, the surface integral in Eq. (2.17) vanishes. Thus, the effective interaction potential for a cell interacting with a boundary is given by  $\Delta W^b = \frac{1}{2} P_{ij} u_{i,j}^b(\vec{r})$ , which is inversely related to the change in effective stiffness induced by the boundary. In this way, cells can actively sense not only the presence of a close-by surface, but also its shape and boundary condition.

### Cellular Traction Fields: Elastic Interactions

Strain fields produced by other cells may be large enough to be detected as external strain by other cells, which gives rise to an elastic interaction of cells. The change in  $W$  encountered by a force pattern  $\vec{f}$  centered around  $\vec{r}$  caused by a second force pattern  $\vec{f}'$  centered at  $\vec{r}'$  is given by:

$$\begin{aligned} \Delta W^{\vec{f}\vec{f}'} &= \int d^3s f_i(\vec{r} + \vec{s}) u_i(\vec{r} + \vec{s}) \\ &= \int \int d^3s d^3s' f_i(\vec{r} + \vec{s}) G_{ij}(\vec{r} + \vec{s}, \vec{r}' + \vec{s}') f'_j(\vec{r}' + \vec{s}') \\ &= \sum_{n=0}^{\infty} \sum_{m=0}^{\infty} \frac{1}{n!} \frac{1}{m!} P_{i_1 \dots i_n} G_{ij, i_1 \dots i_n j'_1 \dots j'_m}(\vec{r}, \vec{r}') P'_{j_1 \dots j_m}, \end{aligned} \quad (2.18)$$

where the indices  $i_1 \dots i_n$  denote derivatives of the Green function with respect to the unprimed coordinates and  $j'_1 \dots j'_m$  derivatives with respect to the primed coordinates. For translationally invariant geometries, for instance in infinite space,  $G_{ij}(\vec{r}, \vec{r}') = G_{ij}(\vec{r} - \vec{r}')$  and derivatives for  $j'_k$  become equivalent to derivatives for  $-i_k$ .

Even if cells have initially isotropic force patterns, they will sense anisotropic strain and begin to polarize. As a model for elastically interacting cells, we consider how identical, static anisotropic contraction dipoles organize in a soft medium in order to sense maximal effective stiffness in their environment. The force dipolar interaction corresponds to the case  $n = m = 1$  in Eq. (2.18):

$$\Delta W^{PP'} = P_{li} u_{i,l}(\vec{r}) = P_{li} G_{ij, lk'}(\vec{r}, \vec{r}') P'_{kj} \quad (2.19)$$

and will be discussed in more detail in Chapter 4.

### 2.3.3 Mechanosensing and Effective Stiffness

Our modeling starts from the phenomenological observation that cells seem to prefer maximal effective stiffness in their environment. Although it can be justified *a posteriori* by its large success in explaining experimental observations (see Chapter 3), we also want to motivate a possible mechanism for our main assumption.

#### Biology of Mechanosensing at Cell–Matrix Contacts

The biology of active mechanosensing is quite complicated and not yet fully understood. Interesting questions from the point of view of molecular biology are how the mechanical signal is transduced into a biochemical one and which pathways are subsequently triggered that lead to a cell response.

The first evidence that cells respond to forces (of strength typically generated by the cytoskeleton) exerted on nascent attachment sites came from the Sheetz-lab in 1997 [15]. The rearward movement of small fibronectin coated beads on the lamellipodium was restrained with a laser tweezer, which resulted in a rapid proportional *reinforcement* of the integrin-cytoskeletal linkages, such that after escape from the laser trap on average a three times larger force was required to move the bead.

Reinforcement could be caused either by an increase in the number of integrin-cytoskeletal linkages (clustering response) or by a strengthening of existing links (recruitment response), e.g. by the recruitment of proteins enhancing the interaction between integrins and the cytoskeleton, or both [15]. Recent experiments suggest that recruitment of actin-binding proteins like filamin and in particular talin-1 [64] to attachment sites and the subsequent recruitment of the focal adhesion protein vinculin [65] seem to be critical for early reinforcement of initial adhesions. On the other hand, for mature focal adhesions there exists a clear correlation between size (i.e. the number of links) and the force exerted on the adhesion [16, 28]. Moreover, by blocking cellular contractility, focal adhesions shrink [16], while the application of an external (inward directed pulling) force to focal complexes causes contact growth in the direction of force application [17].

The initial transduction of the mechanical signal into biochemistry is not yet resolved. Experimental evidence points to several non-exclusive mechanisms for mechanosensation including stretch sensitive ion channels [66, 67], incorporation of focal adhesion proteins into the tensed cytoskeleton [68], structural rearrangement of the whole dynamic adhesion aggregate [39, 69, 70] or force-dependent transitions between an active and inactive conformations of focal adhesion proteins. Several proteins localizing to focal adhesions exist in two conformational states including integrin [71, 72], vinculin [73, 74], talin [75] and the Src-phosphatase pp60src [76]. Typically transitions between active and

inactive states are triggered by binding events of other signaling molecules, but these transitions may also be induced by force [16].

Force dependent modifications within cell–matrix contacts may then trigger a signaling cascade, which is responsible for reinforcement or destabilization of the cell–matrix adhesion, respectively. An important pathway for regulating the stability of cell–matrix adhesions seems to be the focal adhesion kinase (FAK)–Src–pathway [35]: the receptor-like tyrosine phosphatase (RPTP- $\alpha$ ), which is involved in activation of Src-family kinases, was recently shown to act as a transducer of mechanical force and required for early reinforcement [77]. On the other hand, e.g. the activation of FAK seems to be important for adhesion site turnover [78].

Finally, the force-dependent signaling cascade may *feed back* on the force generating actin cytoskeleton, in particular via the activation of the small GTPase RhoA, which promotes focal adhesion growth through its downstream targets MLCP (myosin light chain phosphatase) and MLCK (myosin light chain kinase), which both enhance myosin II contractility, and the activation of mDia, a member of the formin homology protein family, whose role in promoting aggregation is less clear [17, 79]. Force dependent MLCK-activation at cell–matrix contacts is also implied by a recent study observing periodic lamellipodial contractions for spreading cells [80, 81]. Force-dependent signals may also effect the microtubule cytoskeleton, which might be involved in destabilizing adhesions and promoting adhesion site turn-over and thus on the long run might counteract the positive feedback loop provided by Rho-signaling [79, 82, 83].

### Possible Origin of Optimization Principle

Stabilization of contacts under force seems at first paradoxical, since the application of force to adhesion clusters typically destabilizes them and above a critical force the contact is expected to rupture [84, 85]. The property of focal adhesions to act as mechanosensory devices is attracting the attention of several physicists [85–88].

In order to develop a model for active mechanosensation, it might be helpful to separate the process into three parts: the force generation system, the force sensing system, which transduces force into a biochemical signal, and the effector system, responsible for reinforcement. Most theoretical efforts have focused on providing a biophysical explanation for the force sensory mechanism at focal adhesions. For example, the clustering response might be a result of a force induced phase-separation of proteins [86]. The asymmetric growth of focal adhesions could be caused by an inhomogenous strain distribution at focal adhesions, which leads to a higher protein density at the rear than at the front [87, 88]. In this work we are primarily interested in how the environment

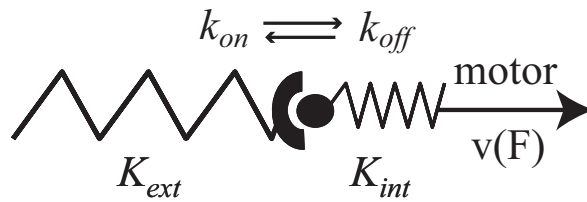


Figure 2.3: Simple model for force build-up at cell–matrix contacts. Myosin motors pull on a closed bond stretching extra- and intracellular components, which act as two springs in series with stiffness  $K_{\text{ext}}$  and  $K_{\text{int}}$ , respectively. The bond is highly dynamic and opens and closes with typical rate constants  $k_{\text{on}}$  and  $k_{\text{off}}$ . With increasing load myosin motors slow down, which is described by the force-velocity relation  $v(F)$ .

effects cellular behavior. Since the stiffness of the environment affects force build-up, we will focus on the force generation process by introducing a simple deterministic model for force generation at cell–matrix contacts.

Consider a single bond connected to a soft spring with spring constant  $K_{\text{ext}}$  representing the soft external environment as shown in Fig. 2.3. One might also include an internal spring with spring constant  $K_{\text{int}}$  to represent the typical mechanical resistance of some cytoplasmic elements that get stretched during force build-up.  $K_{\text{ext}}$  and  $K_{\text{int}}$  act as two springs *in series* with a total spring constant  $K$  given by  $\frac{1}{K} = \frac{1}{K_{\text{ext}}} + \frac{1}{K_{\text{int}}}$ . The bond is loaded by forces generated by the cytoskeleton. Force generation by the acto-myosin apparatus occurs via the “filament-sliding” mechanism, i.e. myosin heads row against actin filaments powered by ATP-hydrolysis, which causes filaments to slide past each other. When the bond is open, filaments move with a typical velocity  $v_0$  and no force is generated. When the bond is closed at time  $t = 0$ , the filament starts to move, thereby stretching the two springs and force builds up. The restoring force exerted by the stretched springs on the filament results in a slowing down of the motors until finally the stall force  $F_s$  is reached. The force-velocity curve for the filament under load can be linearized according to [38]:

$$v(F) = v_0 \left( 1 - \frac{F}{F_s} \right). \quad (2.20)$$

The load  $F$  acting on the contractile filament is determined by the displacement  $x = x_{\text{ext}} + x_{\text{int}}$  of the springs via  $F = -Kx$ . Thus, the energy  $dW$  required to displace the filament by  $dx$  is given by  $dW = -Fdx = \frac{F}{K}dF$ . The dynamics of force generation by a single filament is therefore governed by

$$L = Fv(F) = \frac{dW}{dt} = \frac{F}{K} \frac{dF}{dt}, \quad (2.21)$$

where  $L$  is the power invested by myosin motors into stretching the springs. Thus,  $\frac{dF}{dt} = v_0 K \left(1 - \frac{F}{F_s}\right)$  and the force as a function of time can be calculated to be:

$$F(t) = F_s \left(1 - \exp\left(-\frac{t}{t_K}\right)\right). \quad (2.22)$$

Eq.(2.22) shows that there exists a typical time scale  $t_K$  for force build-up given by:

$$t_K = \frac{F_s}{v_0 K}. \quad (2.23)$$

The larger the stiffness  $K$  and the higher myosin activity, the faster force is built up. The asymptotic force at  $t \rightarrow \infty$  is only determined by the stall force  $F_s$ .

However, bonds at cell-matrix contacts are highly dynamic [69, 70]. Thus, there may exist a competing time scale  $t_k$ , which is determined by the reaction kinetics of all bonds involved in linking actin to the extra-cellular environment (e.g. actin-talin-integrin-fibronectin). The dominant contribution arises from the weakest bond, i.e. from the bond with the largest off-rate  $k_{\text{off}}$ , which, in fact, for initial adhesions might be the talin-actin bond [89]. We therefore may replace the complicated coupling/decoupling dynamics of actin filaments to the environment by a single binding and unbinding process with effective rates  $k_{\text{on}}$  and  $k_{\text{off}}$ . In principle the dissociation rate could also depend on force. A simple model for bond rupture is described by Kramers theory, where the closed and open state are separated by a finite energy barrier  $\Delta E$  (characterizing the bond strength, which typically is a few  $k_B T$ ) along a one-dimensional reaction coordinate  $x$ . The transition rate from the closed to the open state is determined by an Arrhenius law  $k_{\text{off}}^0 = k_0 e^{-\Delta E/k_B T}$ . When force  $F$  is applied to the bond, the potential landscape is tilted and the height of the barrier is reduced by  $F x_b$ . This facilitates the escape of the bond from the closed state and the transition rate becomes  $k_{\text{off}} = k_{\text{off}}^0 e^{F/F_b}$ , where  $F_b = k_B T/x_b$  defines a typical force scale for the bond. For a constant force the mean life-time of the bond therefore decreases exponentially with force. For the time dependent loading protocol by motors given in Eq. 2.22, the situation is more complicated. Two parameters determine whether  $t_k$  is affected by force, the ratio of the forces  $\alpha = F_s/F_b$  and the ratio of time scales  $\beta = t_k/t_K$ . When  $\alpha\beta \ll 1$  the bond is not affected by loading (i.e. the bond dissociates before sufficient force is built up), when  $\alpha\beta \gg 1$  the mean life-time decreases. A lower bound for the mean life-time can be estimated from the linear loading protocol, then  $t_k \rightarrow t_k \frac{1}{\mu} \ln \mu$ , where  $\mu = \alpha\beta$  represents a dimensionless loading rate [90].

Taking into account the competition between force generation dynamics  $t_K$  and contact dynamics  $t_k$  and assuming for simplicity  $\alpha\beta < 1$ , the averaged force  $\langle F \rangle$  attained during filament attachment becomes a simple hyperbolic

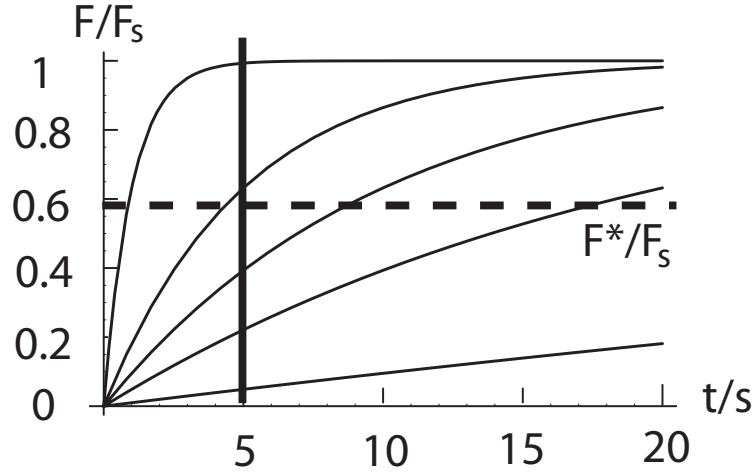


Figure 2.4: Deterministic force build-up dynamics for loading of a single bond by myosin-powered contractility with  $v_0 = 10\mu\text{m/s}$  and  $F_s = 10\text{pN}$  for different values of the spring constant  $K = 1, 5, 10, 20, 100\text{ pN}/\mu\text{m}$  (bottom to top). The competing time scale from bond adhesion dynamics shown as a vertical line is taken to be  $t_k = 5\text{s}$  (and for simplicity assumed to be not effected by force). We also include a putative force threshold  $F^*$  that the cell has to reach to trigger signaling. Only bonds encountering a stiff environment can reach  $F^*$  within the time  $t_k$ .

function of the ratio of the two time scales  $t_k$  and  $t_K$ :

$$\langle F \rangle = \int_0^\infty P(t)F(t)dt = \frac{F_s}{1 + \frac{t_K}{t_k}} \quad (2.24)$$

where  $P(t) = \frac{e^{-t/t_k}}{t_k} dt$  is the probability that the bond breaks at time  $t$  in an interval  $dt$ . When  $\alpha\beta > 1$ ,  $\langle F \rangle$  is expected to decrease as a function of  $\alpha$  and  $\beta$ .

Suppose now that the cell is initially pulling at several cell–matrix contacts with a similar investment of resources (myosin, actin, ATP), such that  $t_K$  at a given contact is only determined by the stiffness of the external spring. In Fig. 2.4 we plot  $F(t)$  for several values of  $K_{\text{ext}}$  by keeping the other parameters fixed. Some competing time scale  $t_k$  is shown as vertical line. The stiffer the spring, the faster force builds up and the larger the attained force will be on average. If a certain threshold in force  $F^*$  triggers reinforcement, then larger stiffness is more favorable and only bonds in a stiff environment can reach  $F^*$  on average. Positive feedback loops from the effector to the force generating system could additionally enhance force build-up dynamics. For example, a force induced enhancement of myosin activity, e.g. through activation of RhoA [17, 79] or myosin light chain kinase (MLCK) [80], increases contractility and thus force build-up dynamics through an effectively increased  $v_0$  and

$F_s$ , respectively. Similarly, the recruitment response, e.g. of vinculin [65], to nascent attachment sites strengthens links at cell-matrix contacts and thus decreases  $k_{\text{off}}$ , i.e. increases  $t_k$  which tends to increase  $\langle F \rangle$ , and thus also may constitute a positive feedback loop. Positive feedback may enhance the dynamics of adhesion site maturation and contact growth at stiff compared to soft sites, such that contacts in a stiff environment grow faster and eventually might outgrow competing contacts. In the long run, this could trigger a corresponding reorganization of the cytoskeleton and could be the reason why cells in an mechanically anisotropic environment orient their cytoskeleton along the direction of maximal stiffness. The positive feedback loop(s) could be counteracted by microtubules, which seem to be attracted to focal adhesions with some time delay and involved in destabilizing contacts [79, 82, 83].

This simple model already makes some more interesting predictions: first, it shows that active mechanosensation is a "relative" process, which is affected both by the stiffness of the environment and by the cell itself through contractility, adhesion dynamics and internal stiffness. Possible targets for feedback from the effector to the force generating system can be identified using this model. The model also suggests that the internal stiffness  $K_{\text{int}}$  of cells may affect how the mechanical environment is perceived by cells.  $K_{\text{ext}}$  and  $K_{\text{int}}$  act as two springs in series, such that the overall stiffness is dominated by the softer spring. This implies that internally soft cells paradoxically may interpret a stiff environment as being *soft* rather than stiff because not sufficient force for signaling can be generated. One therefore may expect that cells adapt the internal stiffness to the external stiffness in order to optimize the detection of stiffness variations in their environment. Finally, the model predicts that there exists an optimal range in stiffness determined by  $t_K \approx t_k$ , where cells are most susceptible to variations in stiffness, i.e. small changes in  $K$  lead to large changes in  $F$ .

The main purpose of introducing this model was to show how the concept of effective stiffness represented by  $W$  can be linked to mechanosensation and stiffness preference.  $W$  enters into Eq.(2.21), which determines the dynamics of force generation. Thus,  $W$  is not only a convenient quantity to characterize the mechanical properties of the environment, but could be an integral part of cellular decision making.

The single bond picture might be a good approximation for nascent adhesions with only a few bonds, where  $v_0 \approx 0.1\mu\text{m}/\text{s}$ ,  $f_s \approx 10\text{pN}$  [15, 89]. When  $K \approx 10\text{pN}/\mu\text{m}$ ,  $t_K$  is on the order of seconds, which compares to typical biological dissociation rates for actin binding proteins of  $k_{\text{off}} \sim \text{s}^{-1}$  [91]. For large focal adhesions, cooperativity between bonds should be included [85]. In this case the relevant time scales might be replaced by the typical life time  $t_k$  of a contact compared to the typical time scale  $t_K$  for force build-up. Both time scales are expected to increase. Experimentally one finds that  $t_K$  is on

the order of  $\approx 10$  minutes for  $K \sim nN/\mu m$  [28], which is on the same order as typical maturation times for focal adhesions [69]. In the future one might extend this simple deterministic model to include strong cooperativity between bonds and stochastic effects [85] and perhaps also introduce explicit equations for feedback between effector and force generating system.

## 2.4 Summary

Both physical defects and active cells respond to elastic deformations in their environment and we suggest that the same mathematical formalism based on force multipoles and linear elasticity theory can be used to describe both situations. In fact, all formulae derived in this Chapter for interactions of cells with external strain, sample boundaries and other cells as quantified by  $W$  describe the corresponding interactions of physical dipoles as quantified by  $V^t$ , with  $W$  and  $V^t$  being related to each other simply by a switch in sign. For different situations of interest we found the same result  $\Delta W = P_{ij}u_{ij}$ , where  $u_{ij}$  is the strain tensor evaluated at the position of the force dipole  $P_{ij}$ . Depending on the situation of interest, this strain tensor can correspond to externally imposed strain, image strain induced by a sample boundary or strain due to the traction of other force dipoles. Our formula shows that cells can sense anisotropies in their environment only through an anisotropic probing process: if the probing process were isotropic,  $P_{ij} = P\delta_{ij}$ , we would find  $W = Pu_{ii}$  and cells could only sense the scalar quantity  $u_{ii}$  describing the local relative change in volume, but not any tensorial quantity like the direction of external strain.

It is important to note that the above equations for active cells are not interaction potentials in a strict physical sense. Rather these equations try to quantify information that cells can gain by pulling on their environment and show how external perturbations result in changes in effective stiffness. The experimental observation that active cells prefer large effective stiffness in their environment leads to the interaction laws for cells given in Eqs. (2.16,2.17,2.18). In this way, we can predict cellular self-organization in soft media from an extremum principle in elasticity theory, in excellent agreement with experimental results [53]. The structure formation for defect dipoles follows simply by inverting the sign of the interaction laws derived for active cells. This case might also apply to artificial or inert cells [48], e.g. for biomimetic systems, one might think of vesicles or nanocapsules which contract on adhesion to an elastic environment.

In regard to modeling of active cells, we assume that they probe their elastic environment through an anisotropic process in which force is of central importance, and that this process results in a cellular preference for large

effective stiffness in the environment. Although the phenomena described here are closely related to cell morphology and the dynamics of focal adhesions, these aspects are not the focus of this work. In particular, the magnitude  $P$  of the cellular force dipole tensor does not enter our predictions, in contrast to the positions and orientations represented by the dipole tensor  $P_{ij}$ . This reflects the fact that our model focuses on the extracellular properties that can be sensed by the cell. Since we avoid modeling cell morphology and dynamics of focal adhesions, we are able to describe the active behavior of cells in the same mathematical framework developed before to describe physical defects in a deformable medium. In particular, both cases require the solution of the corresponding elastic boundary value problem given in Eq. (2.8) and Eq. (2.9). In the next chapter, we present exact solutions for different cases of interest.

The assumption of a linear elastic medium holds true for most synthetic elastic substrates like PAAM or PDMS. The typical physiological environment for anchorage-dependent cells are physiological hydrogels like collagen matrices, whose mechanical properties are more difficult to model, in particular due to their viscoelastic and non-linear behaviour. Yet our calculations will show that our model has large predictive power also for this case, possibly because elastic deformations of hydrogels become encoded in plastic changes that later can be detected by active mechanosensing in a similar way as persistent elastic deformations.

Finally, in Section 2.3.3 we outlined how stiffness preference, the main assumption of our model, might be linked to mechanosensation at cell–matrix contacts by presenting a simple model for force build-up. During recent years, the regulated response to mechanical input by single cells has been studied experimentally in larger detail. There is a growing body of evidence that integrin-based cell-matrix contacts act as local mechanosensors which channel mechanical information about the environment directly into cellular decision making. Although this does not concern our modeling directly, we suggested that the preference of large effective stiffness might be a result of more efficient force generation in a stiffer environment favoring mechanical activity of cells. This might result in a larger signaling activity at cell–matrix contacts encountering a stiffer response from their environment, possibly enhanced by positive feedback loops favoring cell–matrix growth at stiff sites. In the long run, this could trigger a corresponding reorganization of the cytoskeleton. The main purpose of introducing the simple model was to illustrate how our coarse-grained phenomenological modeling might be extended to the subcellular scale in the future. However, these aspects are not the focus of the present work, where we aim at effects on the tissue scale. Thus, we prefer to keep stiffness preference as an assumption, since the exact underlying mechanism does not affect the results of the following chapters.

# Chapter 3

## Examples of Cell Organization

In this chapter we will study examples for cell organization of single cells and compare our predictions to experimental results. We are particularly interested in stiffness variations in homogeneous substrates with a constant Young modulus  $E$ , where anisotropies in effective stiffness are induced by external strain or sample boundaries. We first consider cells in a static homogeneous strain field. External strain fields could arise for example in a wounded part of a tissue. In a physiological context cells are often close to a boundary of a tissue or organ. To predict the effect of boundaries we study a semi-infinite space with a planar surface. As an example for a finite sized sample, we then consider the elastic sphere. In both cases, the elastic equations can be solved exactly. Since cells are modeled as anisotropic force dipoles, these calculations are in general more involved than similar calculations for isotropic force dipoles. Moreover, in contrast to earlier calculations for the physical case, we are interested not only in the effect of free, but also of clamped boundaries, which are known to induce mechanical activity of cells by increasing the effective stiffness. We conclude this chapter with a summary of our results and compare our theory to existing models of cell organization in the literature which are based on contact guidance.

### 3.1 External Strain

As an example for cell organization in a prestrained environment, we consider a homogeneously prestrained elastic slab with an uniaxial stress  $p$  acting along the z-axis. The other faces are traction free, i.e. the stress tensor has only one non-zero component,  $\sigma_{zz} = p$ . Then the corresponding strain tensor has only diagonal components  $u_{ij}^e = \frac{p}{E}\{(-\nu, 0, 0), (0, -\nu, 0), (0, 0, 1)\}$  independent of position. Contraction of this external strain tensor with the force-dipole

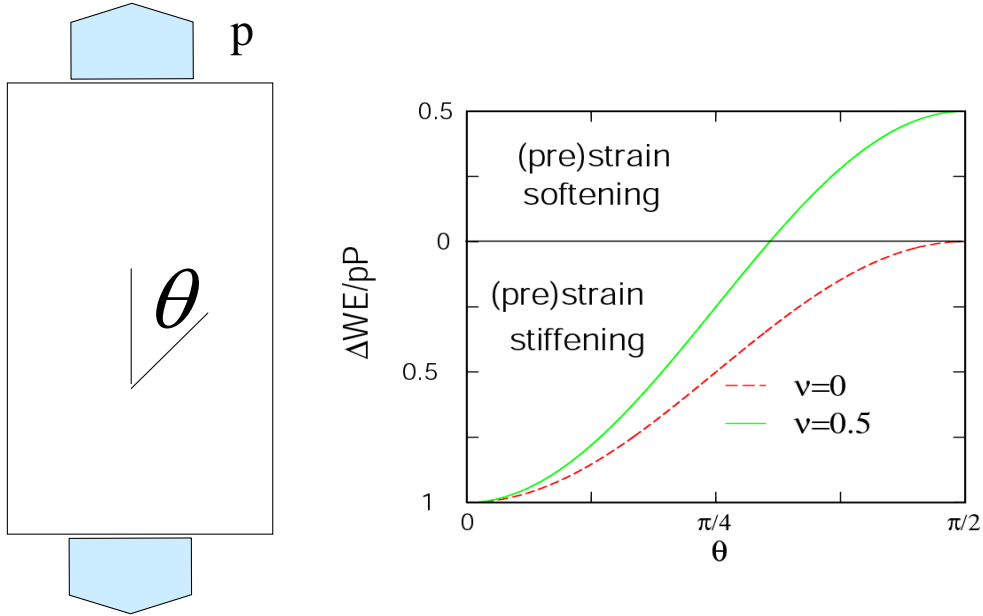


Figure 3.1:  $\Delta W^e$  induced by a homogeneous strain field as a function of probing direction  $\theta$ . Independent of  $\nu$ , cells prefer to orient along the direction of stretch on top of a prestrained elastic substrate or inside a strained physiological hydrogel.

tensor  $P_{ij}$  according to Eq. (2.16) leads to:

$$\Delta W^e = \frac{pP}{E} [(1 + \nu) \cos^2 \theta - \nu] , \quad (3.1)$$

where  $\theta$  is the orientation of the dipole relative to the direction of externally applied strain. Eq. (3.1) applies to both a cell on the top surface of the strained slab (elastic substrate) or inside a strained infinite elastic material (hydrogel).

For tensile strain ( $p > 0$ ), the cell senses maximal effective stiffness along the direction of stretch  $\theta = 0$ , thus cells orient preferentially in the direction of stretch in a prestrained environment. On the other hand, cells in a precompressed environment ( $p < 0$ ) will orient perpendicularly to the axis of compression, which is a combined effect of compressive strain avoidance in the z-direction and maximal tensile strain detection in the perpendicular directions, which will be most pronounced for incompressible media ( $\nu \approx 1/2$ ). Experimentally it is indeed observed that cells orient preferentially along the direction of stretch both for fibroblast on elastic substrates [11] and in collagen

gels [26,31]. Since  $\Delta W$  decreases with increasing rigidity  $E$ , the elastic effects discussed here will be observed only in a soft environment, namely with rigidity  $E$  around kPa, which is a typical physiological value for tissue stiffness. For stiffer substrates the variations in  $\Delta W$  for different probing directions might become too small to induce an orientation response and cells are expected to stay unpolarized. Note that if cells were probing the environment in a "pushing"  $P > 0$  rather than "pulling-mode"  $P < 0$ , compressive strain, rather than tensile strain, would be interpreted as an increase in effective stiffness.

Finally, we would like to mention that there exists a huge number of studies investigating the response of cells to *oscillatory* strain fields [92–95]. Usually studies are performed at 1Hz frequency, which is the physiological value of blood pulsation. Since here, cells are passively strained and deformed by forces acting from the outside, the response might be very different to the case discussed here, where cells actively sense and respond to a *static* stress in the environment. In fact, experiments suggest that cells in dynamic strain fields may avoid both tensile and compressive strain, i.e. minimize  $|P_{ij}u_{ij}|$  [92, 93]. Apart from  $+P_{ij}u_{ij}$  as for cells and  $-P_{ij}u_{ij}$  as for physical defects, this expression constitutes a third alternative of how cell orientation could be linearly coupled to an external strain field [48].

In contrast to cellular dipoles, a physical anisotropic contraction dipole causing a local contraction of the environment along its axis, is repelled (attracted) by tensile (compressive) strain, because the negative interaction energy with the medium is reduced (increased) due to the expansion (compression) of the environment caused by the external field. Physical defects therefore orient in the opposite way as mechanosensing cells with respect to external homogeneous strain.

## **3.2 Sample Boundaries: The Elastic Half Space**

In a physiological context cells are often close to boundaries, such as the surface of a tissue or organ. In addition to that, boundaries induced by implants could also alter cell organization in the surrounding tissue. Boundaries alter the strain with respect to an infinite homogeneous medium by a boundary induced image strain. To predict the effect of boundaries on cell organization we study here the interaction of a force dipole embedded in a semi-infinite space close to the surface with the planar boundary, which might be either rigidly fixed (clamped) or free.

### 3.2.1 The Elastic Boundary Value Problem

The elastic isotropic half space with a clamped surface at  $r_3 = 0$  constitutes a Dirichlet problem with vanishing displacements at the planar boundary,  $u_i(\vec{r}) = 0$  for  $r_3 = 0$ , whereas the free surface leads to a Neumann boundary value problem with vanishing surface tractions,  $\sigma_{ij}(\vec{r})n_j = 0$  for  $r_3 = 0$  with  $\vec{n} = (0, 0, 1)$  being the surface normal. The boundary value problem of the semi-infinite space can be solved using the concept of image singularities. Image approaches are well known from electrostatics: the simplest example is the charge in front of a metal plate. Here, the field due to a charge  $Q$  at  $\vec{r}' = (r'_1, r'_2, r'_3)$  with the boundary at  $r_3 = 0$  is equivalent to the field of the charge and an image charge  $-Q$  at  $\vec{r}'_{\text{im}} = (r'_1, r'_2, -r'_3)$  without a boundary [96]. In analogy, the displacement field due to a unit force at  $\vec{r}'$  close to a planar surface of a semi-infinite space is equivalent to the superimposed fields of a set of force nuclei placed in a homogeneous infinite substrate, i.e.:

$$G_{ij}(\vec{r}, \vec{r}') = G_{ij}^{\infty}(\vec{r}, \vec{r}') + G_{ij}^{\text{im}}(\vec{r}, \vec{r}'), \quad (3.2)$$

where  $G_{ij}^{\infty}$  is the Green function in an infinite medium and  $G_{ij}^{\text{im}}$  specifies its image system, which is a sum of functions derived from  $G_{ij}^{\infty}$  by differentiation (point images, i.e. forces and force dipoles) or integration (line images, i.e. a line of force nuclei). The Green function for an infinite medium is given by the Thompson solution [56]:

$$G_{ij}^{\infty}(\vec{r}, \vec{r}') = a_1^{\infty} \left\{ a_2^{\infty} \delta_{ij} + \frac{R_i R_j}{R^2} \right\} \frac{1}{R}, \quad (3.3)$$

where  $\vec{R} = \vec{r} - \vec{r}'$  and

$$a_1^{\infty} = \frac{1 + \nu}{8\pi E(1 - \nu)} = \frac{\Lambda + 1}{8\pi c}, \quad a_2^{\infty} = (3 - 4\nu) = \frac{3 + \Lambda}{1 + \Lambda}. \quad (3.4)$$

Despite its rather simple geometry, the image system of the elastic half-space is rather complicated and consists of up to 15 image nuclei, including point nuclei located at  $\vec{r}'_{\text{im}} = (r'_1, r'_2, -r'_3)$  and line images running normal to the surface and extending from  $-r'_3$  to infinity. The image system of the free half space was calculated by Mindlin using a Boussinesq-Galerkin representation [63]. The Green function of the clamped half-space has been derived by Phan-Thien applying a Papkovitch-Neuber ansatz, however without revealing the image system in detail [97]. Quite recently, Walpole [98] used methods of general harmonic potential theory and presented the image system for two joined half-spaces, which includes the clamped or free half-space as limiting cases of infinite or vanishing shear rigidity in one of the joined spaces.

Introducing the harmonic functions:

$$\frac{1}{s} = \frac{1}{|\vec{r} - \vec{r}'_{\text{im}}|}, \quad (3.5)$$

where  $s$  is the distance from the image point, and

$$\begin{aligned}\Phi &= \ln(r_3 + r'_3 + s) \\ \Psi &= (r_3 + r'_3)\Phi - s,\end{aligned}\tag{3.6}$$

the image Green tensor  $G_{ij}^{\text{im}}$  of the isotropic elastic half space reads [98]:

$$\begin{aligned}G_{ij}^{\text{im}}(\vec{r}, \vec{r}') &= MG_{ij}^{\infty}(\vec{r}, \vec{r}'_{\text{im}}) + \\ &+ \frac{Jr'_3(1+\nu)}{4\pi E(1-\nu)} \left[ s_{,ij3} - 2\delta_{j3}s_{,i33} - 4(1-\nu)\delta_{i3} \left[ \left( \frac{1}{s} \right)_{,j} - 2\delta_{j3} \left( \frac{1}{s} \right)_{,3} \right] \right] - \\ &- \frac{Jr'_3(1-2\nu)(1+\nu)}{2\pi E(1-\nu)} \delta_{j3} \left( \frac{1}{s} \right)_{,i} - \\ &- \frac{Jr_3'^2(1+\nu)}{4\pi E(1-\nu)} \left[ \left( \frac{1}{s} \right)_{,ij} - 2\delta_{j3} \left( \frac{1}{s} \right)_{,i3} \right] - \\ &- \frac{C(1-2\nu)(1+\nu)}{4\pi E(1-\nu)} (\Psi_{,ij} - 2\delta_{j3}\Psi_{,i3}) + \frac{B(1+\nu)}{2\pi E} \delta_{j3}\Phi_{,i} + \\ &+ \frac{B(1+\nu)}{2\pi E} (\delta_{i3}\Phi_{,j} - \delta_{ij}\Phi_{,3}),\end{aligned}\tag{3.7}$$

where the coefficients  $M, J, C, B$  depend on the boundary condition (subscripts: free  $f$ , clamped  $c$ ) and the Poisson ratio  $\nu$  [98]:

$$\begin{aligned}M^f &= (3 - 4\nu) & M^c &= -1 \\ J^f &= -1 & J^c &= 1/(3 - 4\nu) \\ C^f &= 2(1 - \nu) & C^c &= 0 \\ B^f &= 2(1 - 2\nu) & B^c &= 0.\end{aligned}\tag{3.8}$$

For a fixed  $j$ , each line in Eq. (3.7) represents the  $i$ -th component of the displacement field of one fundamental strain nuclei of an infinite medium. For a free surface, five image singularities contribute to a surface tangential or normal force component. A tangential force  $j = 1, 2$  introduces, in the order of lines of Eq. (3.7), three point images (force, double force with moment and a doublet) and two line images (line of doublets and line of double forces with moment) [63]. A normal force  $j = 3$  induces four point images (force, double force, doublet, center of compression/dilation) and a line of compression/dilation centers [63]. In a clamped half space the line images disappear ( $B = C = 0$ ) and there are only the three or four point images for a tangential or normal force component, respectively. Interestingly, the strength of the higher order point singularities is proportional to the distance  $r'_3$  of the source point from the surface. Hence their relative contribution to the displacement field with respect to the image force increases with increasing distance of the source force from the surface. Note that for  $r'_3 \rightarrow 0$ , i.e. for a force acting at a

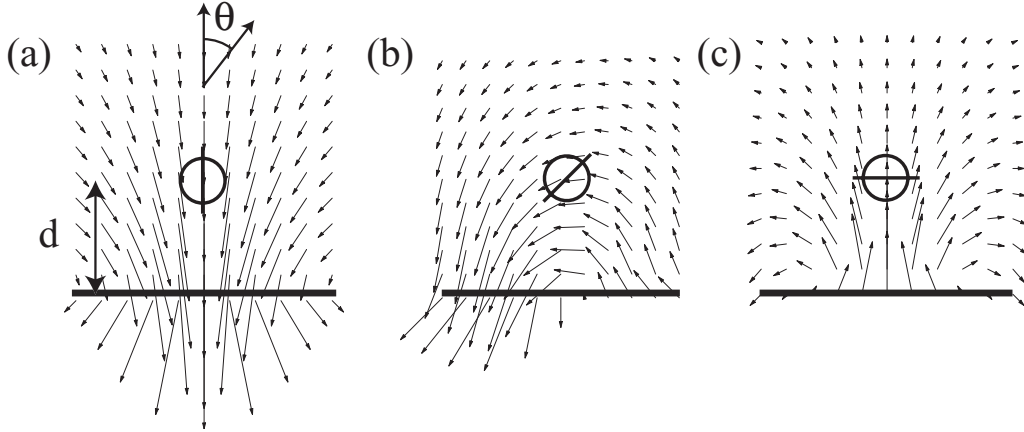


Figure 3.2: Image fields  $\vec{u}^b$  for a contraction dipole  $P_{ij}$  positioned at  $\vec{r}^j = (0, 0, d)$  in front of a clamped surface of a semi-infinite space for Poisson ratio  $\nu = 1/2$ . Dipole orientations are (a)  $\theta = 0$ , (b)  $\theta = \frac{\pi}{4}$  and (c)  $\theta = \frac{\pi}{2}$  with respect to the surface normal. At the clamped surface the image displacements  $\vec{u}^b$  balance the displacements  $\vec{u}^\infty$  of an infinite space. Inside the sample, they are homogeneous solutions of the elastic equations. The interaction of a dipole with the clamped surface is equivalent to the interaction of the dipole with a set of image singularities placed at  $\vec{r}_{\text{im}}^j = (0, 0, -d)$ . For a free surface, the normal tractions vanish and all image displacements change sign. For  $\nu < 1/2$ , there is an additional contribution to  $\vec{u}^b$  derived from line images. However, the interaction of force dipoles with the boundary does not change qualitatively as  $\nu$  is varied.

free surface of a semi-infinite space, Eq. (3.7) yields the well know Boussinesq Green function [56] for tangentially applied forces and the solution of Cerruti for normally applied forces [58]. The dominant terms to the image displacement field far away from the surface arise from the image force and the line images  $\sim 1/s$ , followed by the dipole type defects (double force, compression center)  $\sim r_3'/s^2$  and finally the doublet  $\sim r_3'^2/s^3$ . The Poisson ratio  $\nu$  changes the relative magnitude of the image singularities with respect to each other, but does not change their type (i.e. their sign). Therefore, strain propagation in the half space is expected to stay qualitatively similar with varying  $\nu$ . Changing the boundary condition from free to clamped, the point images flip their sign, which indicates that clamped and free boundary will induce qualitatively opposite effects. Indeed, for the special case of an incompressible medium,  $\nu = 1/2$ , clamped and free half space induce the same boundary fields, but with opposing signs.

The image displacements  $\vec{u}^b$  induced by a force dipole  $P_{ij}$  at  $\vec{r}^j$  are obtained from Eq. (3.7) by differentiation with respect to the primed coordinates.

Note that the planar surface at  $r_3 = 0$  breaks the translational invariance along the z-axis, which means that differentiation of  $G_{ij}^b$  with respect to  $r_3$  and  $r'_3$  are not equivalent. Since the strength of the dipolar singularities in  $G_{ij}^{\text{im}}$  is proportional to  $r'_3$ , taking the derivative with respect to  $r'_3$  will lead to dipole images of  $r'_3$ -independent strength that are proportional to the dipole strength  $P$ . Therefore, the far field image displacements produced by a force dipole in front of a planar surface are dominated by image dipole terms  $\sim 1/s^2$  of strength proportional to  $M$  and  $J$  and additional images derived from the line image terms. In Fig. 3.2 we plot  $\vec{u}^b$  for three different dipole orientations with respect to the surface normal of a clamped half space for Poisson ratio  $\nu = 1/2$ . In this case, for a free surface all image displacements point in the opposite direction.

### 3.2.2 Interactions with the Boundary

The change in effective stiffness encountered by a force dipole  $P_{ij}$  positioned a distance  $r'_3 = d$  away from the surface is inversely related to the effective interaction potential  $\Delta W^b(\vec{r}')$ , which according to Eq. (2.17) is proportional to the induced image strain at the position of the dipole, i.e.  $\Delta W^b(\vec{r}') = \frac{1}{2} P_{ij} \frac{\partial^2 G_{ik}^{\text{im}}(\vec{r}, \vec{r}')}{\partial r_j \partial r'_l} P_{kl} |_{\vec{r} \rightarrow \vec{r}'}$ . Because of rotational symmetry with respect to the surface normal, the surface induced change in effective stiffness sensed by a dipole depends only on its distance  $d$  to the surface and the angle  $\cos \theta = \vec{n} \cdot \vec{l}$  between dipole orientation and surface normal. We find:

$$\Delta W^b(d, \theta) = \frac{P^2}{256\pi E d^3} (a_\nu + b_\nu \cos^2 \theta + c_\nu \cos^4 \theta), \quad (3.9)$$

with the coefficients

$$\begin{aligned} a_\nu^f &= \frac{(1 + \nu)(5 + 2\nu(6\nu - 1))}{1 - \nu} & a_\nu^c &= -\frac{(1 + \nu)(15 + 32\nu(\nu - 1))}{(1 - \nu)(3 - 4\nu)} \\ b_\nu^f &= \frac{(1 + \nu)(22 + 4\nu(2\nu - 9))}{1 - \nu} & b_\nu^c &= -\frac{(1 + \nu)(34 + 32\nu^2 - 72\nu)}{(1 - \nu)(3 - 4\nu)} \\ c_\nu^f &= \frac{(1 + \nu)(13(1 - 2\nu) + 12\nu^2)}{1 - \nu} & c_\nu^c &= -\frac{(1 + \nu)(7 - 8\nu)}{(1 - \nu)(3 - 4\nu)} \end{aligned} \quad (3.10)$$

being rational function of the Poisson ratio  $\nu$ .  $\Delta W^b$  scales quadratically in  $P$  because the image strain scales linearly in  $P$ , in other words, the force dipole interacts with its own images. The interaction of the force dipole with the surface is a long-ranged effect and scales like a dipole-dipole interaction potential, that is  $\sim d^{-3}$ . For free and clamped surfaces, all coefficients in Eq. (3.10) are positive and negative, respectively, irrespective of  $\nu$ . Therefore, the preferred cell orientation close to the surface, i.e. the configurations of minimal  $\Delta W^b$ , are parallel ( $\theta = \pi/2$ ) and perpendicular ( $\theta = 0$ ) orientation

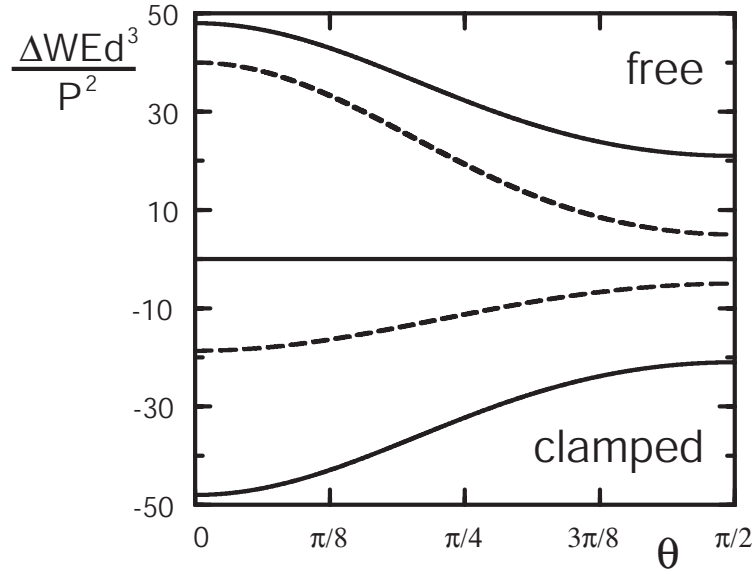


Figure 3.3: Angular dependence of image interaction with the boundary,  $\Delta W^b$  from Eq. (3.9), for a cellular force dipole positioned a distance  $d$  away from the surface of an elastic half space, plotted in units of  $P^2/Ed^3$  and rescaled by  $1/256\pi$ . Curves above and below the  $\theta$ -axis correspond to free and clamped boundaries, respectively. Solid and dashed lines correspond to  $\nu = 1/2$  and  $\nu = 0$ , respectively (all other Poisson ratios yield curves lying in between those shown). A clamped (free) surface effectively rigidifies (softens) the medium towards the surface. Hence, irrespective of the value of  $\nu$ , cells close to a clamped surface prefer to orient perpendicular ( $\Delta W^b$  minimal for  $\theta = 0$ ) while cells close to a free surface prefer parallel orientation ( $\Delta W^b$  minimal for  $\theta = \pi/2$ ).

for free and clamped boundaries, respectively. In Fig. 3.3 we plot the angular dependence of  $\Delta W^b$  for  $\nu = 1/2$  and  $\nu = 0$ . Since  $|\Delta W^b| \sim 1/d^3$  increases if  $d$  decreases, the overall mechanical activity of a cell increases towards a clamped surface ( $\Delta W < 0$ ), but decreases towards a free surface ( $\Delta W > 0$ ). Thus we predict that cells preferentially locomote towards a clamped boundary, but tend to migrate away from a free boundary. In general, free and clamped boundaries have always opposite effects. One may think of a clamped (free) surface as the interface between the medium and an imaginary medium of infinite (vanishing) rigidity, which effectively rigidifies (softens) the medium towards the boundary. Thus for clamped (free) boundary conditions, the cell senses maximal stiffness towards (away) from the boundary. For clamped boundaries, mechanical activity of cells is favored and cells can amplify this effect by adjusting orientation. For free boundaries, mechanical activity of cells is disfavored and the orientation response is an aversion response, see Fig. 3.4.

Experimentally, it is well known that mechanical activity of cells increases for clamped boundary conditions [99]. The predicted orientation effects close to boundaries have been observed numerous times, e.g. the parallel orientation of cells close to free surfaces [31]. Our model predicts the same orientation effects for an elastic substrate with two regions of different rigidities, see Fig. 3.4(c): cells on the soft and stiff sides of the boundary orient perpendicular and parallel to it, respectively. The transition from parallel to perpendicular orientation is a discrete transition and occurs, when the two Young moduli become equal, i.e. at  $E_1 = E_2$ . Indeed fibroblasts migrating from a soft to a stiff region keep their perpendicular orientation and cross over to the stiff side, while fibroblasts migrating from a stiff to a soft region do not cross the boundary, but turn by 90 degrees and move parallel to the boundary [13].

For the interaction of a physical dipole with the surface, we simply have to switch sign in Eq. (3.9). Hence, physical dipoles are attracted by free and repelled from clamped surfaces. A clamped surface prevents the defect from displacing its environment to lower its potential energy, which results in a repulsive interaction. In contrast, a free surface favors displacements close to the surface, since at a free surface there exist no internal restoring forces acting normal to the surface. This results in an attractive interaction of the defect with the surface. Since  $V^t \sim P^2$ , the sign of  $P$  does not matter, i.e. dilation and contraction dipole interact in the same way with the surface.

### 3.3 Sample Geometry: The Elastic Sphere

#### 3.3.1 The Elastic Boundary Value Problem

As an example for a finite sized sample, we consider the elastic sphere with radius  $R$ . For the elastic sphere, no image system has been constructed that solves the elastic boundary value problem and it is not clear whether such an image system exists. Nevertheless, the elastic equations for the elastic sphere can be solved analytically by applying an expansion in terms of vector spherical harmonics. This approach has been used by Hirsekorn and Siems [55] to solve the von Neumann problem of an anisotropic force dipole in an elastic sphere with a free boundary. We will follow this approach in order to solve the Dirichlet problem of a force dipole in a clamped sphere. Both results are then used to calculate the change in effective stiffness encountered by a force dipole in clamped and free spheres, respectively.

Analytical solutions to differential equations for scalar fields in spherical coordinates can be obtained by an expansion in terms of spherical harmonics, which form a complete orthonormal basis set on the unit sphere. In a similar

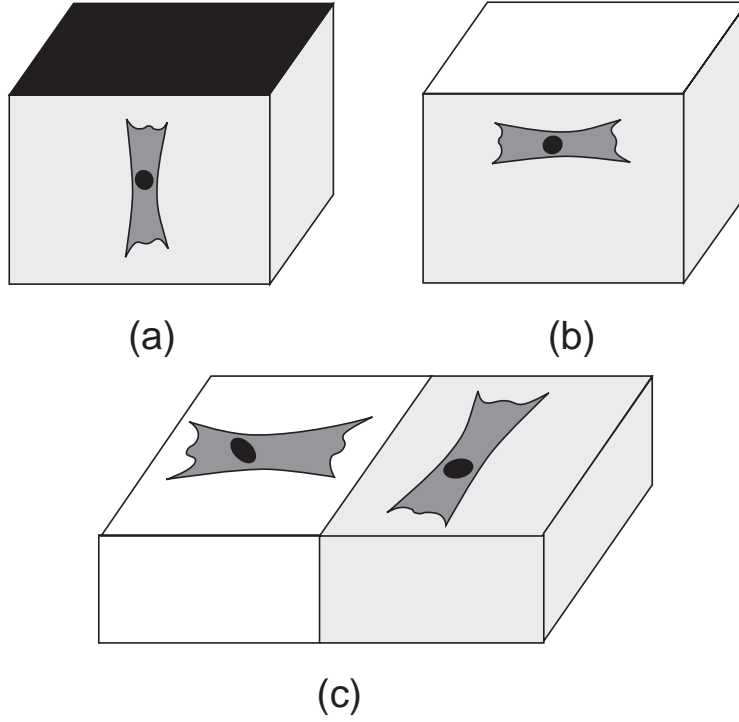


Figure 3.4: Predicted cell orientation in a physiological hydrogel close to a surface (a,b). Note that the additional cubic faces have only been included for illustration purposes. (a) Cells prefer the direction of maximal effective stiffness. Thus, they orient perpendicular to a clamped surface and motile cells prefer to locomote towards a clamped surface. (b) For a free surface, this direction is parallel to the surface and motile cells tend to avoid the boundary. (c) Cells on an elastic substrate close to a boundary between soft (left) and rigid (right) regions prefer analogous orientations as cells close to clamped and free surfaces in a physiological hydrogel, respectively.

way, the general solution to the equilibrium condition Eq. (2.10) for the vector field  $\vec{u}(\vec{r})$  can be expressed as a sum over so-called *vector spherical harmonics* (VSH):

$$\vec{u}(r, \Omega) = \sum_{lm} \left( f_{lm}(r) \mathbf{Y}_{l+1m}^\dagger(\Omega) + g_{lm}(r) \mathbf{Y}_{l-1m}^\dagger(\Omega) + h_{lm}(r) \mathbf{Y}_{lm}^\dagger(\Omega) \right). \quad (3.11)$$

Vector spherical harmonics  $\mathbf{Y}_{JLM}(\Omega)$  form a complete orthonormal basis set on the unit sphere [100]:

$$\int \mathbf{Y}_{JLM}(\Omega) \mathbf{Y}_{J'L'M'}^\dagger(\Omega) d\Omega = \delta_{JJ'} \delta_{LL'} \delta_{MM'}. \quad (3.12)$$

They are the eigenfunctions of the angular momentum operator  $\mathbf{J}$  of a vector field as spherical harmonics  $Y_{lm}$  are the eigenfunctions of the (orbital) angular

momentum  $L$  of a scalar field.  $\mathbf{J}$  is the vector sum  $\mathbf{J} = \mathbf{L} + \mathbf{S}$  of the orbital momentum  $\mathbf{L}$  and the intrinsic spin  $\mathbf{S}$ . The eigenvectors of  $\mathbf{S}$  are the spherical basis vectors  $\mathbf{e}_\alpha$ :

$$\mathbf{e}_{\pm 1} = -\frac{1}{\sqrt{2}}(\mathbf{e}_x \pm \mathbf{e}_y), \quad \mathbf{e}_0 = \mathbf{e}_z \quad (3.13)$$

and represent a spin  $S = 1$  system. Since  $\mathbf{J}$  is an example of angular momentum addition, one can construct the VSH with the help of Clebsch Gordon coefficients  $C_{M-\alpha}^l \frac{1}{\alpha} \frac{J}{M}$  [100]:

$$\mathbf{Y}_{JM}(\Omega) = \sum_{\alpha} C_{M-\alpha}^l \frac{1}{\alpha} \frac{J}{M} Y_{lM-\alpha}(\Omega) \mathbf{e}_{\alpha}. \quad (3.14)$$

This implies that for a given  $J$  there are only three classes of VSH, namely  $l = J, J \pm 1$ , which in retrospective justifies our ansatz Eq. (3.11).

In order to solve the boundary value problem, we split  $\vec{u}$  again into a contribution in an infinite substrate  $\vec{u}^\infty$  and a boundary induced field  $\vec{u}^b$ .  $\vec{u}^\infty$  is the solution to the inhomogenous differential equation Eq. (2.10) with a body force density and thus ensures force balance everywhere inside the sample. For a force dipole  $P'$  located at  $\vec{r}'$  the VSH-expansion of the displacement field  $\vec{u}^\infty(\vec{r})$  reads for  $r' < r$  [55]:

$$\begin{aligned} \vec{u}^\infty(\vec{r}) &= \frac{1}{c} \sum_{lm} \frac{\mathbf{Y}_{ll+1m}^\dagger(\Omega)}{(2l+1)r^2} X_{lm}^{\alpha\beta}(\eta', \Omega') P'_{\alpha}{}^{\beta} - \\ &- \frac{1}{c} \sum_{lm} \frac{\mathbf{Y}_{ll-1m}^\dagger(\Omega)}{(2l+1)r^2} (3l+2+(l+1)\Lambda) C_{m-\alpha}^{l-1} \frac{1}{\alpha} \frac{l}{m} A_{l-2m}^{\alpha\beta}(\Omega') \eta'^{l-2} P'_{\alpha}{}^{\beta} - \\ &- \frac{1}{c} \sum_{lm} \frac{\mathbf{Y}_{llm}^\dagger(\Omega)}{r^2} (2+\Lambda) C_{m-\alpha}^l \frac{1}{\alpha} \frac{l}{m} A_{l-1m}^{\alpha\beta}(\Omega') \eta'^{l-1} P'_{\alpha}{}^{\beta}, \end{aligned} \quad (3.15)$$

where  $\eta' = \frac{r'}{r} < 1$  and

$$\begin{aligned} A_{lm}^{\alpha\beta}(\Omega) &= \sqrt{\frac{l+1}{2l+1}} C_{m-\alpha}^{l+1} \frac{1}{\beta} \frac{l}{l-\alpha+\beta} Y_{lm-\alpha+\beta}(\Omega) \\ B_{lm}^{\alpha\beta}(\Omega) &= \sqrt{\frac{l}{2l+1}} C_{m-\alpha}^{l-1} \frac{1}{\beta} \frac{l}{m-\alpha+\beta} Y_{lm-\alpha+\beta}(\Omega) \\ X_{lm}^{\alpha\beta}(r, \Omega) &= -(3l+1+l\Lambda) C_{m-\alpha}^{l+1} \frac{1}{\alpha} \frac{l}{m} A_{lm}^{\alpha\beta}(\Omega) r^l + \sqrt{l(l+1)} (1+\Lambda) C_{m-\alpha}^{l-1} \frac{1}{\alpha} \frac{l}{m} \\ &\cdot [B_{lm}^{\alpha\beta}(\Omega) r^l + \frac{1}{2} A_{l-2m}^{\alpha\beta}(\Omega) r^{l-2} ((2l-1) - (2l+1)r^2)]. \end{aligned} \quad (3.16)$$

Sums over repeated indices are always implied except for Clebsch-Gordon coefficients.  $P'_{\alpha}{}^{\beta}$  is the force dipole tensor in the spherical basis set given by Eq. (3.13). The reciprocal basis vectors are  $\mathbf{e}^\alpha = \mathbf{e}_\alpha^\dagger = (-1)^\alpha \mathbf{e}_{-\alpha}$  and the

metric tensor is  $g_{\alpha\beta} = (-1)^\beta \delta_{\alpha,-\beta}$ . Spherical coordinates transform via the unitary operator  $U_{\alpha i} = (\mathbf{e}_\alpha \cdot \mathbf{e}_i)$  into cartesian coordinates, i.e.

$$P_{ij} = U_{\alpha i} U_{\beta j} P^{\alpha\beta}. \quad (3.17)$$

In order to satisfy force balance inside the sphere volume, the boundary induced field  $\vec{u}^b$  must be a homogenous solution to Eq. (2.10). Thus, inserting Eq. (3.11) into Eq. (2.10), one obtains a set of differential equations for the radial functions  $f_{lm}(r)$ ,  $g_{lm}(r)$  and  $h_{lm}(r)$  of the boundary induced field [55]:

$$0 = (3l + 2 + (l + 1)\Lambda)(f_{lm}'' + \frac{2}{r}f_{lm}' - \frac{(l + 1)(l + 2)}{r^2}f_{lm}) - \sqrt{l(l + 1)}(1 + \Lambda)(g_{lm}'' - \frac{2l - 1}{r}g_{lm}' + \frac{(l - 1)(l + 1)}{r^2}g_{lm}) \quad (3.18)$$

$$0 = (3l + 1 + l\Lambda)(g_{lm}'' + \frac{2}{r}g_{lm}' - \frac{l(l - 1)}{r^2}g_{lm}) - \sqrt{l(l + 1)}(1 + \Lambda)(f_{lm}'' + \frac{(2l + 3)}{r}f_{lm}' + \frac{l(l + 2)}{r^2}f_{lm}) \quad (3.19)$$

$$0 = h_{lm}'' + \frac{2}{r}h_{lm}' - \frac{l(l + 1)}{r^2}h_{lm}. \quad (3.20)$$

The general solution to Eq. (3.18)-Eq. (3.20) with a  $\vec{u}^b$  which is analytic at the sphere origin is [55]:

$$f_{lm}(r) = a_{lm} \frac{3l + 1 + l\Lambda}{(1 + \Lambda)(2l + 3)} r^{l+1} \quad (3.21)$$

$$g_{lm}(r) = a_{lm} \frac{1}{2} \sqrt{l(l + 1)} r^{l-1} (r^2 - R^2) + b_{lm} \frac{1}{2} r^{l-1}$$

$$h_{lm}(r) = c_{lm} r^l,$$

where  $R$  is the radius of the sphere and the remaining constants  $a_{lm}$ ,  $b_{lm}$  and  $c_{lm}$  must be determined by the boundary conditions at the sphere surface.

The Dirichlet problem of a clamped sphere yields:

$$\vec{u}^b(R, \Omega) = -\vec{u}^\infty(R, \Omega), \quad (3.22)$$

i.e. the expansion coefficients  $a_{lm}^c$  etc. of the boundary induced field can be found by matching  $\vec{u}^\infty$  and  $\vec{u}^b$  at the sphere surface:

$$\begin{aligned} a_{lm}^c &= -\frac{1}{cR^3} \frac{(2l + 3)(1 + \Lambda)}{(2l + 1)(3l + 1 + l\Lambda)R^l} X_{lm}^{\gamma\delta}(\rho', \Omega') P'_{\gamma\delta} \\ b_{lm}^c &= \frac{2}{cR^3} \frac{3l + 2 + (l + 1)\Lambda}{2l + 1} \left(\frac{\rho'}{R}\right)^{l-2} C_{m-\gamma}^{l-1} C_{\gamma m}^l A_{l-2m}^{\gamma\delta}(\Omega') P'_{\gamma\delta} \\ c_{lm}^c &= \frac{1}{cR^3} (2 + \Lambda) \left(\frac{\rho'}{R}\right)^{l-1} C_{m-\gamma}^l C_{\gamma m}^l A_{l-1m}^{\gamma\delta}(\Omega') P'_{\gamma\delta}, \end{aligned} \quad (3.23)$$

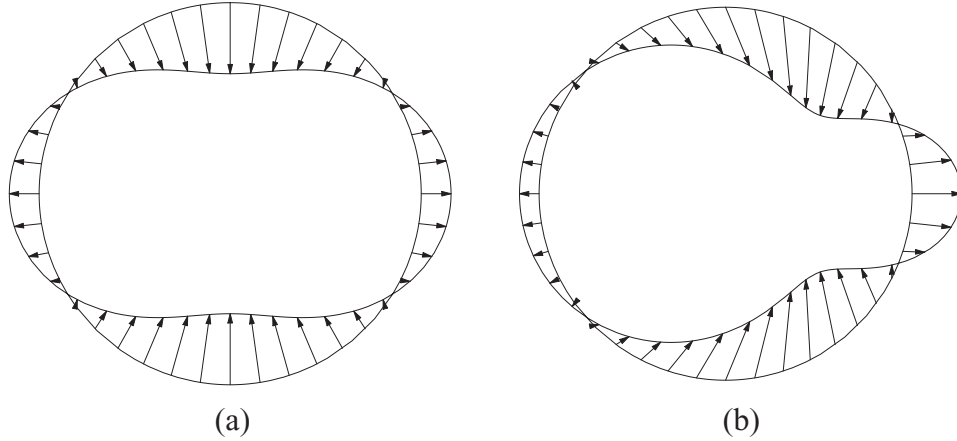


Figure 3.5: Deformation of an elastic sphere ( $R = 1$ ,  $\Lambda = 2$ ,  $c = 1$ ) with a free surface by a contraction dipole oriented in the  $z$ -direction. In (a) the dipole is placed at the origin,  $\vec{r} = (0, 0, 0)$ . In (b) the dipole is placed off-center at  $\vec{r} = (\frac{R}{4}, 0, 0)$ . The pictures show a cut through the  $x$ - $z$ -plane, but it has rotational symmetry only in (a).

where  $\rho' = r'/R$  is the ratio of the distance  $r'$  of  $P'$  to the sphere center and the sphere radius  $R$ . For a sphere with a free surface normal stress has to vanish and the corresponding Neumann boundary condition reads:

$$\sigma_{ij}^b \left( \frac{x_j}{r} \right)_{r=R} = -\sigma_{ij}^\infty \left( \frac{x_j}{r} \right)_{r=R}. \quad (3.24)$$

To determine  $a_{lm}^f$  etc. one first has to calculate the stress-tensor  $\sigma_{ij}^\infty$  and then balance the normal stress with the corresponding boundary induced stress  $\sigma_{ij}^b$  at  $r = R$ . The final result for the expansion coefficients in a free sphere is [55]:

$$\begin{aligned} a_{lm}^f &= \frac{1}{cR^3} \frac{2(1+\Lambda)(2l+3)(l+2)}{(2l+1)M(l)R^l} X_{lm}^{\gamma\delta}(\rho', \Omega') P'_{\gamma\delta} \\ b_{lm}^f &= -\frac{1}{cR^3} \frac{2(l^2+l+1) + (2l^2+1)\Lambda}{(l-1)(2l+1)} C_{m-\gamma\gamma m}^{l-1\ 1\ l} \left( \frac{\rho'}{R} \right)^{l-2} A_{l-2m}^{\gamma\delta}(\Omega') P'_{\gamma\delta} \\ c_{lm}^f &= -\frac{1}{cR^3} \frac{(l+2)(2+\Lambda)}{l-1} \left( \frac{\rho'}{R} \right)^{l-1} C_{m-\gamma\gamma m}^l A_{l-1m}^{\gamma\delta}(\Omega') P'_{\gamma\delta} \end{aligned} \quad (3.25)$$

with

$$M(l) = 2(l^2 + 1 + l) + (2l^2 + 4l + 3)\Lambda. \quad (3.26)$$

For both boundary conditions the image displacements scale  $\sim 1/R^2$  with the sphere radius and the VSH-expansion of  $\vec{u}^b$  converges as  $\sim l^2(\rho\rho')^l$ . Thus, higher  $l$ -moments dominate if the dipole is close to the surface ( $\rho' \rightarrow 1$ ). These are localized near the surface and decay rapidly towards the sphere center. We furthermore see that for a dipole close to the surface the convergence

properties of the series expansion are rather poor and more  $l$ -terms need to be considered to approximate the displacement field near the surface. Again clamped and free boundary induce opposing boundary fields as indicated by the opposite signs of the expansion coefficients: a clamped surface decreases  $\vec{u}$  to zero at the boundary whereas a free boundary enhances the displacements at the boundary. In Fig. 3.5 we plot two examples for a deformed elastic sphere with free boundaries under the action of a contraction dipole.

### 3.3.2 Effects in an Elastic Sphere

The change in effective stiffness sensed by a contraction dipole at  $\vec{r}'$  in an elastic sphere is inversely related to the effective boundary interaction potential  $\Delta W^b(\vec{r}') = P_{ij}u_{ij}^b$ . To calculate  $\Delta W^b(\vec{r}')$ , we need to contract the gradient-displacement tensor of the boundary induced field with the dipole tensor. This is most conveniently done using the spherical representation, i.e.:

$$\Delta W^b(\vec{r}') = \frac{1}{2}P^\alpha{}_\beta u^b{}_{\alpha,\beta}(\vec{r} \rightarrow r', \vec{r}') = \frac{1}{2}P^\alpha{}_\beta (\mathbf{e}_\beta^\dagger \cdot \nabla)(\mathbf{e}_\alpha \cdot \mathbf{u}^b). \quad (3.27)$$

Starting from the ansatz Eq. (3.11) for  $\vec{u}$ ,  $u_\alpha{}^\beta(\vec{r}, \vec{r}')$  can be derived by applying the gradient formula for spherical harmonics [100]:

$$\begin{aligned} \nabla \Phi(r) Y_{lm}(\Omega) &= -\sqrt{\frac{l+1}{2l+1}} \left( \frac{d}{dr} - \frac{l}{r} \right) \Phi(r) \mathbf{Y}_{l+1m}(\Omega) \\ &+ \sqrt{\frac{l}{2l+1}} \left( \frac{d}{dr} + \frac{l+1}{r} \right) \Phi(r) \mathbf{Y}_{l-1m}(\Omega), \end{aligned} \quad (3.28)$$

and furthermore the symmetry relationships of Clebsch Gordon coefficients [100]:

$$\begin{aligned} C_{m_1 m_2 m_3}^{j_1 j_2 j_3} &= (-1)^{j_2+m_2} \sqrt{\frac{2j_3+1}{2j_1+1}} C_{-m_2 m_3 m_1}^{j_2 j_3 j_1} \\ C_{m_1 m_2 m_3}^{j_1 j_2 j_3} &= (-1)^{j_1+j_2-j_3} C_{-m_1 -m_2 -m_3}^{j_1 j_2 j_3}. \end{aligned} \quad (3.29)$$

We finally find:

$$\begin{aligned} u^b{}_{\alpha}{}^\beta(\vec{r}, \vec{r}') &= \sum_{lm} R^l \frac{a_{lm}}{1+\Lambda} X_{lm}^{*\alpha\beta} \left( \frac{r}{R}, \Omega \right) \\ &- (2l+3)r^l A_{lm}^{*\alpha\beta}(\Omega) \left( \frac{b_{l+2m}}{2} C_{m-\alpha}^{l+1}{}_{\alpha m}{}^{l+2} + c_{l+1m} C_{m-\alpha}^{l+1}{}_{\alpha m}{}^{l+1} \right). \end{aligned} \quad (3.30)$$

Note that the  $m$ -sums over  $b_{lm}$  and  $c_{lm}$  run in the intervals  $[-l-2, l+2]$  and  $[-l-1, l+1]$ , respectively.

The effective interaction potential  $\Delta W^b$  for an elastic sphere is then found by inserting the appropriate expansion coefficients  $a_{lm}$ , etc. given in

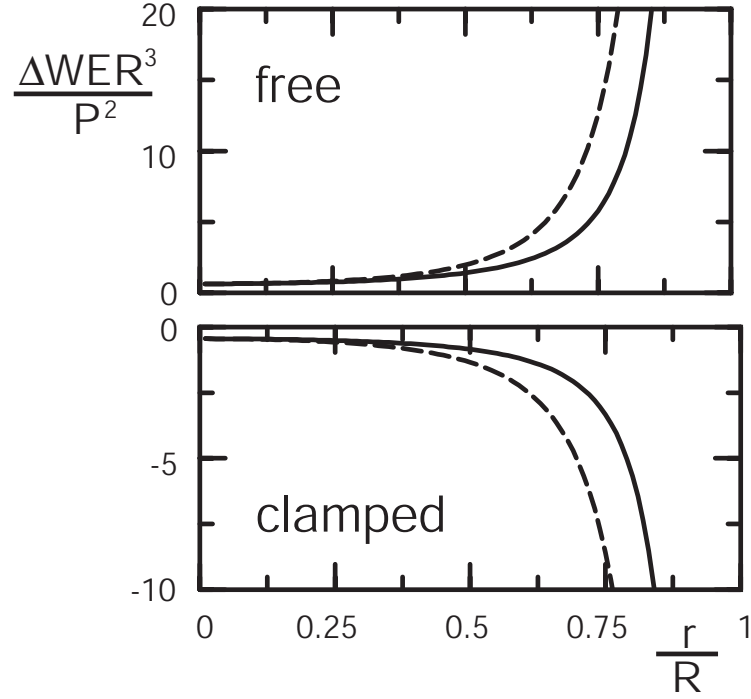


Figure 3.6: Image interaction  $\Delta W^b$  from Eq. (3.31) between the surface and a cellular force dipole embedded in an elastic sphere of radius  $R$  with  $\nu = 1/3$ , plotted in units of  $P^2/ER^3$  as a function of distance  $r/R$  to the sphere surface and rescaled by  $15/8$ . Curves above and below the  $r$ -axis correspond to free and clamped boundary conditions, respectively. Solid and dashed line correspond to orientations  $\theta = \pi/2$  and  $\theta = 0$  with respect to the surface normal. As for the half space, optimal cell orientation yields  $\theta = 0$  (clamped) and  $\theta = \pi/2$  (free) respectively.

Eqs. (3.23,3.25) and contracting  $u_\alpha^\beta$  with  $P^\alpha_\beta = P'^\alpha_\beta$ . We may rewrite  $\Delta W^b$  to indicate the important scaling laws of the interaction of the dipole with the sphere surface by:

$$\Delta W^b = \frac{P^2}{ER^3} f_\nu\left(\frac{r}{R}, \theta\right), \quad (3.31)$$

where  $r$  is the distance to the sphere center and  $\theta$  is the dipole orientation with respect to the surface normal. The function  $f_\nu$  contains the sum over all angular momenta and does not vary qualitatively as  $\nu$  (or, equivalently,  $\Lambda$ ) is varied.

With regard to cell orientation, we find the same results as for the elastic half space: cells will orient parallel (perpendicular) to a free (clamped) surface, respectively. As shown in Fig. 3.6, we also find a similar result for the effect of distance to the surface: for free (clamped) boundary conditions, a

small (large) distance to the sphere center is more favorable, since the surface favors (disfavors) mechanical activity. The new aspect here is the role of the sphere radius  $R$ . Since  $|\Delta W|$  increases when  $R$  decreases, one can effectively rigidify (soften) a material with a clamped (free) surface by reducing system size. Our predictions could be tested using e.g. fibroblast-populated collagen microspheres, an assay which has been introduced to study compaction of tissue equivalents at high cell density [101]. Since here we are mainly concerned with single cell effects, we suggest to modify this assay in such a way as to monitor the organization of isolated cells close to the sphere surface at low cell density and as a function of varying sphere radius.

For the interaction of a physical dipole with the surface embedded in an elastic sphere, we once more obtain the opposite results. Dipoles are attracted (repelled) and orient towards (away from) a free (clamped) surface.

### 3.4 Summary and Discussion

We have applied the general formalism from Chapter 2 to derive predictions for the organization of single cells in response to mechanical input for different situations of practical interest. In general, we found that physical and cellular force dipoles interact in opposite ways with external strain field or sample boundaries because  $V_t = -W$ . We also found that in general, free and clamped boundaries will have opposite effects. For example, cellular anisotropic force dipoles are repelled and attracted by free and clamped boundaries, respectively. In the vicinity of these boundaries, they will align in parallel and perpendicular, respectively. In general, all the interaction laws derived here show the universal scaling  $W \sim (P^2/El^3)f_\nu(\theta)$ , where  $f$  is a non-trivial function of Poisson ratio  $\nu$  and the orientation angles  $\theta$ , which has to be calculated for each situation of interest. Except for the case of external strain, the cellular force pattern interacts with itself (case of boundaries) or with another cellular force pattern (case of elastic interaction of cells as will be discussed in Chapter 4), therefore  $W \sim P^2$ . The scaling  $W \sim 1/l^3$  is typically for force dipoles. Here the length  $l$  can either be distance (e.g. between cell and boundary or between two cells) or sample size (in the elastic sphere). Finally,  $W \sim 1/E$ . Although  $W$  decreases with increasing Young modulus  $E$ , that is elastic effects become smaller, at the same time mechanical activity of cells usually increases. For this reason, we expect that there exists a range of optimal values for  $E$  for which the elastic effects in cell adhesion described here should be most pronounced (possibly around  $E = kPa$ , the physiological order of magnitude for cell and tissue stiffness).

Our model is able to explain numerous experimental observations that have been reported for organization of cells (especially fibroblasts) both on

elastic substrates and in physiological hydrogels [53]. The excellent agreement of our results with experiments suggests that cell organization can be predicted from local mechanical properties which the cell actively senses in its environment. The only property of cellular regulation which enters our model is the assumption that cells locally prefer large effective stiffness. Otherwise our modeling focuses on the elastic properties of the extracellular environment. Modeling the soft environment of cells as an isotropic elastic medium is certainly a good assumption for elastic substrates. However, the situation is more complicated for physiological hydrogels, in particular because they might not behave elastically and because they feature fiber degrees of freedom.

In fact, cell organization in gels is often explained by contact guidance, the alignment of cells along topographic features like collagen fibers. Since fibers can become aligned due to cell traction, contact guidance provides a long-ranged and persistent mechanism for cellular self-organization in tissue equivalents [51]. This process has been modeled before. In the theory of Ref. [51], flux equations for cellular and matrix densities are combined with mechanical equations which include cells as centers of isotropic contraction. This might be a good model for chondrocytes, which tend to show a spherical morphology. The anisotropic biphasic theory (ABT) from Ref. [52, 102] aims at cells like fibroblasts and smooth muscle cells, whose typical morphology in tissue equivalents is bipolar. ABT introduces a cell orientation tensor, which is coupled to a fiber orientation tensor, since cells are assumed to react foremost to fiber degrees of freedom. In our model, the force dipole tensor represents cell orientation as does the cell orientation tensor in ABT, but it is coupled to elastic degrees of freedom, since cells are assumed to react foremost to large effective stiffness. Since models for contact guidance in tissue equivalents focus on fiber degrees of freedom and high cell densities, they do not explain the single cell responses observed on elastic substrates, where contact guidance usually is ruled out [11, 13, 14].

The large predictive power of our model for elastic substrate experiments suggests that active mechanosensing by single cells might also be involved with cell organization in hydrogels. However, for the collagen assay from Ref. [103] it has been shown that as a response to external strain, fibers become rearranged and stress relaxes towards zero. In a matrix which cannot support any stress, our elastic considerations do not apply and contact guidance through formerly aligned fibers might be the only relevant clue for cell organization [103]. However, it is important to note that in our model, stress is actively generated by cells and thus needs to be supported only over time scales in which the cell actively senses the mechanical properties of its environment. In particular, if fiber alignment has resulted in some anisotropic mechanical environment, the cell might sense the anisotropic mechanical response of the matrix and orient itself correspondingly. This might explain why cells have been found to align to

a greater extent with respect to external strain than the surrounding collagen fibrils [103] and why our modeling is also successful for hydrogels.

We also want to point out that contact guidance is a bidirectional clue and provides only guidance, in contrast to external elastic strain, which provides taxis. In our model, taxis is reflected by the position dependence of  $\Delta W$ . For example, our theory not only predicts that cells prefer to orient parallel to free boundaries, but also that cells prefer to move away from them. Moreover a simple preference for cell alignment along fibers does not predict what cells do if they encounter a fiber junction in the gel. Our modeling would suggest that cells prefer the fiber under largest tension, exactly as has been observed experimentally for neutrophils migrating in human amnion [104]. In general, future experiments are needed to clarify the relative importance of topographic versus mechanical clues for cell organization in physiological hydrogels, while future modeling is needed to account for the mechanical (in particular, viscoelastic) properties of physiological hydrogels.

# Chapter 4

## Elastic Interactions of Cells

So far, we have focused on the organization of *single* cells due to elastic effects and found that cells interpret strain as variations in effective stiffness. Strain might be caused by external forces or induced by a boundary as studied in the previous chapter. Cellular traction forces also cause strain, which acts as external strain for other cells. This amounts to an elastic interaction between cells. Elastic interactions provide an appealing alternative to biochemical signals, since they are long-ranged, propagate quickly, and often provide spatially anisotropic signals. From this chapter on we will focus on *collective effects* of cells. We first derive elastic interaction laws for force dipoles on an elastic half-space (2D) and in an infinite medium (3D) and study the resulting structure formation analytically. We then focus on strings of aligned dipoles. Using methods of complex analysis we present analytical results for the interaction between two parallel strings and a string and a stack of dipoles, respectively.

### 4.1 Elastic Interactions of Force Dipoles

Mechanically active cells adhering to an elastic substrate can interact elastically with each other according to Eq. (2.18). However, although active mechanosensing might be used by any cell-type in principle, elastic interactions are likely to be limited to adhesion-dependent cells with strong mechanical activity like fibroblasts, such that strain fields become large enough to be detectable by other cells. To study elastic interactions we need to model the *overall* force patterns of cells in addition to the cellular probing pattern. Even if cells are initially isotropic, they sense anisotropic strain and start to polarize (this sometimes happens also spontaneously, e.g. in the presence of certain growth factors). The typical overall force pattern of a bipolarized fibroblast is shown in Fig. 4.1. The overall mechanical activity of fibroblasts resembles an anisotropic force contraction dipole oriented along the long axis of

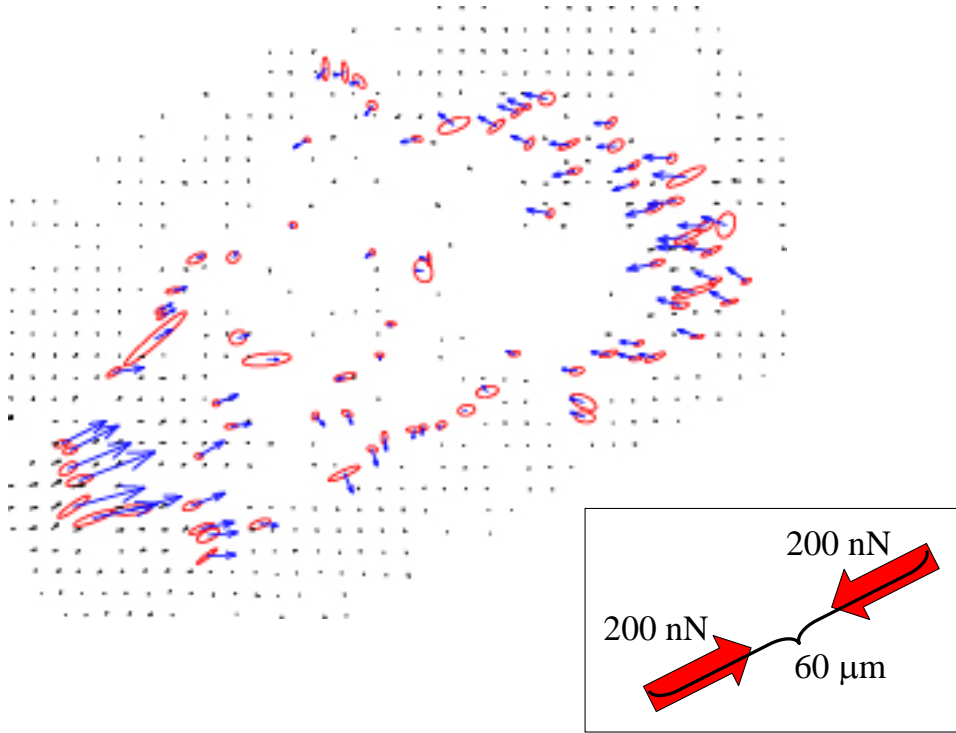


Figure 4.1: Typical force pattern of a fibroblast measured with the elastic substrate method in combination with microstructuring techniques [37]. The overall force pattern of a (bi)polarized fibroblast reflects an anisotropic contraction dipole with  $P \approx 10^{-11}\text{J}$ , which corresponds to two opposing forces of  $200\text{nN}$  separated by  $60\mu\text{m}$ . In this chapter we model the overall mechanical activity of cells in the framework of the force dipole concept and study elastic interactions of contraction dipoles.

the cell. Whereas in the preceding chapters the force dipole concept was used to model cellular probing during active mechanosensing, we apply the same concept here to model typical force patterns of cells in order to study elastic interactions between contraction dipoles. For simplicity we assume that the dipole strength  $P \approx 10^{-11}\text{J}$  is a constant. In analogy to the previous chapters, we ask: in what way does a cell orient its mechanical activity in order to sense maximal effective stiffness in its environment due to the traction of other cells? We will now first derive elastic interaction laws between contraction dipoles on elastic substrates and in 3D hydrogels by calculating  $\Delta W$  for arbitrary configurations of the two dipoles. These interaction laws will play the same role as interaction potentials for physical defects and might be considered as *effective* interaction potentials. By switching the signs of the interaction laws we obtain the corresponding interaction potentials  $V^t$  for physical dipoles.

### 4.1.1 Dipoles on Elastic Half Space

We first consider cells on top of an elastic substrate. If the thickness of the substrate is much larger than the elastic displacements on the top surface, it can be modeled as a semi-infinite elastic space [37]. The Green function for a force applied to the surface of a semi-infinite space is given by the well known Boussinesq solution [56]. Since tangential forces are expected to be much larger than normal forces, i.e. the  $x$  and  $y$ -components of  $P_{ij} = Pl_i l_j$  are much larger than the  $z$ -components, the Green function can be restricted to the  $x$ - $y$ -plane.  $\vec{l}$  denotes the orientation of the dipole. Moreover the normal displacement component contributes very little to the elastic interaction and we may use the two-dimensional (2D) Green function, i.e. only the  $x$ - and  $y$ -components of the Boussinesq solution:

$$G_{ij}^{2D}(\vec{r}, \vec{r}') = a_1 \left\{ a_2 \delta_{ij} + \frac{R_i R_j}{R^2} \right\} \frac{1}{R}, \quad (4.1)$$

where  $\vec{R} = \vec{r} - \vec{r}'$  and

$$a_1 = \frac{\nu(1+\nu)}{\pi E} = \frac{\Lambda(\Lambda+2)}{4\pi c(1+\Lambda)}, \quad a_2 = \frac{1-\nu}{\nu} = \frac{2+\Lambda}{\Lambda}. \quad (4.2)$$

It is convenient to define the angles  $\theta$ ,  $\theta'$  and  $\alpha$  via the scalar products  $\cos \theta = \vec{l} \cdot \vec{R}/R$ ,  $\cos \theta' = \vec{l}' \cdot \vec{R}/R$  and  $\cos \alpha = \vec{l} \cdot \vec{l}'$ . Then the effective interaction potential  $\Delta W^{PP'}$  for cells interacting through elastic media is derived from Eq.(2.19), which relates inversely to change in effective stiffness encountered by one cell due to the traction of the other. We find

$$\Delta W^{PP'} = a_1 \frac{PP'}{R^3} f(\theta, \theta', \alpha) \quad (4.3)$$

with the angular dependence:

$$\begin{aligned} f(\theta, \theta', \alpha) &= 3 \left( \cos^2 \theta + \cos^2 \theta' - 5 \cos^2 \theta \cos^2 \theta' - \frac{1}{3} \right) \\ &\quad - (1 - a_2) \cos^2 \alpha - 3(a_2 - 3) \cos \alpha \cos \theta \cos \theta'. \end{aligned} \quad (4.4)$$

Since the displacements of a force dipole scale  $\sim R^{-2}$ , the strain field scales  $\sim R^{-3}$  with distance, which leads to the long-ranged elastic interaction ( $W^{PP'} \sim R^{-3}$ ) typical for dipolar interactions. The complicated angular dependence in Eq. (4.4) results in a highly anisotropic interaction. Note that for the planar geometry, there are only two independent angles. Nevertheless we prefer to write the interaction symmetrically in the primed and unprimed coordinates, since this is favorable for numerical implementations because, instead of the computationally expensive cosine-functions, one only has to evaluate the respective scalar products, given above.

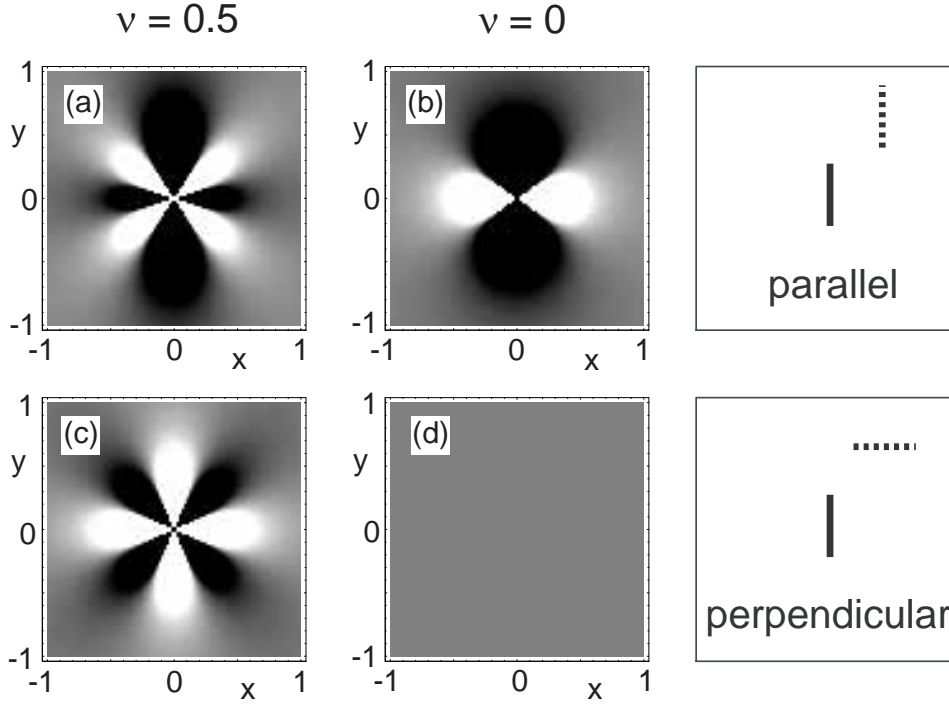


Figure 4.2: Density plots of cellular interactions on an elastic half space given by  $\Delta W^{PP'}$  from Eq. (4.3) for (a,b) parallel and (c,d) perpendicular orientations. In (a,c), Poisson ratio  $\nu = 1/2$ , and in (b,d),  $\nu = 0$ . One dipole oriented along the  $y$ -axis is fixed at the origin, while the other is moved in space, see right panels. Black denotes areas of attraction (strain-stiffening) and white areas of repulsion (strain softening). The interaction potential for defect dipoles simply differs in sign, thus black and white exchange meaning.

In Fig. 4.2 we show a density plot of the interaction between force dipoles for  $\nu = 0.5$  and  $\nu = 0$ . Black (white) denotes areas of strain stiffening (softening), which mediate an attractive (repulsive) interaction between cellular dipoles. In contrast, for physical dipoles black areas are repulsive and white areas are attractive. We see that the angular part of the interaction in 2D varies significantly with Poisson ratio as strain is propagated differently on compressible and incompressible media. For example as shown in Fig. 4.2(a,b), for parallel oriented dipoles a side-by-side (or railway-track) configuration is favorable for cellular dipoles on incompressible, but highly disfavored for dipoles on compressible substrates. Moreover, towards highly compressible media ( $\nu \rightarrow 0$ ), the transverse shear mode upon contraction along the  $y$ -axis (Poisson effect) is strongly suppressed, i.e.  $u_{xx} \rightarrow 0$ . Thus, for  $\nu = 0$  the interaction vanishes for two perpendicularly oriented dipoles as shown in Fig. 4.2(d), while the corresponding dipoles on incompressible substrates strongly interact (c). For

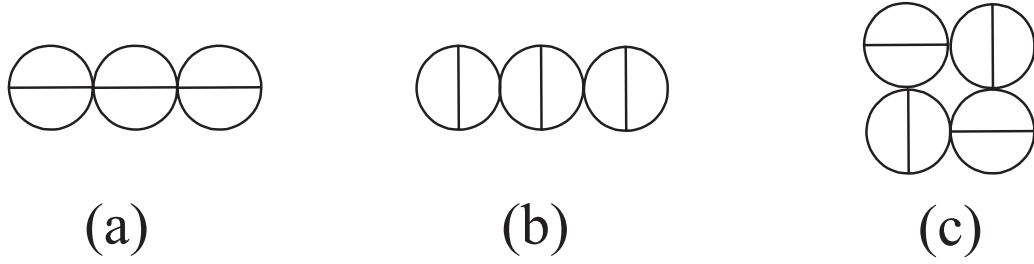


Figure 4.3: Different structures arising from elastic interactions of anisotropic force dipoles on top of an elastic half space. (a) Cellular force dipoles align in strings, similar to electric dipoles and independent of the value for  $\nu$ . (b) Physical force dipoles for Poisson ratio  $\nu \approx 0$  align side-by-side in a railway track like configuration. (c) Physical force dipoles for Poisson ratio  $\nu \approx 1/2$  locally form a T-configuration. The resulting structure is compact and similar to the one favored by electric quadrupoles. The crossover between (b) and (c) occurs at  $\nu = 1/5$ .

incompressible substrates ( $\nu = 0.5$ ), the Poisson effect results in large compressive strain fields along the  $x$ -axis, i.e.  $u_{xx} < 0$ , leading to a strongly repulsive interaction between perpendicularly oriented dipoles. Interestingly, there also exists an attractive region, which is centered around the  $xy$ -direction.

Despite these differences in  $\Delta W^{PP'}$  with  $\nu$ , we find that the *optimal* configuration for cellular dipoles is *independent* of the Poisson ratio. By minimizing  $\Delta W^{PP'}$  we can identify the preferred cell configuration. We find that  $\Delta W^{PP'}$  has a pronounced minimum for aligned dipoles ( $\theta = \theta' = \alpha = 0$ ), independent of  $\nu$ . The contraction of a dipole always causes maximal tensile strain (and thus maximal strain stiffening) along the axis of contraction  $u_{yy} < 0$ , see Fig. 4.2(a,b). Thus, the optimal state for cells are two aligned dipoles, see Fig. 4.3(a). At low cell densities, a common pattern for the organization of elastically interacting cells will therefore be the formation of strings of cells, similar to the case of electric dipoles [105, 106]. Strings might close into rings such that each cell is fully activated by its neighbors.

The case of defects with anisotropic dipole moments is described by the negative of Eq. (4.3). Then the ground state configuration strongly depends on the Poisson ratio  $\nu$  via the angular dependence of Eq. (4.4). For highly compressible media,  $\nu \rightarrow 0$  ( $\Lambda \rightarrow 0$ ), dipoles prefer to align side-by-side in a railway track configuration, see Fig. 4.3(b). For incompressible media,  $\nu = 1/2$  ( $\Lambda \rightarrow \infty$ ), dipoles arrange with perpendicular orientations in a local T-configuration, see Fig. 4.3(c). This leads to rather compact structure formation, with a square lattice pattern at intermediate densities and a hexagonal herringbone pattern at high dipole densities (not shown), similar to the situa-

tion with electric quadrupoles [48]. For  $\nu = 1/5$  ( $\Lambda = 2/3$ ), the T-configuration and the side-by-side configuration have degenerate energies.

Finally, for isotropic physical dipoles the 2D case has been discussed before [46]. Then

$$V^t = -P\delta_{li}G_{ij,lk'}^{2D}(\vec{r}, \vec{r}')P'\delta_{kj} = -PP'G_{ij,ij'}^{2D}(\vec{r}, \vec{r}') = +PP'G_{ij,ij}^{2D} = a_1a_2\frac{PP'}{R^3}, \quad (4.5)$$

where we used the fact that  $G_{ij}^{2D}$  is translationally invariant. Thus, for identical isotropic defects the interaction is isotropic and repulsive, while for cells with isotropic force patterns the interaction would be isotropic and attractive.

### 4.1.2 Dipoles in Elastic Full Space

Strain propagation in an elastic three-dimensional (3D) infinite medium is described by the Thomson Green function [56], which was introduced in Eq. 3.3. Due to the structural similarity between the Thomson Green tensor  $G_{ij}^\infty$  and the Boussinesq tensor  $G_{ij}^{2D}$ , the interaction law in 3D is very similar to the 2D case. We find for the effective interaction potential:

$$\Delta W^{PP'} = a_1^\infty \frac{PP'}{R^3} f^\infty(\theta, \theta', \alpha) \quad (4.6)$$

with the angular function  $f^\infty(\theta, \theta', \alpha)$  given by Eq. (4.4) by replacing the constants  $a_1$  and  $a_2$  with  $a_1^\infty$  and  $a_2^\infty$ , respectively, given in Eq. 3.4. Note that in 3D there are three independent orientational degrees of freedom.

In Fig. 4.4 we show the corresponding density plot of  $\Delta W^{PP'}$  for dipoles with relative orientations  $\alpha = 0$  and  $\alpha = \pi/2$  positioned in the  $x$ - $z$ -plane for two different values of the Poisson ratio,  $\nu = 0$  and  $\nu = 1/2$ . In contrast to 2D, the interaction of perpendicularly oriented dipoles diminishes with  $\nu \rightarrow 0$ , but does not vanish in 3D. For parallel dipoles, the interaction profiles look very similar for 2D and 3D.

We may now explicitly give the formulas for  $\Delta W$  for two identical dipoles interacting in the three basic configurations depicted in Fig. 4.3.

(a) For two parallel dipoles in  $z$ -direction placed along the  $z$ -axis, we find

$$\Delta W^{PP'} = -2a_1^\infty P^2 (a_2^\infty + 1) \left(\frac{1}{z}\right)^3 = -\frac{(1+\nu)P^2}{2\pi E z^3} = -\frac{(\Lambda+2)P^2}{2\pi c z^3}, \quad (4.7)$$

which yields the optimal configuration independent of the value for  $\Lambda$  or, equivalently,  $\nu$ . Thus, like on 2D substrates, cells in 3D favor to align along a common axis. Again this behaviour is similar to the one of electric dipoles [106].

(b) For two parallel dipoles in  $z$ -direction placed along the  $x$ -axis (side-by-side configuration), we find

$$\Delta W^{PP'} = a_1^\infty P^2 (a_2^\infty - 2) \left(\frac{1}{x}\right)^3 = \frac{(1+\nu)(1-4\nu)P^2}{8\pi E(1-\nu)x^3} = \frac{(\Lambda-1)P^2}{8\pi c x^3}. \quad (4.8)$$

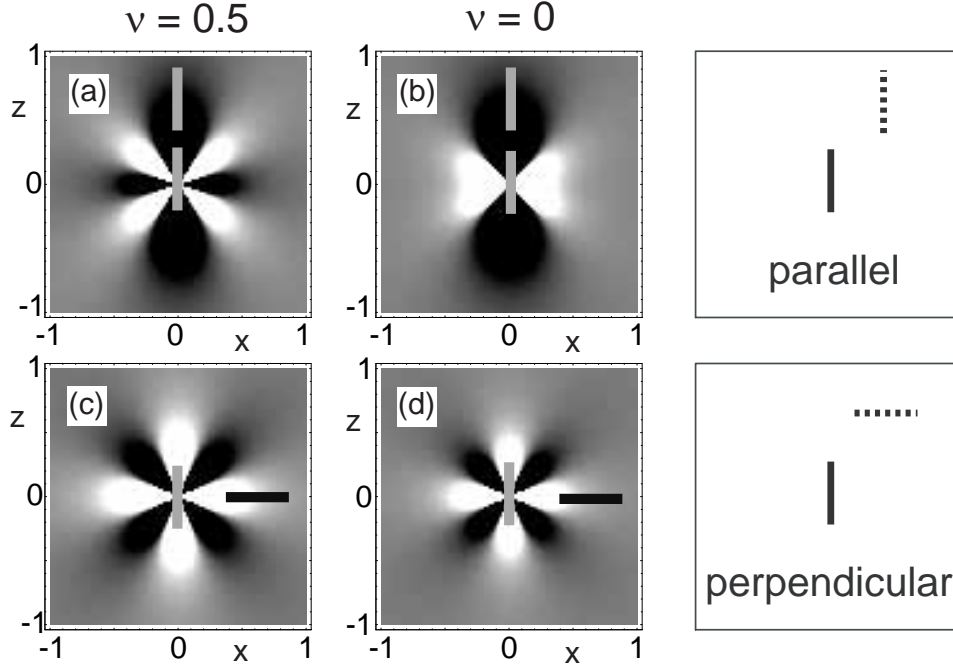


Figure 4.4: Density plots of cellular interactions in infinite space as specified by  $\Delta W^{PP'}$  from Eq. (4.6) for (a,b) parallel and (c,d) perpendicular orientations. In (a,c), Poisson ratio  $\nu = 1/2$ , and in (b,d),  $\nu = 0$ . One dipole oriented along the  $z$ -axis is fixed at the origin, while the other is moved in space. Black denotes areas of attraction (repulsion) and white areas of repulsion (attraction) for cellular (physical) dipoles. (a,b) Independent of the value for  $\nu$ , two cells prefer alignment (black region along  $z$ -axis). The interaction in the side-by-side configuration (along  $x$ -axis) changes sign at  $\nu = 1/4$ , when the black cone vanishes. (c,d) The T-configuration is the ground state for physical dipoles in 3D independent of the value for  $\nu$  (white regions along  $z$ - and  $x$ -axes).

Thus  $\Delta W^{PP'}$  changes sign as  $\Lambda$  varies through 1 or  $\nu = 1/4$ , respectively.

(c) Finally, in the T-configuration, where the first dipole is fixed in  $z$ -direction at the origin and the second dipole is positioned in the  $x$ - $y$ -plane oriented perpendicular to the  $z$ -axis, we find:

$$\Delta W^{PP'} = 2a_1^\infty P^2 \left(\frac{1}{r}\right)^3 = \frac{(1+\nu)P^2}{4\pi E(1-\nu)r^3} = \frac{(\Lambda+1)P^2}{4\pi cr^3}, \quad (4.9)$$

where  $r = \sqrt{x^2 + y^2}$ . In this case  $\Delta W^{PP'}$  is always positive and yields a globally maximal  $\Delta W^{PP'}$ . Therefore it corresponds to a globally minimal  $V^t = -\Delta W^{PP'}$  and the T-configuration is the ground state of two physical anisotropic contraction dipoles, independent of the value for  $\nu$ . The aggregation of physical dipoles in 3D is more complicated than in 2D, since the

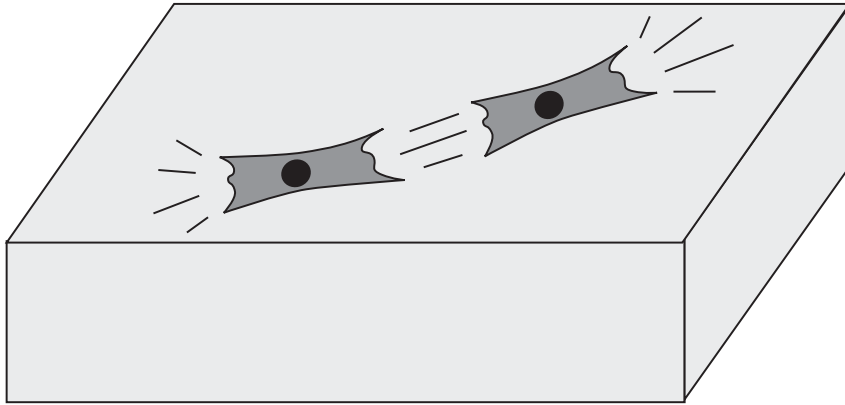


Figure 4.5: Elastic interaction of cells: cells interact elastically to form strings because in nose-to-tail alignment the mechanical activity of one cell triggers the one of the other cell, thereby forming a positive feedback loop for cell alignment.

T-configuration cannot be continued in 3D without causing frustration. This leads to the existence of many metastable states. Finally, we would like to mention that the elastic interaction of two isotropic dipoles in 3D vanishes, since  $G_{ij,ij}^\infty = 0$  [57].

### 4.1.3 Discussion: A Biomechanical Feedback Loop

We have applied the force dipole concept to cells to derive effective interaction potentials for cells on elastic substrates (2D) and in hydrogels (3D). We find that independent of the Poisson ratio and dimension, elastic interaction between cells favor alignment. This might be intuitively clear, since a contractile cell causes a local compression of the substrate underneath the cell along the contraction axis and tensile strain at more distant points. Hence at distant points maximal strain-stiffening occurs along the axis of contraction. A second cell will therefore upregulate its mechanical activity along the same direction. This scenario constitutes a positive mechanical feedback loop for cell alignment, since in the aligned configuration the mechanical activity of one cell upregulates the activity of the other and vice versa as depicted in Fig. 4.5. Thus, at low cell densities we expect cells to preferentially form strings and rings, similar to electric dipoles [106]. In fact in Ref. [107] the formation of short strings was recently observed for fibroblasts in a collagen gel.

We have also studied the interaction of physical force dipoles, which are related to the cellular case by switch of sign in the interaction potential, i.e.  $V = -W$ . In contrast to the cellular case, the ground state for physical dipoles depends on dimension and Poisson ratio. In Fig. 4.6 we summarize

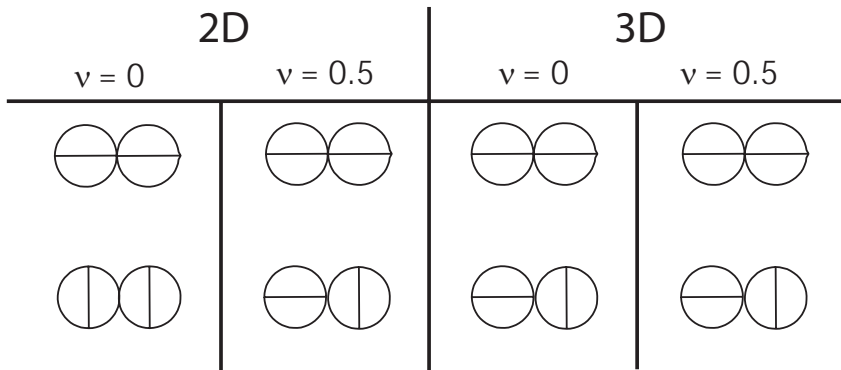


Figure 4.6: Optimal configuration for cellular dipoles (top) and physical dipoles (bottom) for interactions in 2D and 3D and as a function of Poisson ratio. Cells always prefer to align. In 3D physical dipoles always prefer the T-configuration, while in 2D at small Poisson ratio the ground state is the rail-way track configuration.

our results for the optimal states. From the structural similarity between 2D and 3D Green function, one may expect that strain propagation in 2D and 3D occurs rather similarly. Indeed at  $\nu = 0.5$  the Green functions in 2D and 3D are identical up to a constant prefactor. However, there are also some important differences. In general, we find that in 3D strain propagation is less effected by variations of the Poisson ratio and the optimal structures for both cellular and physical particles are conserved. For the elastic half space the situation is more interesting. In particular the transverse shear mode is strongly suppressed on highly compressible substrates, such that perpendicularly oriented dipoles do not interact. Therefore, the ground state for physical dipoles changes from the T- to the side-by-side configuration. Another important difference between 2D and 3D is that the elastic interaction of *isotropic* dipoles vanishes in 3D [57], but not in 2D [46]. Therefore, the interaction of isotropic dipoles in 3D is completely determined by boundary-induced interactions, like for hydrogen in metal samples of finite size [45].

## 4.2 Strings of Dipoles

At low dipole density the angular dependence of the (cellular) elastic dipole–dipole interaction favors the formation of strings of aligned dipoles both on elastic substrates and in hydrogels. Therefore, in this section we will focus on the collective behaviour of *strings* and derive analytic results for interactions with strings using methods of complex analysis.

### 4.2.1 Single String

To calculate the effective interaction potential  $\Delta W$  for  $N$  dipoles in a string, we can apply the superposition principle, since the medium is assumed to be linear. Thus,  $\Delta W$  is given by the sum over all pairwise interactions between dipoles:

$$\Delta W = \frac{1}{2} \sum_{\alpha=1}^N \sum_{\beta \neq \alpha}^N \Delta w_{\alpha\beta}, \quad (4.10)$$

where the factor  $\frac{1}{2}$  is required to avoid double counting. In a finite string composed of  $N$  identical dipoles with a uniform distance  $a$  between adjacent dipoles as shown in Fig. 4.7, there are  $N - 1$  interactions between dipoles separated by the distance  $a$ ,  $N - 2$  interactions between dipoles separated by  $2a$ , etc. Thus,  $\Delta W$  reads:

$$\Delta W = -2a_1(a_2 + 1) \frac{P^2}{a^3} \left( \frac{N-1}{1^3} + \frac{N-2}{2^3} + \dots + \frac{1}{(N-1)^3} \right), \quad (4.11)$$

where  $a_1$  and  $a_2$  are the coefficients of the respective Green function in 2D and 3D given by Eq.(4.2,3.4). We can split Eq.(4.11) into two sums  $\sim \frac{N}{i^3}$  and  $\sim \frac{-1}{i^2}$ . We then extend the string to an infinite length and finally subtract the finite remainder due to the finite length of the chain:

$$\Delta W = \frac{-2a_1(a_2 + 1)P^2}{a^3} \left( N \sum_{i=1}^{\infty} \frac{1}{i^3} - \sum_{i=1}^{\infty} \frac{1}{i^2} + \sum_{i=N-2}^{\infty} \frac{i-1}{i^3} \right) \quad (4.12)$$

The limits of the first two sums are well known and can be expressed in terms of the Riemann Zeta-function  $\zeta(z)$ . The last sum can be expressed in terms of the  $\Gamma$ -function  $\Gamma(z) = \int_0^{\infty} t^{z-1} e^{-t} dt$ . One finds:

$$\Delta W = \frac{-2a_1(a_2 + 1)P^2}{a^3} \left( N\zeta(3) - \zeta(2) + \Psi^{(1)}(N-2) + \frac{1}{2}\Psi^{(2)}(N-2) \right), \quad (4.13)$$

where  $\zeta(3) \approx 1.20206$  and  $\zeta(2) = \pi^2/6 \approx 1.6449$ , respectively and  $\Psi^{(n)}(z)$  is the  $(n+1)$ -th logarithmic derivative of the  $\Gamma$ -function.

The first two summands in Eq.(4.13) have a simple meaning: for an infinite string, the first term  $\Delta w = -2a_1(a_2 + 1)P^2/a^3\zeta(3)$  relates to the change in effective stiffness experienced by one dipole in an infinite string due to the presence of all the other dipoles. The second term  $\Delta w = -2a_1(a_2 + 1)P^2/a^3\zeta(2)$  relates to the loss in effective stiffness when an infinite string is broken into two strings and thus, yields the penalty of creating a "free" chain end. Very similar considerations also apply to the case of electric dipoles, which also show a strong tendency to align in dipolar strings [106, 108].

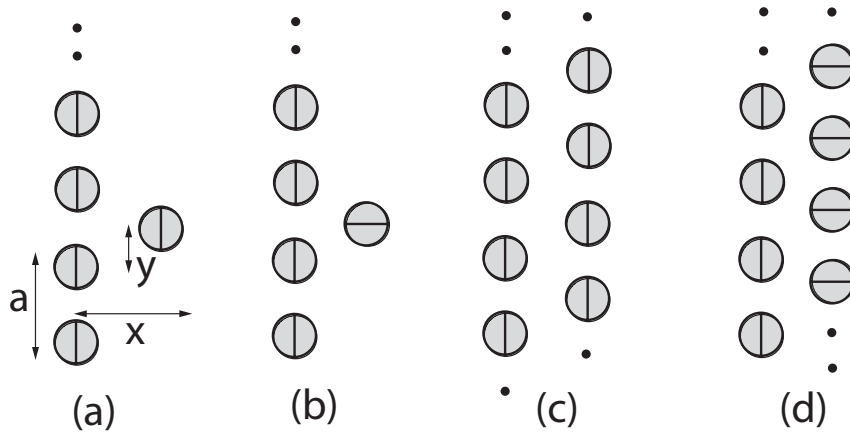


Figure 4.7: We study the elastic interactions of a single dipole and an infinite string composed of identical dipoles with dipolar spacing  $a$ . The position of the second dipole with respect to the string is determined by its horizontal distance  $x$  to the string origin and its vertical off-set  $y$ . We consider both parallel (a) and perpendicular (b) orientation of the dipole with respect to the string. Note that the elastic interaction *per dipole*  $\Delta w$  of two infinite strings or a string and a stack (c,d) of identical dipolar spacing is the same as the interaction of a single dipole oriented in parallel (perpendicularly) to an existing string (a,b).

### 4.2.2 Interactions with Strings

We now focus on the interaction of a single dipole with an infinite string of identical dipoles with their dipole moment aligned along the vertical axis of the string as shown in Fig. 4.7. We consider explicitly a parallel and perpendicular orientation of the second dipole with respect to the string (a,b). The distance of the dipole to the string is denoted by  $x$  and its off-set to the adjacent dipole by  $y$  while the separation between dipoles within the string is denoted by  $a$ . Using the same notation, we can also study the interaction between two infinite strings or an infinite string with an infinite stack as shown in Fig. 4.7(c,d). In fact, the interaction between two strings or string and stack of identical dipolar spacing yields the same results *per dipole* as for the respective case of a single dipole shown in Fig. 4.7(a,b).

#### Interactions of Two Strings

The change in  $\Delta w^{\parallel}$  encountered by a single cell oriented *in parallel* to an infinite string of cells at the position  $(x, y)$  away from the stack's origin is given by the sum of all pairwise interactions of the dipole with the string. We assume that all dipoles are oriented along the  $y$ -axis. Then, the pairwise interactions of the dipole with each dipole in the string can be expressed in

cartesian coordinates using the Green function representation of the interaction of two dipoles with parallel orientations, i.e. we write the interaction between two parallel dipoles in terms of  $w = P_{yy}u_{yy} = -P^2\partial_y^2G_{yy}$ . Hence:

$$\Delta w^{\parallel} = -a_1P^2\frac{\partial^2}{\partial y^2}\sum_{n=-\infty}^{+\infty}\left(\frac{a_2}{(x^2+(na-y)^2)^{\frac{1}{2}}}+\frac{(na-y)^2}{(x^2+(na-y)^2)^{\frac{3}{2}}}\right), \quad (4.14)$$

where  $a_1$  and  $a_2$  are the coefficients of the respective elastic Green function in 2D and 3D given in Eq.(4.2) and Eq.(3.4), respectively. Eq.(4.14) describes also the string-string interaction (per dipole) of two parallel infinite strings separated by a distance  $x$  with an mutual off-set  $y$ . The first term in Eq.(4.14) describes the corresponding interaction of electric dipoles, where  $a_1a_2 \rightarrow 1/(8\pi\epsilon_0)$  and  $P \rightarrow \mu$  is the electric dipole moment [108]. For the special case of highly compressible substrates with vanishing Poisson ratio  $\nu = 0$  in 2D, the second term vanishes for elastic dipoles. However, in all other cases, in particular for the 3D situation for any  $\nu$ , the second term is present and moreover *dominates* the asymptotic interaction far away from the string.

For electric dipoles, Phil Allen very recently revisited the interaction of parallel strings using methods of complex analysis [108,109], and we will apply a similar approach for the case of elastic dipoles. In order to evaluate the sums in Eq. (4.14), we can make use of the Poisson sum rule [108]:

$$g(x,y) = \sum_{n=-\infty}^{\infty} f(in) = \frac{1}{2i} \oint_C f(z) \coth \pi z, \quad (4.15)$$

where the contour  $C$  surrounds the imaginary axis in the complex plane. The Poisson sum rule is a special case of the residue theorem: the  $\coth \pi z$  has simple poles at  $z = in$  and the residue can be evaluated with the help of the rule of l'Hospital:

$$\lim_{z \rightarrow in} (z - in)f(z) \frac{\cosh \pi z}{\sinh \pi z} = \frac{f(in)}{\pi}. \quad (4.16)$$

Hence, if  $f(z)$  has no singularities inside  $C$  the residue theorem yields Eq.(4.15). For the sums of Eq.(4.14) it is convenient to scale all distances with respect to  $a$  and to evaluate them separately with the help of the Poisson sum formula, i.e.:

$$f_1(z) = \frac{a_2}{\sqrt{(x/a)^2 - (z - iy/a)^2}} \quad (4.17)$$

$$f_2(z) = -\frac{(z - iy/a)^2}{((x/a)^2 - (z - iy/a)^2)^{\frac{3}{2}}}. \quad (4.18)$$

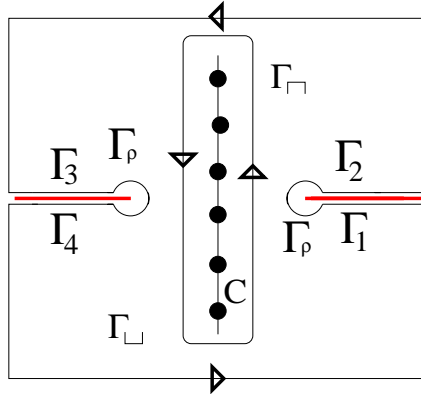


Figure 4.8: We evaluate the sum in  $\Delta w^{\parallel}$  with help of the Poisson sum rule and turn the sum into an integral in the complex plane. The path  $C$  surrounds the simple poles of the  $\coth \pi z$ . To calculate the integral we replace  $C$  by the keyhole-contour  $\Gamma$ . Since the integrands in  $g_1$  and  $g_2$  have to branch-points at  $u_0 \pm x$ , we introduce two branch-cuts. The keyholes surround the two branch-cuts.

Substituting  $u = z - iy/a$ , the sums are given by the integrals:

$$g_1(x, y) = \frac{a_2}{2i} \oint_C du \frac{\coth \pi(u + iy/a)}{\sqrt{(x/a)^2 - u^2}} \quad (4.19)$$

$$g_2(x, y) = -\frac{1}{2i} \oint_C \frac{u^2 \coth \pi(u + iy/a)}{((x/a)^2 - u^2)^{\frac{3}{2}}}. \quad (4.20)$$

Since both integrands have branch-points at  $u_0 = \pm x$ , we bend the contour  $C$  of the  $g$ -integrals around the branch-cuts shown in Fig. 4.8 and integrate along the new “keyhole-path”  $\Gamma$ .

We now apply basic symmetry arguments to simplify the above integrals. Let us first split the  $\coth$ -term in  $g_1$  and  $g_2$  in its real and imaginary part:

$$\coth \pi(u + iy) = \frac{\sinh 2\pi u}{\cosh 2\pi u - \cos 2\pi y} + i \frac{\cosh 2\pi u}{\cosh 2\pi u - \cos 2\pi y}. \quad (4.21)$$

For the imaginary part of Eq.(4.21), both integrands in Eq.(4.19,4.20) behave symmetric under the inversion transformation  $u \rightarrow -u$  and hence their contributions cancel piecewise along  $\Gamma$ . In contrast, for the real part both integrands behave asymmetric and their contributions add up, i.e. for both integrals in Eq.(4.19,4.20) we are left with the integration over the real part of the  $\coth$ -term. For integration along the square contour we can furthermore use a reflection symmetry with respect to the imaginary axis: let  $u = p + iq$  and consider a reflection at the imaginary axis, i.e.  $p \rightarrow -p, q \rightarrow q$ , then

$Re(g_i) \rightarrow -Re(g_i)$  while  $Im(g_i) \rightarrow -Im(g_i^*) = Im(g_i)$ . Hence, the contributions of the integrals along the square contour cancel piecewise. In conclusion, we are left with an integration over the real part of the coth-term along one keyhole contour formed by  $\Gamma_1 - \Gamma_\rho - \Gamma_2$ . Since  $\sqrt{(x/a)^2 - u^2}$  changes sign across the branch-cut, the integrals along  $\Gamma_{1,2}$  add up and we finally find for the dimensionless interaction of a parallel dipole (and string of parallel dipoles respectively) with an infinite stack:

$$\begin{aligned} \frac{\Delta w^\parallel}{P^2/a^3} &= \frac{\partial^2}{\partial(y/a)^2} \int_{x/a}^{\infty} du \frac{-2a_1 a_2 \sinh 2\pi u}{\sqrt{u^2 - (x/a)^2} (\cosh 2\pi u - \cos 2\pi y/a)} \\ &- \frac{\partial^2}{\partial(y/a)^2} \left( 2 \int_{\frac{x}{a} + \rho}^{\infty} du + \int_{\Gamma_\rho} du \right) \frac{a_1 u^2 \sinh 2\pi u}{\left(u^2 - \left(\frac{x}{a}\right)^2\right)^{\frac{3}{2}} (\cosh 2\pi u - \cos 2\pi y/a)}. \end{aligned} \quad (4.22)$$

We note that for the first summand in Eq. (4.22) the integral along the circular  $\Gamma_\rho$ -contour vanishes in the limit  $\rho \rightarrow 0$ , while it diverges for the second summand. However, here it exactly cancels the divergence picked up for small  $\rho$  in the integrals along  $\Gamma_{1,2}$ .

From the exact representation of  $\Delta w^\parallel$  in Eq. (4.22), we can extract the asymptotic behavior for large distances  $x$ . We first differentiate the integrands with respect to  $y$ , then expand the integrands for leading terms in  $\exp(2\pi n x)$  and  $(x/a)^{-m+\frac{1}{2}}$  and finally solve the asymptotic integrals analytically. We find:

$$\Delta w^\parallel \approx \frac{8a_1 \pi^2 P^2}{a^3} \cos\left(\frac{2\pi y}{a}\right) e^{-\frac{2\pi x}{a}} \left( -2\pi \sqrt{\frac{x}{a}} + (a_2 + 1) \left(\frac{x}{a}\right)^{-\frac{1}{2}} + O\left(\frac{x}{a}\right)^{-\frac{3}{2}} \right) \quad (4.23)$$

The leading term in the interaction is therefore  $\Delta w^\parallel \sim \sqrt{x} e^{-2\pi x}$  unless  $\nu = 0$  in 2D where  $\Delta w^\parallel \sim e^{-2\pi x}/\sqrt{x}$  as for electric dipoles [108]. The asymptotic interaction of parallel elastic strings with zero-offset  $y = 0$  is therefore always attractive both in 2D and 3D with one exception, namely for  $\nu = 0$  in 2D, when the asymptotic interaction is repulsive. In Fig. 4.9(b,d) we compare the asymptotic expansion of  $|\Delta w|$  given by Eq. (4.23) with the corresponding results of the direct numerical evaluation of the sum given in Eq. (4.14) using a logarithmic plot. We show results for different values of the Poisson ratio  $\nu$  and for 2D and 3D situations. Depending on  $\nu$ , the asymptotic and exact solution agree already at  $x/a = 1$  within  $\pm 2 - 10\%$ , while at  $x/a = 2$  the agreement is better than 1%. Therefore, the interaction between strings of dipoles is effectively *short-ranged* and falls-off exponentially with a length scale  $\lambda = a/2\pi$  set by the dipolar spacing  $a$  within the string. The transverse interaction with the string is hence only determined by the geometry of the string and independent of any special material properties of the elastic medium.

For distances comparable to and smaller than  $a$  the asymptotic expansion breaks down and in Fig. 4.9(a,c) we plot  $\Delta w^\parallel$  for  $x \leq a$  and  $y = 0$  for 2D

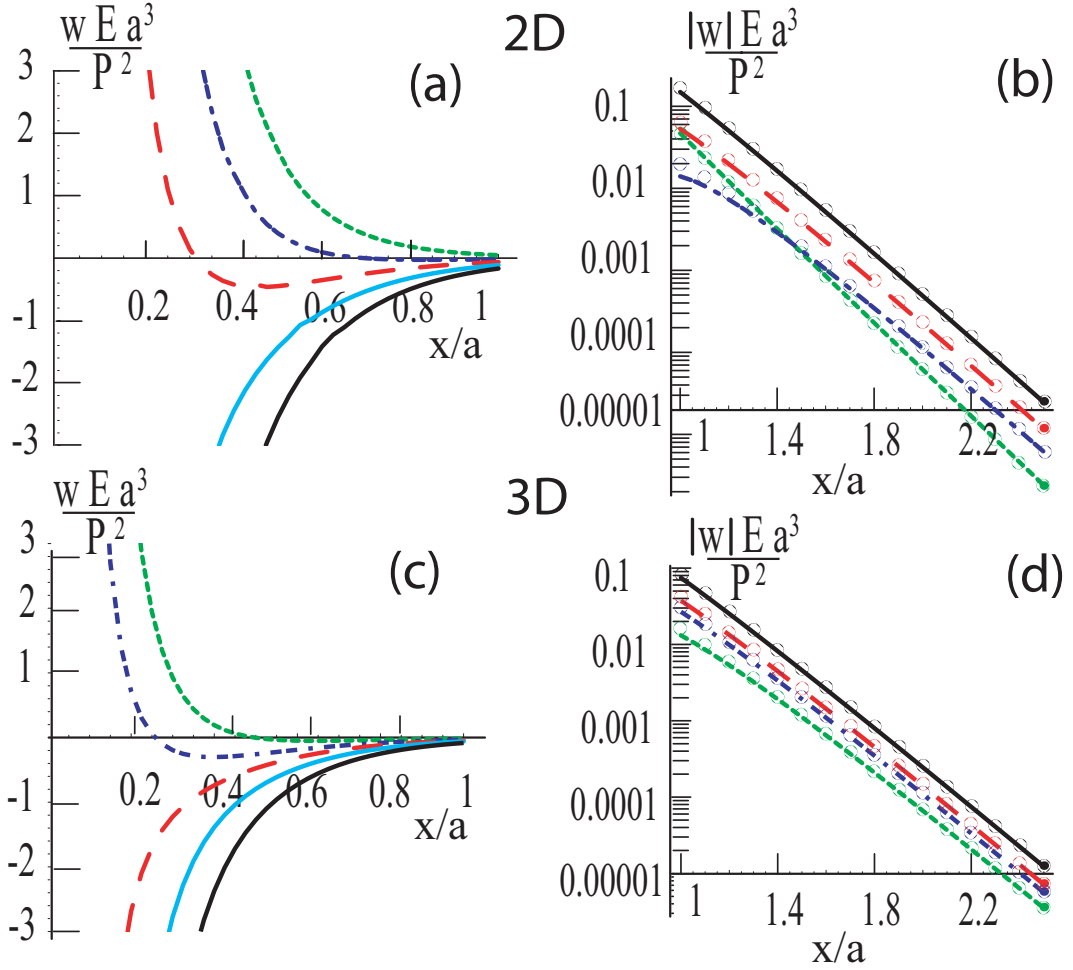


Figure 4.9: Elastic interaction between parallel strings with zero vertical offset  $y = 0$  as a function of separation between strings  $x/a$ , measured in units of the dipolar spacing  $a$ . Results shown for 2D (a,b) and 3D (c,d), respectively. The left row (a,c) shows a linear plot of  $w^{\parallel}$  close to the string for  $\nu = 0, 0.2, 0.3, 0.4, 0.5$  from top to down evaluated numerically from Eq. (4.14). For small  $x \ll a$ , the interaction is dominated by the dipole-dipole interaction of laterally adjacent dipoles. (b,d) The interaction between strings is effectively short-ranged and falls off exponentially with  $\lambda = \frac{a}{2\pi}$  for  $x \geq a$ . Right row shows the corresponding results to (a,c) for  $|\Delta w^{\parallel}|$  for  $x \geq a$  using a logarithmic plot. Lines show the first two terms of the asymptotic expansion in Eq. (4.23) and dots the exact numerical evaluation of Eq. (4.14).  $\nu = 0.4$  was omitted for better visibility.

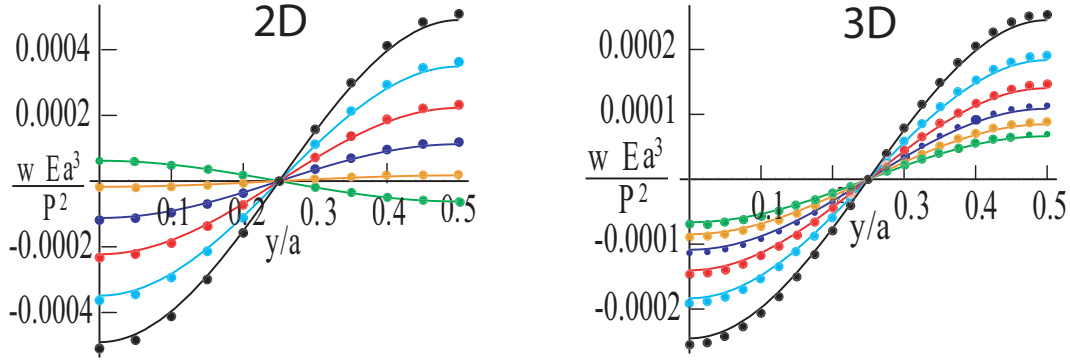


Figure 4.10: The string-string interaction  $\Delta w^{\parallel}$  oscillates as a function the vertical off-set  $y$ . Strings are separated horizontally by  $x/a = 2$ . Lines show the asymptotic result Eq. (4.23) for 2D (left) and 3D (right) for  $\nu = 0, 0.1, 0.2, 0.3, 0.4, 0.5$  from top to bottom and dots the exact numerical results Eq. (4.14). Note that  $\Delta w^{\parallel}$  is phase-shifted for  $\nu = 0$  in 2D.

and 3D, respectively. In this regime the distance law gradually crosses over from the exponential to the dipolar  $r^{-3}$ -powerlaw and the interaction depends strongly on the material properties. Figs. 4.9(a,c) reveal an interesting dependence of the interaction on the Poisson ratio. While for large  $x$  the interaction of  $y = 0$ -strings is always attractive (except for  $\nu = 0$  in 2D), the interaction changes sign and becomes repulsive for small  $x$  in compressible media. For distances  $x$  closer than the dipolar spacing  $a$  within the string,  $\Delta w^{\parallel}$  gets increasingly dominated by the interaction of adjacent dipoles in neighboring strings. For example, for strings with zero off-set, dipoles are arranged in the local side-by-side configuration. Recall that for two dipoles in the side-by-side configuration the interaction changes with the Poisson ratio and is attractive for incompressible, but repulsive for highly compressible media, see Fig. 4.2(a,b) and Fig. 4.4(a,b), respectively. This explains why closely spaced strings with zero-offset are favored for incompressible media, but are disfavored for highly compressible media. The situation is reversed for strings with maximal off-set  $y = 0.5$  which attract (repel) each other in (in)compressible media, again consistent with the respective behavior of the two body interaction of adjacent dipoles shown in Fig. 4.2(a,b) and Fig. 4.4(a,b).

Due to translational invariance by  $(0, a)$  along the axis of an infinite string, the interaction  $\Delta w^{\parallel}$  of a dipole with a string must be a periodic function of  $y/a$ , i.e.  $\Delta w^{\parallel} \sim \text{Re}[\sum_m a_m \exp(2\pi i m y/a)]$ . Our calculations show that the interaction is strictly oscillatory with the offset  $y$  and the period  $a$  with zero constant offset, i.e.  $a_0 = 0$ , and is asymptotically approximated by a simple cosine for large vertical distances  $x$  between strings. The oscillations in  $\Delta w^{\parallel}$

with the off-set  $y$  are plotted in Fig. 4.10 for  $x/a = 2$ , where the dots represent the exact (numerical) results and the lines the asymptotic formula. Note, the  $\pi$ -phase-shift for  $\nu = 0$  in 2D. A phase shift also occurs for small  $x < a$  in 2D and 3D at small  $\nu$  (data not shown) when the asymptotic approximation breaks down and the interaction becomes strongly dependent on the material properties as discussed above.

### Interactions of Strings and Stacks

We now consider the interaction of a dipole oriented *perpendicularly* with respect to an infinite string of aligned dipoles as shown in Fig. 4.7(b,d).  $\Delta w^\perp$  is again given by the sum of all pairwise interactions between perpendicularly oriented dipoles, which in cartesian coordinates is given by  $w = P_{xx}u_{xx} = -P_{xx}\partial_x\partial_y G_{xy}P_{yy}$ , i.e.

$$\Delta w^\perp(x, y) = -a_1 P^2 \frac{\partial^2}{\partial x \partial y} \sum_{n=-\infty}^{\infty} \frac{x(na - y)}{(x^2 + (na - y)^2)^{\frac{3}{2}}}. \quad (4.24)$$

For the given string geometry, where the distance between dipoles is given by  $r_n = \sqrt{x^2 + (y - na)^2}$ , one can show that Eq. (4.24) yields the same result as:

$$\begin{aligned} \Delta w^\perp(x, y) &= a_1 P^2 \frac{\partial^2}{\partial x^2} \sum_{n=-\infty}^{\infty} \frac{x^2}{(x^2 + (na - y)^2)^{\frac{3}{2}}} \\ &= a_1 P^2 \left( 2 + 4x \frac{\partial}{\partial x} + x^2 \frac{\partial^2}{\partial x^2} \right) \sum_{n=-\infty}^{\infty} \frac{1}{(x^2 + (n - y/a)^2)^{\frac{3}{2}}}, \end{aligned} \quad (4.25)$$

which is more convenient to evaluate analytically. In order to extract the asymptotic behavior of  $\Delta w^\perp$  for large  $x$ , we determine the asymptotics of the sum in Eq. (4.26) using the methods of the previous subsection. We find for the leading terms:

$$\sum_{n=-\infty}^{\infty} \frac{1}{\left(\left(\frac{x}{a}\right)^2 + \left(n - \frac{y}{a}\right)^2\right)^{\frac{3}{2}}} \approx \frac{2a^2}{x^2} + 4\pi \cos(2\pi y/a) \frac{e^{2\pi x/a}}{(x/a)^{\frac{3}{2}}} \quad (4.26)$$

and hence

$$\Delta w^\perp \approx \frac{8a_1 \pi^2 P^2}{a^3} \cos\left(\frac{2\pi y}{a}\right) e^{-\frac{2\pi x}{a}} \left( 2\pi \sqrt{\frac{x}{a}} + O\left(\left(\frac{x}{a}\right)^{-\frac{1}{2}}\right) \right). \quad (4.27)$$

The asymptotic behavior for large  $x$  is set by  $\sqrt{x/a} e^{-\frac{2\pi x}{a}}$ , independent of  $\nu$ . In Fig. 4.11 the exact numerical results (dots) obtained from Eq.(4.24) are compared with the asymptotic results (line) from Eq. (4.27) for interactions of a string and a stack with zero off-set  $y = 0$ . We find very nice agreement already for  $x \approx a$ . As for parallel dipoles, the interaction with the string is effectively

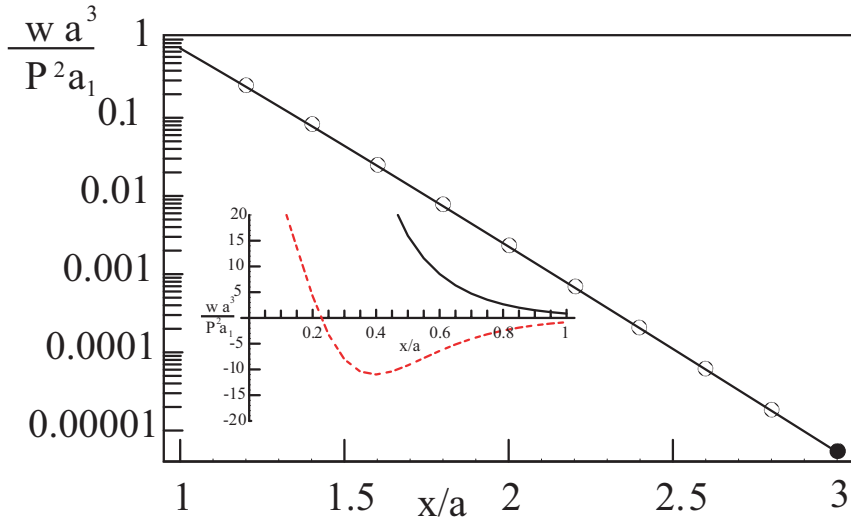


Figure 4.11:  $\Delta w^\perp$  for a dipole oriented perpendicularly to an infinite string with zero vertical off-set as a function of the horizontal distance  $x$  measured in units of  $a$ . Dots show the exact, numerical results and the line the asymptotic analytic results evaluated according to Eq. (4.24) and Eq. (4.27), respectively. The inset shows  $\Delta w^\perp$  for  $y/a = 0$  (line) and  $y/a = 0.5$  (dashed) for  $x/a < 1$ .

screened in the transverse direction and decays exponentially with the same length scale set by  $\lambda = a/2\pi$ .  $\Delta w^\perp$  asymptotically also shows the same oscillatory behavior as for parallel strings, but with a  $\pi$ -phase-shift. We find that the interaction of strings with stacks with zero vertical off-set ("T-strings") is asymptotically repulsive, whereas the interaction is asymptotically attractive for strings and stacks with maximal off-set  $y = 0.5a$ . In fact, Eq.(4.27) and Eq.(4.23) are identical up to the  $a_2(\frac{x}{a})^{-\frac{1}{2}}$ -term (and the sign).

For  $x < a$  the asymptotic expansion breaks down and in the inset of Fig. 4.11 we show exact numerical results obtained from Eq. (4.24) for T-strings ( $y = 0$ ) and strings and stacks with maximal off-set  $y = 0.5a$ , respectively. The formation of T-strings is always disfavored, which might be expected considering the repulsive interaction of locally adjacent dipoles in the T-configuration, which was the ground state for physical dipoles, and thus a highly disfavored local configuration for cellular dipoles (see Fig. 4.2, Fig. 4.4). However, strings and stacks with an offset of  $y/a = 0.5$  attract each other for  $x/a > 0.4$  (see inset in Fig. 4.11). This might be understood taking into account that there exist attractive cones in the dipole-dipole interaction of perpendicular dipoles favoring an offset between perpendicularly oriented dipoles (Fig. 4.4, Fig. 4.2). For  $x \rightarrow 0$ , the string and the stack merge to yield a single string with dipoles spaced by  $0.5a$  and alternating orientations. In this case, adjacent dipoles are again arranged in a local T-configuration, which explains why the interaction

changes sign and becomes repulsive for small  $x$ .

In contrast to the interaction of parallel dipoles, the qualitative behavior of  $w^\perp$  does not change as  $\nu$  is varied. However, the interaction varies quantitatively via the  $a_1$ -scaling and in general increases with increasing  $\nu$ . As discussed earlier, a special situation occurs for perpendicularly oriented dipoles on top of an elastic substrate (2D), where the coupling of shear and compression mode is strongly suppressed towards small  $\nu$ , i.e.  $a_1 \rightarrow 0$ . As a result, there is no interaction of the string with perpendicularly oriented dipoles (see Fig. 4.2(d)), but only with dipoles oriented in parallel to the string (via the  $a_2$ -term which survives).

### 4.2.3 Discussion

Although the interaction between isolated dipoles is in principle long-ranged and falls-off with the typical dipolar power-law  $\sim r^{-3}$ , the transverse interaction of a dipole oriented in parallel and perpendicular, respectively, with respect to an infinite string is effectively short-ranged. In the direction perpendicular to the string axis the strain fields of the string screen each other and elastic effects decay exponentially over the length-scale  $\lambda = a/2\pi$  set by the dipolar spacing within the string. This results in an effective short-ranged interaction of a single dipole with a string and between two parallel strings respectively. We also find that the interaction is oscillatory with the off-set along the direction of the string, which follows directly from the translational invariance along the string axis. Dipoles oriented perpendicular with respect to the string always prefer to have maximal off-set, while dipoles oriented in parallel asymptotically prefer to arrange with zero off-set (except for  $\nu = 0$  in 2D, where it is reversed).

Our calculations show that the typical length-scale  $\lambda$  is independent of the material properties, but depends only on the string geometry via the dipolar spacing  $a$  within the string. Although the exponential interaction law might be reminiscent of a Yukawa potential as obtained for the screening of a point charge by mobile carriers in electrostatics, the exponential decay in this case is a pure result of the geometry of the considered defect configuration. Electrostatic screening implies the attenuation of an external field due to a redistribution of mobile "charges" (defects) in the medium. Since screening is a result of microscopic processes inside the material, the strength of shielding depends on the material properties, in particular for electrostatic screening it reflects the polarizability of the medium [96]. In contrast, here we considered a *fixed* configuration of dipoles, which did not induce any rearrangement of elastic defects (nor did it induce any new ones). While the propagation of strain fields generated by a single dipole depends on the elastic length scales set by  $(P/E)^{\frac{1}{3}}$ , the new distance law is a result of a specific superposition of many

fields and only determined by the geometry of the given defect arrangement. To illustrate this point, let us decrease the distance  $a$  between dipoles within the string. Then the strain fields caused by dipoles along the string effectively *cancel* each other and the resulting overall strain tends rapidly to zero. From this perspective it might be hardly surprising to find that the interaction of two stacks of dipoles with *perpendicular* orientation with respect to the stack's axis, i.e.  $P_{ij} = P\delta_{ix}\delta_{jx}$  is long-ranged because now the strain fields  $u_{xx}$  along the dipole axis do not cancel, but rather *add* up. However, in the transverse direction, i.e. for  $u_{yy}, u_{zz}$ , the fields still interfere destructively.

The short-ranged interaction between strings seems to be a rather general result of the interaction of *dipolar* strings and is largely independent of the exact interaction mechanism. For example, by switching the sign of  $\Delta w$  we obtain the interaction potential of physical force dipoles, which therefore is also short ranged. Secondly, the electrostatic interaction of parallel strings of *electric* dipoles exhibits a very similar behavior to strings of elastic dipoles [108–110]. Thirdly, we expect a similar effect also for the interaction of strings of hydrodynamic force dipoles embedded in a fluid interacting hydrodynamically with each other because elastic and hydrodynamic Green function are structurally very similar [111].

Although the overall distance dependence of the interaction with a string of dipoles is independent of the material properties, but only dependent on geometry, the details of the interaction, in particular whether it is a repulsive or attractive interaction, certainly depend on the properties of the elastic medium. This is particularly true for small distances between strings with respect to the dipolar spacing within the string. Here the asymptotic expansion of  $\Delta w$  breaks down and the interaction gets increasingly dominated by the interaction between adjacent dipoles in the neighboring strings/stacks. In particular the Poisson ratio effects the way how strain is propagated in the medium. For example, for two strings the interaction may change sign close to the string when the substrate is highly compressible. Another important observation is that *on elastic substrates* the 2D-interaction of dipoles with perpendicular orientation decreases to zero with decreasing Poisson ratio because the transverse shear mode is strongly suppressed with vanishing  $\nu$ .

The fast decay of  $\Delta w$  with distance to the string  $x$  provides a strong hint why dipoles in our model prefer to form 1-dimensional strings at low dipole density. Along the string axis the interaction is strongly attractive while the interaction in the perpendicular direction is effectively short-ranged. Thus, a single cell hardly feels the presence of a string already at distances of the same order of magnitude than the dipolar spacing  $a$  within the string. In the next chapter we will show that much insight into basic structure formation of elastically interacting active cells can be gained from our knowledge about the interaction between dipolar strings.

# Chapter 5

## Structures on Elastic Substrates

For pattern formation in biology there typically exists an intimate relationship between structure and function, which is particularly true for biological tissues. Nature evolved many ways to guide cell organization in tissues: via chemotaxis or haptotaxis, via physical contact or via mechanics by either restructuring the overall composition of matrix (contact guidance) or via the elasticity of medium. Here we focus on structure formation of cells on elastic substrates due to elastic interactions. We aim to identify the relevant parameters governing pattern formation due to elastic effects, which may allow one to rationally engineer cellular force patterns and cell assemblies with defined properties in the future. We first study how force dipoles positioned on a regular lattice arrange their orientations in order to maximize effective stiffness. By using our results for dipolar strings from the previous chapter, we present a semi-analytical method to calculate the overall (effective) interaction potential for lattice structures for both physical and cellular dipoles. We identify *optimal* patterns as a function of lattice geometry and Poisson ratio  $\nu$ . We then use Monte Carlo simulations to investigate the influence of stochasticity and positional disorder on typical cellular structures formed on elastic substrates.

### 5.1 Structures on Micropatterned Substrates

The prediction of cellular patterns in an *in vivo* situation is rather complicated since several organizing principles could apply simultaneously and be of equal importance. Moreover, different organizing principles might yield similar structures, which obscures a direct comparison of theoretical predictions and experiment. *In vitro* experiments often allow for a better control of environmental stimuli and thus greatly simplify matters.

In order to study elastic interactions of cells, experiments using elastic substrates seem to be ideal because the effects of competing interactions are reduced and structures are easy to observe under a microscope. Moreover, a

combination of the elastic substrate method with new techniques like microcontact printing provide additional opportunities to design controlled experiments. Pioneered by Whitesides and Ingber, microcontact printing has been mainly used in the past to study the effect of cell geometry on cell organization by culturing cells on small adhesive islands on a non-adhesive substrate [112–114]. Recently microcontact printing was combined with elastic substrates to measure the dependence of traction force distribution on cell geometry [114]. In order to study structure formation of cellular force patterns, one could create regular lattices of adhesive islands on a non-adhesive elastic substrate and in this way gain control over cell positioning. This reduces the number of cellular degrees of freedoms and allows to selectively focus on cell orientation.

What kind of patterns would one expect to see if elastic interactions were the dominant driving mechanism for ordering? How can one control these patterns? We address these questions in the following by studying structure formation on elastic substrates for force dipoles positioned on a square and hexagonal lattice, respectively.

### 5.1.1 Optimal Lattice Structures

#### Basic Considerations: The String–Stack Decomposition

In order to characterize different structures, we apply the organization principle of stiffness preference by calculating:

$$w^{\text{tot}} = \frac{1}{2N} \sum_{i,j \neq i}^{N_x, N_y} \Delta w_{ij}, \quad (5.1)$$

where  $\Delta w_{ij}$  specifies the interaction between dipole  $i$  and  $j$  and  $w^{\text{tot}}$  is the elastic interaction normalized with respect to the total number of particles in the lattice  $N = N_x N_y$ . Eq.(5.1) can again be considered as an effective total interaction potential for elastically interacting cells. By flipping the sign of Eq.(5.1) one obtains the total potential energy (per dipole)  $v^t$  of a given defect assembly. In analogy to the defect case, the *optimal* state for cells (i.e. the analog to the ground state) is the structure which minimizes  $w^{\text{tot}}$ , i.e. the pattern in which dipoles are arranged in such a way that each cell senses the maximal effective stiffness in its environment due to the traction of all the other cells.

To calculate  $w^{\text{tot}}$  for an infinite lattice of dipoles, one first has to check the convergence properties of the sums in Eq.(5.1). The  $\Delta w_{ij} \sim \frac{1}{r^3}$  power-law provides a sufficiently fast decay that the sums in Eq.(5.1) converge *absolutely* for a 2D lattice. For interactions of dipoles on 3D lattices, the situation is more complicated and the sum converges at best *conditionally*, which means that in principle the result of Eq.(5.1) depends on the summing scheme.

## 5.1. STRUCTURES ON MICROPATTERNED SUBSTRATES 73

The absolute convergence of the sums in Eq.(5.1) for 2D lattices implies that one can choose any summing procedure because the result is independent on the ordering of summands. In the following we introduce a summing scheme, which decomposes the structure of interest into (sub)lattices of parallel strings. For example, for a lattice with lattice constant  $b$ , composed of identical dipoles all oriented along a common director  $\vec{n}$ , one could decompose the structure into parallel  $\vec{n}$ -strings and first sum the interactions within a string  $N_i \rightarrow \infty$  and then add all string-string interactions  $N_j \rightarrow \infty$ . Thus, using the results from Section (4.2),  $w^{\text{tot}}$  can be decomposed into:

$$w^{\text{tot}} = -2a_1\zeta(3)(a_2 + 1)\frac{P^2}{a^3} + \frac{1}{2}\sum_j \Delta w^{\parallel}(x_j, y_j). \quad (5.2)$$

$a$  is the dipolar spacing along the  $\vec{n}$ -string. The first term describes the interactions with dipoles along an infinite string, which was calculated in Eq.(4.13).  $\Delta w_j^{\parallel}$  is the interaction with the  $j$ -th parallel  $\vec{n}$ -string running at a horizontal distance  $x_j$  with a vertical offset  $y_j$ . Note that the string-string interaction scales with the dipolar spacing  $a$  within the string, which in general does not coincide with the lattice constant  $b$ , i.e.  $a = f(b)$ . As shown in Section 4.2, the interaction  $\Delta w^{\parallel}$  between strings is screened exponentially with horizontal distance between the strings. Thus, the sum over  $N_j \rightarrow \infty$  converges very quickly. Note, if  $x_j \leq a$ , i.e. if the distance between adjacent strings is smaller than the dipolar spacing  $a$ , the analytic approximation for  $\Delta w^{\parallel}$  derived in Eq.(4.23) does not hold and one has to evaluate Eq.(4.14) numerically instead.

For lattice structures with dipoles of different orientations ( $\vec{n}_A \neq \vec{n}_B$ ) it is often possible to formally decompose the structure into an  $A$ -sublattice of interacting  $\vec{n}_A$ -strings and a  $B$ -sublattice of interacting  $\vec{n}_B$ -strings. One could consider the interactions in each sublattice separately and finally add the interaction between the two sublattices. Suppose  $A$  and  $B$ -strings have perpendicular orientations, then the interaction between a string of  $A$ -dipoles and a parallel stack of  $B$ -dipoles is also short-ranged as shown in Section 4.2. Thus, the interactions of  $A$  and  $B$ -sublattice converge rapidly. Hence:

$$w^{\text{tot}} = \frac{1}{2}(w_A + w_B + w_{AB}^{\perp}), \quad (5.3)$$

where  $w_A$  and  $w_B$  are the respective effective potentials for the  $A$  and  $B$ -sublattice and  $w_{AB}^{\perp}$  is the contribution of the string-stack interaction between the  $A$  and  $B$  sublattice.

The decomposition of lattice structures into strings has recently been introduced by Phil Allen to compute the electrostatic energies of 3D string-like lattice structures of electric dipoles [108]. Here, we transfer this method to the case of elastic dipoles and extend it to a string-stack decomposition. This allows to calculate and compare the interaction potentials for a much larger

class of lattice structures. Since the exponential screening of string-string interactions seems to apply quite generally to *dipolar* interactions (e.g. electric, elastic, hydrodynamic dipoles), we expect that this method will be useful for a broad class of problems involving structure formation. While here we restrict ourselves to 2D lattice structures, the method might also apply for 3D lattice structures, where the sums in Eq.(5.1) are only conditionally convergent. In Ref. [108], Allen showed that the result for the electrostatic energies of various string-like 3D lattice structures composed of electric dipoles calculated using the string-decomposition agrees with the well known Clausius-Masotti result. Thus, the string-decomposition method could represent a simple alternative to Ewald sums [115–117] or fast multipole expansions [118, 119], which are conventionally used for similar problems in electrostatics [115, 116] or elasticity theory [117–119]. Finally, Eqs.(5.2,5.3) imply that string-like structures are dominated by the interactions along the string and the interaction between the next neighbor strings or stacks, respectively. Thus, one could try to understand basic structure formation on 2D lattices from the interactions between strings and stacks, respectively, as discussed in Section 4.2.

### Optimal Structures for Square and Hexagonal Lattices

We now consider a square lattice and a hexagonal lattice of identical dipoles on top of an elastic substrate. Using the string decomposition introduced above, we will calculate  $w^{\text{tot}}$  as a function of the material properties for several structures of interest.

In order to identify good candidates for the optimal structure, we first apply a Monte Carlo annealing technique. We initialized about  $N \approx 1000$  dipoles with random orientations on a lattice with periodic boundary conditions. Dipole orientations were then changed at random. According to the Metropolis scheme, a new configuration was always accepted when  $w_{\text{tot}}$  decreased and otherwise accepted with the Boltzmann weight  $p \propto \exp(-\Delta w_{\text{tot}}/k_B T)$ , where  $T$  represents an effective temperature. In order work at the same area density  $\rho$  of dipoles, the lattice constants  $b_s$  and  $b_h$  of square and hexagonal lattice, respectively are related by  $b_h = \sqrt{\frac{2}{\sqrt{3}}} b_s$ . It is convenient to introduce a reduced temperature  $T^* = \frac{T\pi E b^3}{P^2}$ . In order to minimize  $w^{\text{tot}}$  numerically, slowly decrease  $T^*$  from  $T^* = 5$  to  $T^* = 0.001$ , using about 30 consecutive annealing steps, where in each step the system was allowed to equilibrate.

Typical structures for the square and hexagonal lattice obtained by Monte Carlo annealing are shown schematically in Fig. 5.1. One could broadly classify them into string-like (a,b) and more ring-like (c) patterns. String-like structures, in which case all dipoles orient their mechanical activity along a common axis, exhibit a discrete two-fold rotational symmetry and show strong

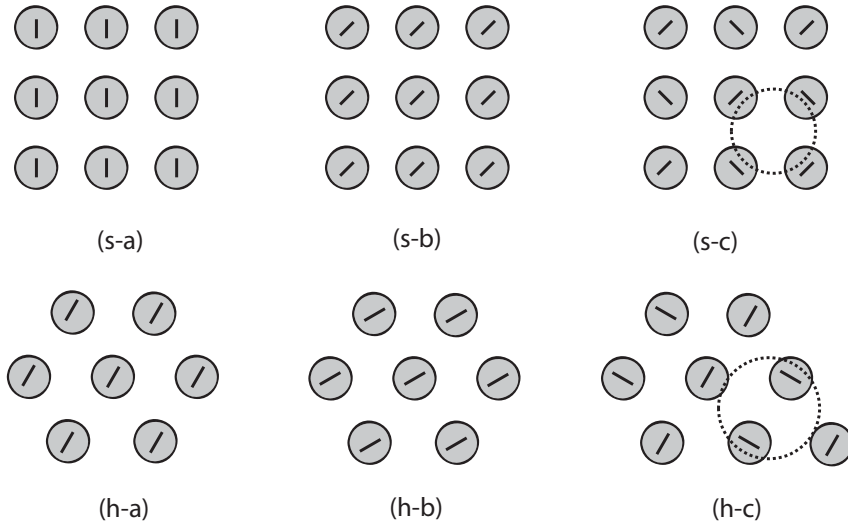


Figure 5.1: Different structures arising from elastic interactions of cellular force dipoles positioned on a square lattice (s-a)-(s-c) and on a hexagonal lattice (h-a)-(h-c) respectively on top of an elastic half space. The lattice constant is denoted by  $b$ . (a) and (b) are string-like structures with a two-fold rotational symmetry, which will result in anisotropic material properties of the composite active material of cells and the isotropic elastic substrate. (c)-structures are ring-like and have a four-fold rotational symmetry yielding more isotropic material properties.

anisotropic orientational ordering. This will result in anisotropic mechanical properties of the composite “active” material of elastic substrate and embedded cells, which makes string-like patterns particularly interesting. This effect will be less pronounced for structures with a higher order rotational symmetry like the ring-like structures, which yield more isotropic properties of the active material.

For the square lattice we found two string-like structures with a discrete two-fold rotational symmetry, namely (s-a) a lattice of identical  $s(0, 1)$ -strings and (s-b) a lattice of  $s(1, 1)$ -strings, respectively, where the  $(0, 1)$  and  $(1, 1)$  denote the direction  $\vec{n}$  of the strings. The third structure (s-c) is less anisotropic and exhibits a discrete four-fold rotational symmetry. Its unit cell is doubled with respect to the string-like structures and resembles a ring or a hedgehog, respectively. We will refer to this structure as the hedgehog- or ring-like structure, respectively, while (s-a) and (s-b) are pure string-like structures.

For the hexagonal lattice we found analogous patterns and will consider two string-like structures (h-a) a lattice of parallel  $h(1, 0)$ -strings and (h-b) a lattice of parallel  $h(1, 1)$ -strings and (h-c) one more ring-like structure. Note that the orientation of the string is always expressed with respect to the square

(*s*) and hexagonal (*h*) basis vectors, respectively.

All six structures (s-a) to (h-c) can be formally decomposed into (sub)lattices of parallel strings with the dipolar spacing  $a$  within the string being a function of the lattice spacing  $b$ . For the string-like structures in (a) and (b) the string decomposition is obvious. (s-c) can be formally decomposed into two string-like  $s(1,1)$  and  $s(-1,1)$  sublattices. The interaction between the two sublattices can be calculated from the interactions of  $s(1,1)$ -strings with  $s(1,1)$ -stacks. Similarly, (h-c) is decomposed into two sublattices of  $h(0,1)$  and  $h(-1,1)$ -strings, and the interaction between sublattices follows from  $h(1,0)$ -string-stack interactions.

Each structure is characterized by its dipolar spacing  $a$  within each string, the separation  $x_i$  between the zero-th and the  $i$ -th string or stack, respectively, and their offset  $y_i$ . In Tab.5.1.1 we summarize the characteristics of the different lattice structures under consideration, where  $\tilde{x}_i$  and  $\tilde{y}_i$  are normalized with respect to the dipolar spacing  $a$ .

Type	spacing $a$	$w^{\parallel}$		$w^{\perp}$	
	$a$	$\tilde{x}_i$	$\tilde{y}_i$	$\tilde{x}_i$	$\tilde{y}_i$
(s-a)	$b$	$i$	0	-	-
(s-b)	$\sqrt{2}b$	$i - \frac{1}{2}$ $i$	$\frac{1}{2}$ 0	-	-
(s-c)	$a_A = \sqrt{2}b$ $a_B = \sqrt{2}b$	$i$ $i$	0 0	$i - \frac{1}{2}$ $i - \frac{1}{2}$	$\frac{1}{2}$ $\frac{1}{2}$
(h-a)	$b$	$\sqrt{3}(i - \frac{1}{2})$ $\sqrt{3}i$	$\frac{1}{2}$ 0	-	-
(h-b)	$\sqrt{3}b$	$\frac{1}{\sqrt{3}}(i - \frac{1}{2})$ $\frac{i}{\sqrt{3}}$	$\frac{1}{2}$ 0	-	-
(h-c)	$b$ $\sqrt{3}b$	$i\sqrt{3}$ $\frac{i}{\sqrt{3}}$	0 0	$\sqrt{3}(i - \frac{1}{2})$ $\frac{1}{\sqrt{3}}(i - \frac{1}{2})$	$\frac{1}{2}$ $\frac{1}{2}$

From the string decomposition of the lattice structures given in Tab.5.1.1 one can now calculate  $w^{\text{tot}}$  semi-analytically applying the procedure outlined in Eq.(5.1) to Eq.(5.3). Since the vertical distance  $x$  of a string to the adjacent string or stack, respectively, is typically smaller than the dipolar spacing  $a$ , the string-string (string-stack) interactions are evaluated numerically using Eq.(4.27). We typically terminate the summation over string-string interactions after  $x \approx 5\text{-}10a$  interdipolar spacings.

In Fig.5.2 we plot our results for  $w^{\text{tot}}$  as a function of the Poisson ratio  $\nu$ . For all six structures the interaction between dipoles leads to an overall strain-stiffening effect, i.e.  $w^{\text{tot}} < 0$ . We also find that  $w^{\text{tot}}$  is a non-trivial function of  $\nu$  and that the optimal structure is a function of both geometry and Poisson ratio.

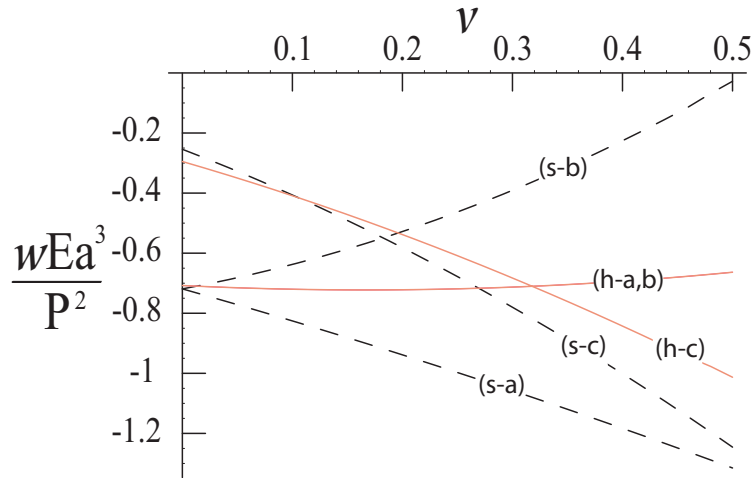


Figure 5.2:  $w^{\text{tot}}(\nu)$  calculated using the string-stack decomposition technique for the three square lattice structures (s-a) to (s-c) (dashed lines) and the three hexagonal lattice structures (h-a) to (h-c) (solid lines) shown in Fig. 5.1. The optimal structure depends on  $\nu$  and lattice geometry. String-like structures (a,b) are favored on highly compressible media, whereas toward larger  $\nu$  ring-like structures (c) are increasingly favored and dominate in the hexagonal lattice.

For the square lattice the string-like (s-a) structure of parallel  $s(1,0)$ -strings has always the minimal  $w^{\text{tot}}$  independent of  $\nu$ . For the special case of  $\nu = 0$  the (s-a) structures becomes degenerate to the  $s(1,1)$ -structure (s-b). In contrast, the optimal structure in a hexagonal lattice depends on the Poisson ratio of the substrate. For highly compressible media ( $\nu = 0$ ) the degenerate stringy structures (h-a) and (h-b) are optimal, while on incompressible substrates ( $\nu = 0.5$ ) the ring-like structure (h-c) becomes more favorable. The transition between these structures occurs at  $\nu \approx 0.32$ .

In fact, there is a general trend to destabilize string-like structures in favor of ring-like structures with increasing Poisson ratio in both the hexagonal and the square lattice. In the square lattice the gap in  $\Delta w^{\text{tot}} = w_{s-a}^{\text{tot}} - w_{s-c}^{\text{tot}}$  between the string-like optimal structure (s-a) and the hedgehog-structure (s-c) decreases strongly with increasing Poisson ratio, although the ring-like structure does not quite overcome the string-like structure as happens in the hexagonal lattice. This implies that on incompressible substrates the optimal structure changes qualitatively from a string-like to a ring-like structure as the geometry of the lattice is changed from the square to the hexagonal lattice. For highly compressible media string-like structures are always favorable and in particular towards  $\nu = 0$  they become (almost) equally favorable, as indicated by the (almost) degenerate values of  $w^{\text{tot}}$ . For highly compressible

materials the number of axis available for rotational symmetry breaking therefore increases. For example, for the square lattice on  $\nu = 0.5$ -substrates the system might either choose  $s(1, 0)$  or the  $s(0, 1)$ -axis, while for  $\nu = 0$  also the  $s(1, 1)$  and the  $s(1, -1)$ -directions are available. Indeed for the special case of  $\nu = 0$  there may be even more string-like structures with equally favorable  $w^{\text{tot}}$  and thus more possible symmetry axes, which we did not consider here explicitly.

### Interpretation of Results using The String–Stack Decomposition

The formation of string-like structures for cellular dipoles may have been expected, since the dipole–dipole interaction favors the formation of strings. In contrast, the formation of ring-like structures may come more as a surprise. We now show that a qualitative understanding of the results for  $w^{\text{tot}}$  as a function of lattice geometry and Poisson ratio can be gained from the string–stack decomposition and our knowledge about string–string and string–stack interactions, respectively from Chapter 4. Since the interaction between parallel strings and string and stacks, respectively, is short-ranged,  $w^{\text{tot}}$  is dominated by interactions within the strings and the next neighbor string–string and string–stack interactions, respectively. Hence,  $w^{\text{tot}}$  is affected most by variations in string geometry, i.e. dipolar spacing  $a$ , horizontal separation  $x$  and offset  $y$ .

For example, in the square lattice strings along  $s(1, 0)$  have the minimal interdipolar spacing possible ( $a = b$ ) and a favorable string–string interaction because adjacent strings have zero offset. This drives the (s-a) structure formation. In contrast, for  $s(1, 1)$ -strings  $a = \sqrt{2}b$ , and for  $\nu = 0.5$  the corresponding string–string interaction is repulsive because adjacent strings have maximal offset, which strongly disfavors (s-b) structure with respect to (s-a) on incompressible substrates. Finally, in the (s-c) structure the interaction between the  $s(1, 1)$ -strings and the adjacent  $s(1, 1)$ -stacks is strongly attractive because strings and stacks prefer to have maximal offset. This explains the competition between the hedgehog and the  $s(1, 0)$ -string structure on incompressible media because both structures have a favorable string–string (stack) interaction. The reason why (s-a) is slightly preferred with respect to (s-c), is probably the smaller dipolar spacing in (s-a).

For the hexagonal lattice, strings both in the (h-a) and (h-b)-structure have maximal offset and hence are disfavored at large  $\nu$ . In contrast, in the (h-c) structure, the interaction of adjacent strings and stacks is attractive at large  $\nu$  because they have maximal offset. Thus, in contrast to the square lattice, where parallel strings were stabilized due to the geometry of the lattice, they are destabilized in the hexagonal lattice with increasing  $\nu$ , while the interactions in (h-c) remain favorable. That could be the reason why the

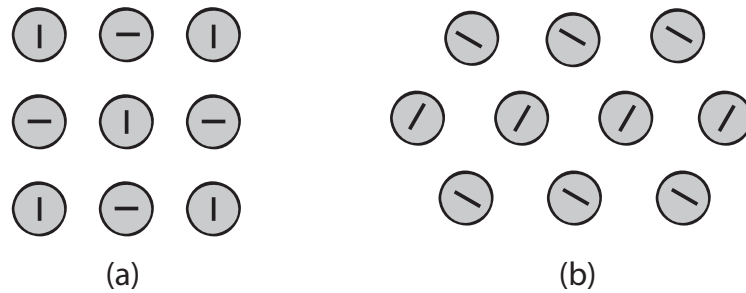


Figure 5.3: Physical force dipoles prefer to form a square T-lattice (a) or a hexagonal Herring bone-type pattern (b), respectively. Formally both structures can be decomposed into string-like sublattices, which simplifies the calculation of the elastic interaction energy  $v^{\text{tot}} = -w^{\text{tot}}$ .

ring-like structure is able to overcome the stringy structures in the hexagonal lattice, but not in the square lattice.

When the Poisson ratio is decreased, the overall interaction strength decreases and in particular the interaction between strings and stacks goes to zero. This explains why  $w^{\text{tot}}$  increases in ring-like structures with decreasing Poisson ratio. Moreover, for small Poisson ratio the string-string interaction exhibits a phase-shift with respect to the optimal offset for closely spaced strings, such that for small  $\nu$  the interaction of adjacent  $h(1,0)$ -strings is actually attractive. This explains why  $w^{\text{tot}}$  hardly varies with  $\nu$  in (h-a,b) because the decrease in the overall interaction strength is compensated by an increase in attractive interaction between strings.

To conclude, although the string-stack decomposition is primarily a convenient mathematical procedure to calculate  $w^{\text{tot}}$ , it is also a useful concept to gain more intuition for structure formation.

### Elastic Energy of Defect Lattices

The string-stack decomposition can also be used to calculate the elastic energy  $v^{\text{tot}}$  of lattices composed of physical dipoles. For physical dipoles the formation of aligned strings is a high energy state and thus avoided. Physical dipoles prefer to form compact (isotropic) aggregates: the local  $T$ -configuration, which is the ground-state of two physical dipoles on incompressible substrates can be continued in a square lattice without causing frustration and thus represents a good candidate structure for the ground state, see Fig. 5.3(a). By simulation an alternative competing structure was identified, which represents a hexagonal Herringbone-type pattern [48], see Fig. 5.3(b). The geometric characteristics of the string-stack decomposition of the T-lattice structure (a) and the Herringbone structure (b) are given in Tab. 5.1.1, where  $\tilde{x}$  and  $\tilde{y}$  have been

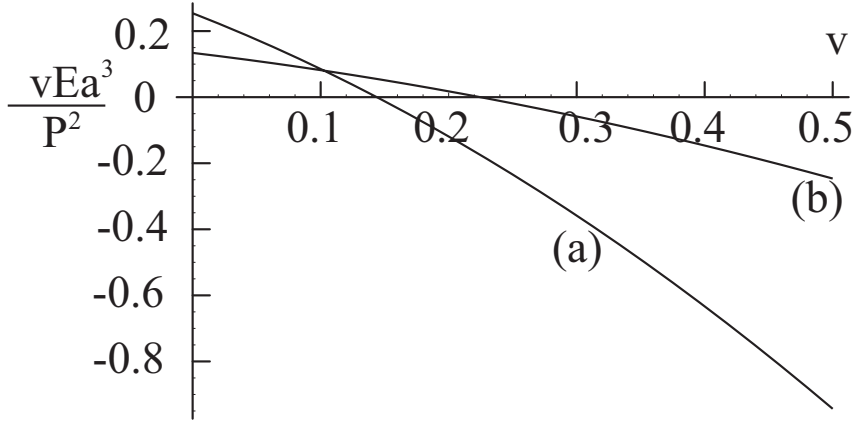


Figure 5.4: Elastic interaction energy per dipole  $v^{\text{tot}} = -w^{\text{tot}}$  for the T-lattice (a) and the Herringbone pattern (b) (at the same dipole density). The ground-state for an incompressible medium ( $\nu = 0.5$ ) is the T-lattice. For low Poisson ratio the Herringbone pattern takes over.

normalized with respect to the dipolar spacing  $a$ . By flipping the sign of Eq. 5.3 we can calculate the elastic interaction energy per dipole  $v^{\text{tot}}$  in these lattices, using the values from Tab. 5.1.1. Both in the T-lattice and in the Herringbone structure a stack is inserted into a string, i.e.  $\tilde{x} = 0$  and  $\tilde{y} = \frac{1}{2}$ . One can calculate the interaction energy of this arrangement analytically:

$$v^{\perp}(0, \frac{1}{2}) = -\frac{2a_1}{a^3} \sum_{i=1}^{\infty} \frac{1}{(i - \frac{1}{2})^3} = -\frac{14a_1}{a^3} \zeta(3). \quad (5.4)$$

Type	spacing $a$	$w^{\parallel}$		$w^{\perp}$	
		$\tilde{x}_i$	$\tilde{y}_i$	$\tilde{x}_i$	$\tilde{y}_i$
(a)	$a = 2b$	$i - \frac{1}{2}$	$\frac{1}{2}$	$i - \frac{1}{2}$	0
		$i$	0	$i$	$\frac{1}{2}$
(b)	$a = 2b$	$\sqrt{3}(i - \frac{3}{4})$	$\frac{1}{4}$	$\sqrt{3}(i - \frac{3}{4})$	$\frac{3}{4}$
		$\sqrt{3}(i - \frac{1}{2})$	$\frac{1}{2}$	$\sqrt{3}(i - \frac{1}{2})$	0
		$\sqrt{3}(i - \frac{1}{4})$	$\frac{3}{4}$	$\sqrt{3}(i - \frac{1}{4})$	$\frac{1}{4}$
		$\sqrt{3}i$	0	$\sqrt{3}(i - 1)$	$\frac{1}{2}$

By applying the procedure presented in Section 5.1 we calculate the elastic energy of both structures at equal density as a function of the Poisson ratio  $\nu$ . The result is shown in Fig. 5.3. We find that on incompressible substrates ( $\nu = 0.5$ ) the T-lattice has a significantly lower energy than the Herringbone pattern. When the Poisson ratio is decreased the Herringbone pattern takes over. This might be intuitively plausible since for  $\nu \rightarrow 0$  the ground state configuration of two physical dipoles changes from the T-configuration to the

the side-by-side configuration, which is closer to the local structures realized in the Herringbone pattern than in the T-lattice.

### 5.1.2 Effect of Noise: Monte Carlo Simulations

#### Monte Carlo Simulations

The determination of optimal structures is only a starting point for analyzing and predicting typical structures of elastically interacting cells. In a more realistic situation one should consider that—even without the presence of an additional ordering principle—ordering will not be perfect since there are always sources of external and internal noise. In order to include a stochastic element into structure formation we perform Monte Carlo simulations, where the temperature  $T$  represents an effective measure for the degree of stochasticity involved. In statistical physics, Monte Carlo simulations are a versatile tool to simulate the influence of thermal fluctuations. They are frequently used to numerically study the interplay between energy  $E$  and entropy  $S$  at finite temperatures  $T$  and to calculate phase-diagrams. At constant temperature a physical system in equilibrium minimizes the free energy  $F = E - TS$  and the system statistically visits each state  $\mu$  with the probability  $p_\mu = \frac{\exp(-\frac{E_\mu}{k_B T})}{Z}$ , where  $Z$  is the partition sum required for normalization. At low temperatures the energy is the dominant contribution to the free energy and the system spends most of its time in ordered states close to the ground state, while at high temperatures ( $k_B T \gg E$ ), entropy dominates, i.e. all states are equally probable and the system is in a disordered state. In analogy, for the cellular structure forming system  $w^{\text{tot}}$  represents an ordering term and might be considered as an effective energy term. We already have some insight into the optimal, ordered state of the system without noise. In the opposite limit of high noise, elastic signals are too weak to influence cellular orientations and one expects completely random, disordered structures. The functional  $F$  therefore might be a reasonable starting point to include stochastic effects into our model, since it accurately describes the  $T = 0$ -limit (no noise) and the  $T \rightarrow \infty$  limit.

Of course there are many caveats associated with this approach. For example, cells are dynamic, active, non-equilibrium entities and there is no guarantee that the system is ergodic. Secondly, so far  $W$  was only a measure to characterize the mechanical properties of the environment which relates to the true cellular decision function in an unknown way. The sole restriction was that the minimum of  $W$  corresponds to the optimal state. We now assume that  $W$  indeed represents an ordering function. Despite these restrictions, Monte Carlo simulations might still provide useful insight into basic stochastic effects involved in cellular structure formation. Moreover, from a practical

point of view they are very convenient, since they allow to use well developed methods from statistical physics. Finally, the same approach has been used by others before in a similar context [120, 121].

In our Monte Carlo simulations we typically consider  $N \approx 1000$  dipoles. In order to minimize the effects of boundaries we apply periodic boundary conditions (pbcs), such that each dipole has the same number of next neighbors and experiences the same local geometry. We implement pbcs using the minimal image convention [122], i.e. we only consider the interactions of the dipole with its  $N - 1$  nearest (image) particles. For 2D simulations the  $r^{-3}$ -decay of the elastic interactions is fast enough that the correction term induced by truncating the interactions at a finite distance remains finite, and the minimal image convention is a good approximation [122]. The minimal image convention has also been used before to simulate elastic interactions of physical dipoles in 3D [123].

We use the standard Metropolis algorithm to generate typical configurations, i.e. a Monte Carlo move is always accepted, when it decreases  $w^{\text{tot}}$  and otherwise it is accepted with the probability  $p = \exp\left(-\frac{\Delta w^{\text{tot}}}{k_B T}\right)$ . In our case the temperature  $T$  represents a measure for the degree of stochasticity involved in cellular decision making. It is convenient to define a reduced temperature

$$T^* = \frac{k_B T \pi E \bar{b}^3}{P^2}, \quad (5.5)$$

where  $\bar{b}$  is the average distance between two particles in the simulation box.  $\bar{b}$  is related to the absolute area density by  $\langle \rho \rangle = 1/\bar{b}^2$  and in 3D by  $\langle \rho \rangle = 1/\bar{b}^3$ . The reduced temperature  $T^*$  measures the relative importance of noise  $k_B T$  with respect to the average elastic interaction strength,  $w \propto \frac{P^2}{\pi E \bar{b}^3}$ . For simulations with fixed dipole positions, each Monte Carlo move consists of a random selection of one dipole in the simulation box whose orientation is subsequently changed at random.

### Effect of Noise for Dipoles on a Lattice

In order to study the effect of noise on structure formation for dipoles on a square and hexagonal lattice respectively, we performed Monte Carlo simulations for  $N = 900$  dipoles at different values of the Poisson ratio  $\nu = 0, 0.1, 0.2, 0.3, 0.4, 0.5$  and at different values of the reduced temperature  $T^*$ . In order to work at the same dipole density, the hexagonal and square lattice constants are related by  $b_h = \sqrt{2/\sqrt{3}} b_s$ . Starting from a random configuration typically less than  $10^3$  Monte Carlo sweeps were required to reach thermal equilibrium.

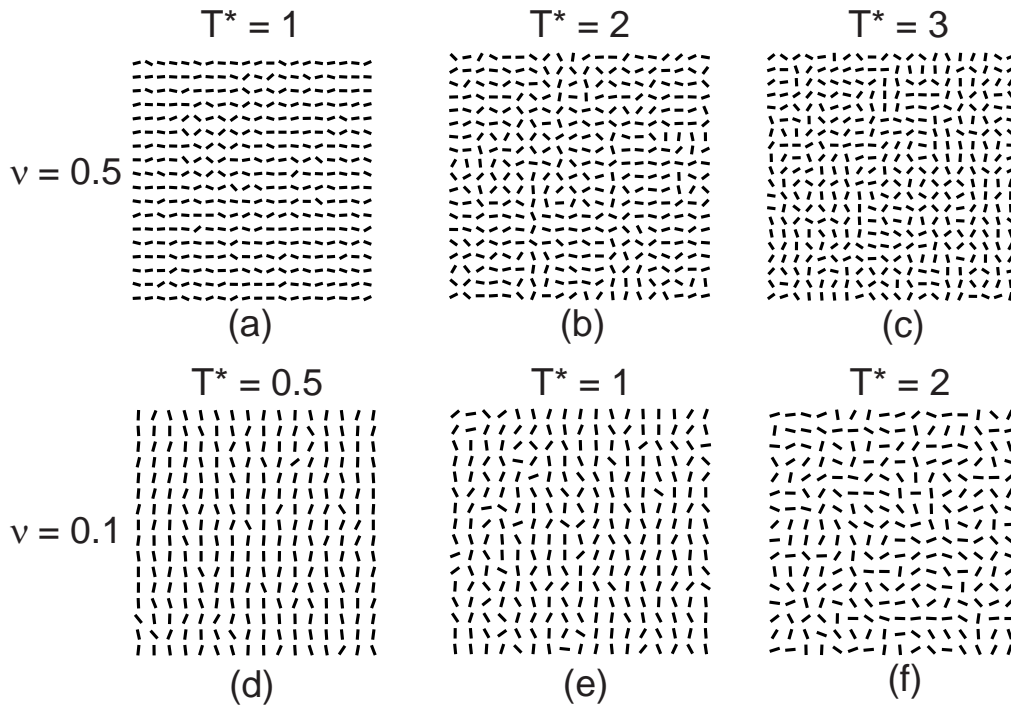


Figure 5.5: Typical patterns for dipoles fixed on a square lattice on top of an elastic half space with  $\nu = 0.5$  (a-c) and  $\nu = 0.1$  (d-f), respectively. Temperature increases from left to right. (a) For  $\nu = 0.5$  the dominant fluctuations around the optimal state are cooperative hedgehog fluctuations. (b,c) With increasing  $T^*$  domains of short strings along  $(1,0)$  and  $(0,1)$  coexist—often separated by hedgehog domains. (d-f) For  $\nu = 0.1$ , hedgehogs are less prominent and dipoles typically weakly fluctuate around the optimal orientations. With increasing  $T^*$  numerous domains of short string-like domains along  $(1,0)$ ,  $(0,1)$  and  $(1,1)$ ,  $(1,-1)$  coexist.

In Fig. 5.5 and Fig. 5.6 we show typical snapshots for dipoles fixed on a square and hexagonal lattice, respectively, on top of an elastic half space with  $\nu = 0.5$  and  $\nu = 0.1$ . The temperature increases from left to right. Note that for illustration purposes, we only plot a section of the full configuration.

On the square lattice dipoles at low noise levels form string-like structures, where the rotational symmetry is spontaneously broken along either direction of the principal lattice vectors  $(1,0)$  or  $(0,1)$ . For incompressible media ( $\nu = 0.5$ ), the typical fluctuations around the optimal string state are cooperative fluctuations of several dipoles generating hedgehog defects, see Fig. 5.5(a). Since for incompressible substrates the hedgehog structure is only slightly disfavored with respect to strings, it is "excited" very easily at low  $T^*$ . With increasing  $T^*$  we find smaller and smaller domains of short  $(1,0)$  and  $(0,1)$ -strings often separated by hedgehog-like domains, see Fig. 5.5(b,c). The

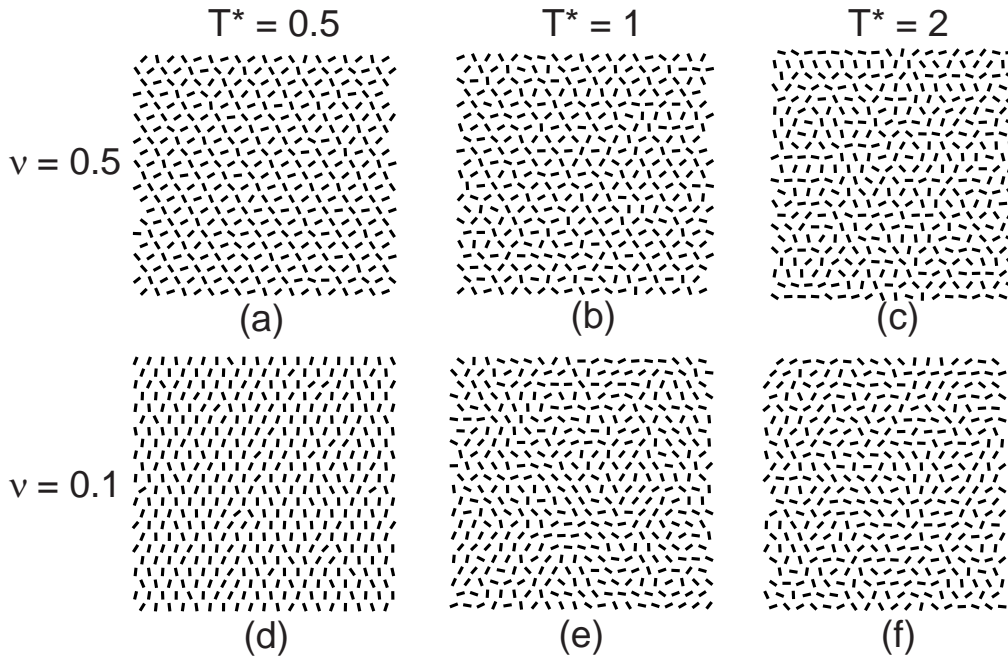


Figure 5.6: Typical patterns for dipoles on a hexagonal lattice on top of an elastic half space with  $\nu = 0.5$  (a-c) and  $\nu = 0.1$  (d-f), respectively.  $T^*$  increases from left to right. (a) At  $T^* = 0.5$  weak fluctuations around the optimal ring-like structure dominate. (e,f) At  $T^* = 1$  and  $T^* = 2$ , ring-like domains form and typically short isolated string-like and small ring-like structures dominate. (d) For  $\nu = 0.1$  four string-like structures have degenerate  $w^{\text{tot}}$  and one finds coexistence of many string-like domains (often with similar orientations) even at low  $T^*$ . (e,f) At  $T^* = 1$  and  $T^* = 2$  complementary string domains form.

structures become increasingly disordered and the orientations are distributed isotropically.

With decreasing Poisson ratio, hedgehog defects become less frequent since the penalty for ring-like structures increases with decreasing Poisson ratio. Typical cooperative fluctuations at low Poisson ratio are domains derived from the  $s(1,0)$ - and  $s(0,1)$ - as well as from the  $s(1,1)$ - and  $s(1,-1)$ -structures, see Fig. 5.5(d-f). Since the penalty of the diagonal string structure (s-b) with respect to (s-a) decreases to zero with decreasing  $\nu$ , it is excited more easily on highly compressible substrates than on incompressible substrates.

On the hexagonal lattices the optimal ordered state depends strongly on the Poisson ratio. For incompressible substrates the ring-like structure (h-c) dominates and at low noise intensities dipoles typically fluctuate only weakly around their optimal orientations, see Fig. 5.5(a). Increasing the

noise level as in Fig. 5.5(b,c), we find coexistence of domains of the two optimal ring-like structures directed along  $h(1,0)$  or  $h(0,1)$ , isolated short strings running along the hexagonal lattice vectors and various other ring-like structures.

When the Poisson ratio is decreased, the ring-like structures are again destabilized with respect to string-like structures at low  $T^*$ . An interesting regime exists around  $\nu \approx 0.32$ , where both large ring- and string-like domains coexist (not shown), since they are almost equally favorable. At even smaller  $\nu$ , as shown Fig. 5.6(d-f), we typically find coexistence of domains of short parallel strings. Since the  $h(1,0)$ - and  $h(1,1)$ -string structures are degenerate, we often find coexistence of such domains at low  $T^*$ , often with similar orientations, e.g.  $h(0,1)$  and  $h(1,1)$ . When noise increases, also the complementary string segments along  $h(0,1)$  and  $h(-1,1)$  are found and the overall structure becomes isotropic.

### Structure and Effective Mechanical Properties

We already mentioned that the mechanical activity of cells is expected to influence the material properties of the composite material (or tissue equivalent). In particular, when all cells direct their mechanical activity along a common direction, this will modify the mechanical properties in an anisotropic way. In contrast, when cells form disordered or ordered ring-like structures the averaged material properties remain (effectively) isotropic.

In order to address the mechanical properties of the composite material of cells and elastic medium, we aim to define a global order parameter  $\langle p \rangle$ , which should be able to distinguish between anisotropic and (effectively) isotropic structures, which result either from disorder or because of effectively isotropic orientational ordering as in the ring-like patterns. Suppose all dipoles point along the director  $\vec{n}$ , then  $\langle \cos^2 \beta \rangle = 1$ , where  $\beta$  is the angle of the dipole orientation with respect to  $\vec{n}$  and  $\langle \rangle$  denotes a configuration average. For disordered and ring-like structures, one gets  $\langle \cos^2 \beta \rangle = \frac{1}{2}$ . Thus, a suitable order parameter to distinguish these structures is  $p = 2(\langle \cos^2 \beta \rangle - \frac{1}{2})$ , which yields  $p = 1$  for string-like and  $p = 0$  for effectively isotropic (ring-like or disordered) structures. For our lattice structures the director  $\vec{n}$  only takes discrete values, e.g.  $(1,0)$  and  $(0,1)$  for the square lattice, because the underlying symmetries of the lattice support only distinct directions for discrete symmetry breaking ("crystal field effect"). However, for later purpose, it is convenient to calculate  $p$  in such a way that the direction of  $\vec{n}$  can vary. We therefore define a 2D analog of the nematic order parameter  $p$  used for the theory of liquid

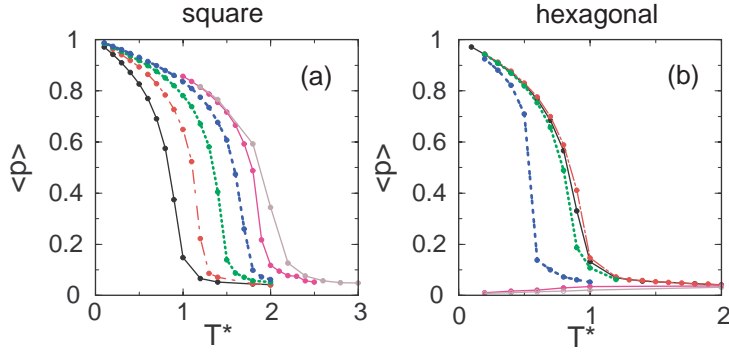


Figure 5.7: The averaged order parameter  $\langle p \rangle$  relates the degree of structural anisotropy to the effective material properties. (a)  $\langle p \rangle$  on a square lattice as a function of noise  $T^*$  for  $\nu = 0, 0.1, 0.2, 0.3, 0.4, 0.5$  (from left to right). (b) On a hexagonal lattice  $\langle p \rangle = 0$  for  $\nu = 0.4, 0.5$  and  $\langle p \rangle \rightarrow 1$  for  $\nu = 0.3, 0.2, 0.1, 0$  from left to right.

crystals [124]. We introduce the ordering matrix  $Q$ :

$$Q_{ij} = \frac{1}{N} \sum_{\alpha=1}^N (P_{ij}^{\alpha} - \frac{1}{2} \delta_{ij}), \quad (5.6)$$

where  $P_{ij}$  is the dipole tensor of the  $\alpha$ 'th particle and the sum runs over all particles in the simulation box. The largest eigenvalue  $\lambda_{\max}$  of the symmetric ordering matrix  $Q$  defines the order parameter  $p = 2\lambda_{\max}$ .  $p$  measures the degree of rotational order with respect to the director  $\vec{n}$ , which is the corresponding eigenvector to the maximal eigenvalue. The averaged order parameter  $\langle p \rangle$  is obtained by averaging  $p$  over  $M$  configurations:

$$\langle p \rangle = \frac{2}{M} \sum_{J=1}^M \lambda_{\max}^J. \quad (5.7)$$

In Fig. 5.7 we plot  $\langle p \rangle$  for both square (a) and hexagonal (b) lattice for different values of the Poisson ratio as a function of temperature  $T^*$ . The results were obtained from simulations with 900 dipoles. On a square lattice  $\langle p \rangle$  approaches 1 for all values of  $\nu$  when the elastic effects dominate noise and the system moves from an isotropic disordered into an anisotropic ordered state. We furthermore observe that in the square lattice ordering is facilitated with increasing  $\nu$ . This is expected because the elastic signals increase with increasing  $\nu$ . For a hexagonal lattice only substrates with  $\nu = 0.3, 0.2, 0.1, 0$  support string-like structures,  $\langle p \rangle \rightarrow 1$ , toward low  $T^*$ , also revealing a more complicated temperature dependence with  $\nu$ . For substrates with  $\nu = 0.4, 0.5$  one finds  $\langle p \rangle \approx 0$  at any value of  $T^*$ . Here, the orientational ordering transition

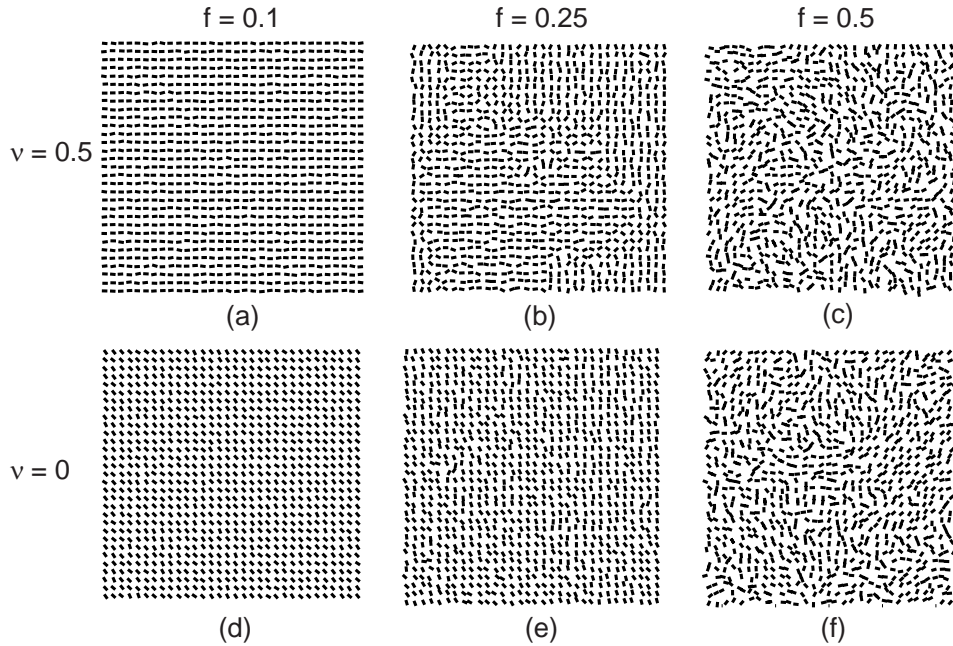


Figure 5.8: Monte Carlo snapshots at  $T^* = 0.1$  for dipoles randomly displaced from an ideal square lattice for  $f = 0.1, 0.25, 0.5$  from left to right for  $\nu = 0.5$  (a-c) and  $\nu = 0$  (d-f), respectively. Increased positional disorder destroys long-ranged orientational order in a similar way as an increase in  $T^*$  on an ideal lattice. Uniform deviations from the square lattice retain some quadratic order  $\lambda_4 = 0.95, 0.6, 0.15$  (left-right). This could explain, why there occurs no transition to ring-like structures on incompressible substrates.

with decreasing  $T^*$  occurs from an disordered isotropic to an ordered—but effectively isotropic—ring-like structure.

### Effect of Fluctuations around Lattice Positions

A second type of perturbations of the ideal structure might be interesting from a practical point of view, namely deviations from the ideal lattice positions. It is known that the shape of islands can influence the cellular force distribution [113, 114]. Thus, one might be forced to use larger islands to minimize these effects, which on the other hand means that cells may not adopt the perfect lattice positions. To simulate this effect, dipole positions were randomized around the perfect square lattice by displacing dipoles randomly (uniformly) within a circle around the lattice positions. Positions were then fixed for the simulation. The radius  $r$  of the circle is a fraction  $f = r/b$  of the lattice constant  $b$ . For the calculation in Fig. 5.8, we choose  $f = 0.1, 0.25, 0.5$  and  $\nu = 0.5$  and  $\nu = 0$ , respectively and show results for a low value of the reduced temperature, i.e.  $T^* = 0.1$ . A 10% uniform deviation from the lattice positions

has only a minor effect on orientational ordering and we find highly ordered string-like structures in both cases. In fact, on incompressible substrates the positional perturbations might suppress cooperative hedgehog fluctuations and thus increase ordering at low noise intensity. Increasing  $f$ , string domains (as well as hedgehog domains) form and long-ranged orientational order gradually disappears. With increasing  $f$  domains shrink and structures appear increasingly disordered. Thus, positional disorder effects orientational ordering in a similar way as increasing the temperature  $T^*$  on a perfect lattice.

As will be shown in Section 5.2, on incompressible substrates ( $\nu = 0.5$ ), positional disorder typically favors the formation of rings with respect to strings. Interestingly, we do not find such a transition in the present case. The reason probably is that uniform positional disorder around a square lattice still retains some long-ranged quadratic bond-orientational order for the dipole positions. To quantify this effect one can calculate the quadratic order parameter  $\lambda_4$ , which is defined in analogy to the hexatic order parameter for hexagonal bond-order [124, 125]:

$$\lambda_4 = \frac{1}{N} \sum_i^N \sum_j^{n_i} \frac{e^{4i\theta_{ij}}}{n_i}, \quad (5.8)$$

where  $N$  is the number of dipoles and  $n_i$  is the number of neighbors of dipole  $i$  found in a circle of radius  $r = 1.3b$ .  $\theta_{ij}$  is the angle of the line from particle  $i$  to  $j$  with respect to an arbitrary, but fixed global axis.  $\lambda_4 = 1$  corresponds to perfect long-range quadratic order and  $\lambda_4$  becomes zero when dipole locations square lattice correlations and become completely disordered. We calculate  $\lambda_4$  and find  $\lambda_4 > 0$  up to 50% uniform deviations around the square lattice positions. For the configurations in Fig. 5.8 we find  $\lambda_4 = 0.95, 0.6, 0.15$  for  $f = 0.1, 0.25, 0.5$ , respectively. The persistent quadratic orientation correlations between dipole positions may explain why we do not observe rings on incompressible substrates, because the square lattice supports string-like structures even on incompressible substrates. Hence, although string-like structures are increasingly disfavored with respect to ring-like structures with increasing Poisson ratio, the square lattice geometry is able to stabilize them and moderate deviations around square lattice positions are not sufficient to destabilize them. The geometry dependent transition from ring-like to string-like structures on incompressible substrates might therefore be observable experimentally.

## 5.2 Structures for Positional Disorder

For typical *in vivo* and *in vitro* situations, for example when cells are cultured on conventional elastic substrates, cellular positions are less well defined than

for the lattice structures discussed above. We now study structure formation of contraction dipoles on conventional elastic substrates as a function of material properties and dipole density using Monte Carlo simulations. We again focus on orientational degrees of freedom only, since it is generally assumed that the cellular orientational degrees of freedom relax much faster than positional degrees of freedom [126]. In more biological terms: significant cell locomotion occurs on a much slower time scale than orientational reorganization of the cytoskeleton, which might be further reduced by using less motile cell strains or appropriate drugs. We therefore again neglect effects of cell locomotion and fix the dipole positions for the simulations, and vary the orientations only.

The most interesting question is whether and under what conditions elastic interactions are able to mediate a spontaneous breaking of the rotational symmetry for cellular structures, which contribute to anisotropic material properties. For square and hexagonal lattices, discrete two-fold rotational symmetry breaking occurs as a function of temperature  $T^*$ , Poisson ratio  $\nu$  and lattice geometry. In this case, the underlying lattice symmetries support discrete space directions for symmetry breaking. Under certain conditions, elastic interactions might also break the continuous  $O_2$ -rotational symmetry without requiring to break the translational symmetry and thus yield a nematic phase similar to liquid crystals.

### Introduction: State Variables of Structure Formation

One might expect that structure formation on elastic substrates depends on three variables: the reduced temperature  $T^*$ , the Poisson ratio  $\nu$  (as for lattice structures) and the density  $\rho$ . The cell density will affect structure formation in two ways. On the one hand, a large average density  $\langle\rho\rangle$  means that dipoles come closer together, which will increase the elastic signal with respect to noise. This effect can be subsumed into a decrease in the reduced temperature, since  $T^* = \frac{TE\pi\langle\rho\rangle^{\frac{3}{2}}}{P^2}$ . On the other hand, depending on the density, some short-ranged position correlations between dipoles may emerge. For example, at high cell density, the area occupied by one cell is not accessible to another (excluded area interaction), which will lead to correlations between dipole positions. We now associate with each cell a circular disk with radius  $a$  and assume that the mechanical action of the cell (i.e. the force dipole) is located at the disk's center. The physical meaning of the disk might either be the cell area, as mentioned above, or more general, some typical area surrounding cells that is not accessible to other cells due to some kind of repulsive interaction, e.g. contact inhibition [127]. One could also implement this situation artificially by using irregular spaced adhesive islands of circular shape on a non-adhesive substrate, where islands are not allowed to overlap.

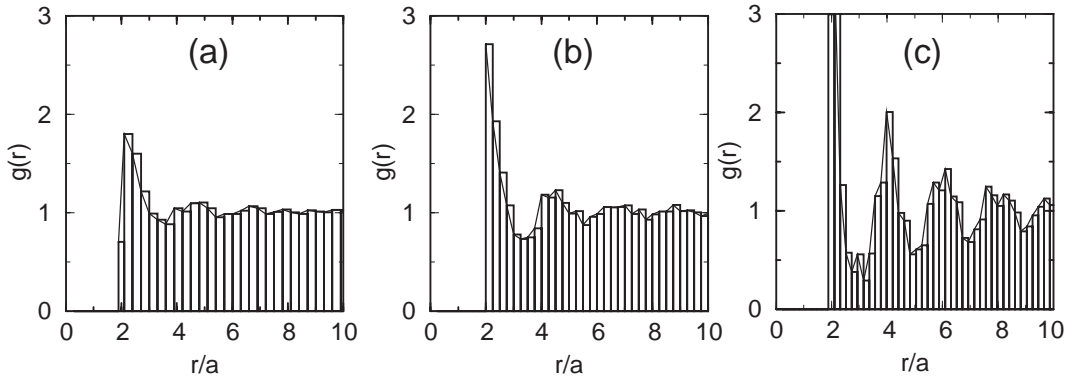


Figure 5.9: Radial distribution function  $g(r)$  obtained from simulations at reduced densities of  $\rho^* = 0.34, 0.5, 0.74$  (left-right). With increasing packing fraction  $\rho^*$  short-ranged pair correlations develop due to the non-overlap constraint between disks which are characteristic for a liquid of hard disks [128].

One can then introduce a reduced density  $\rho^*$  defined as

$$\rho^* = \frac{N\pi a^2}{L^2}, \quad (5.9)$$

which is a dimensionless variable describing the ratio of the area occupied by  $N$  circular disks of radius  $a$  to the area of the (simulation) box with side lengths  $L$ . The emergence of short-ranged correlations with increasing  $\rho^*$  can be illustrated by calculating the density pair correlation function  $g(g)$ , which for an isotropic, translationally-invariant position-distribution only depends on the distance  $r$  between disks [128]:

$$g(r) = \frac{1}{\langle \rho \rangle} \left\langle \sum_{\alpha \neq \beta} \delta(|\vec{r} - \vec{r}^{\alpha, \beta}|) \right\rangle. \quad (5.10)$$

$\vec{r}^{\alpha, \beta}$  is the distance between particles  $\alpha$  and  $\beta$ .

In Fig. 5.9 we show numerical results for  $g(r)$  for different  $\rho^*$  obtained by randomly placing  $N = 1024$  disks of radius  $a$  into a simulation box of area  $L^2$ , where disks are not allowed to overlap. The  $\rho^* = 0$  case corresponds to an ideal gas, where the the probability to find a particle at any distance  $r$  is a constant, i.e.  $g(r) \rightarrow 1$ . With increasing  $\rho^*$ , short-ranged position correlations emerge indicated by the short-ranged oscillations in  $g(r)$  at small  $r$ , which are typical for a liquid of hard disks [128]. In a dense liquid the probability to find a second particle at  $r/a < 2$  is zero, while the probability to find a second particle a distance  $2a$  and subsequently at  $4a$  etc. is enhanced. Thus, with increasing  $\rho^*$ , correlations between positions develop due to the non-overlap constraint. Therefore,  $\rho^*$  is a measure for geometric correlations between dipole positions, which may affect structure formation.

We should mention that the phase-diagram for hard disks has been obtained by Monte Carlo simulations [125]. It predicts an isotropic liquid phase for  $\rho^* < 0.88$  with short-ranged position correlations and a hexagonal crystallite phase for  $\rho^* > 0.905$ , with truly long-ranged position correlations. The maximal packing fraction for disks in 2D is achieved in a hexagonal lattice, which yields  $\rho^* \approx 0.907$ . In between the solid and liquid phase, there is a small band of a hexatic phase, with long-ranged bond-orientational, but no long-ranged translational order [125]. Most results for structure formation under positional disorder presented in the next section correspond to simulations at values of  $\rho^*$  in the liquid regime. The solid regime, with perfect positional long-ranged order, has been considered already by studying the hexagonal lattice structures in Section 5.1.2.

### Monte Carlo Simulations

We now study pattern formation on elastic substrates as a function of the reduced temperature  $T^*$ , the Poisson ratio  $\nu$  and the reduced density  $\rho^*$  by Monte Carlo simulations. For the simulation,  $N = 1024$  disks of radius  $a$  are randomly placed into a simulation box of length  $L$  under the non-overlap constraint for disks, which yields  $\rho^* = \frac{N\pi a^2}{L^2}$ . Dipoles are fixed at the disks' center and orientations varied as before. All other parameters and conditions for the Monte Carlo simulation were identical to the ones described in Section 5.1.2.

Fig. 5.10 shows typical snapshots of structures at  $T^* = 0.1$  for dipoles on an elastic substrate with  $\nu = 0, 0.25, 0.35, 0.5$  (top–bottom) at different values of the reduced density  $\rho^* = 0, 0.4, 0.5$  (left–right). At low densities, dipoles predominantly optimize locally the interaction between them by forming short string-like clusters, with no obvious long-range correlation between clusters. This leads to rather robust pattern formation that does not differ qualitatively as the Poisson ratio is varied, see Fig. 5.10(a). One expects that these patterns represent typical cellular structures formed, when cells in dilute concentrations are suspended on an elastic substrate and adhere at random positions ( $\rho^* \rightarrow 0$ ). With increasing  $\rho^*$  the respective structures at low noise intensity show a strong dependence on the Poisson ratio  $\nu$  and an increasing similarity to the hexagonal lattice structures. For incompressible substrates we find isotropic ring-like structures often composed of only four dipoles reminiscent to the small rings in the ring-like structure (h-c), see Fig. 5.10(IVc). With decreasing Poisson ratio, string-like patterns emerge. For example, for  $\nu = 0.35$  in Fig. 5.10(IIIc) we find coexistence of string-like and ring-like domains. String-like structures start to dominate for  $\nu < 0.32$ . For  $\nu = 0.25$  we observe that with increasing density strings start to interact and domains of aligned strings form, which increase in size with increasing  $\rho^*$ , see Fig. 5.10(IIb,IIc). With decreasing Poisson ratio,

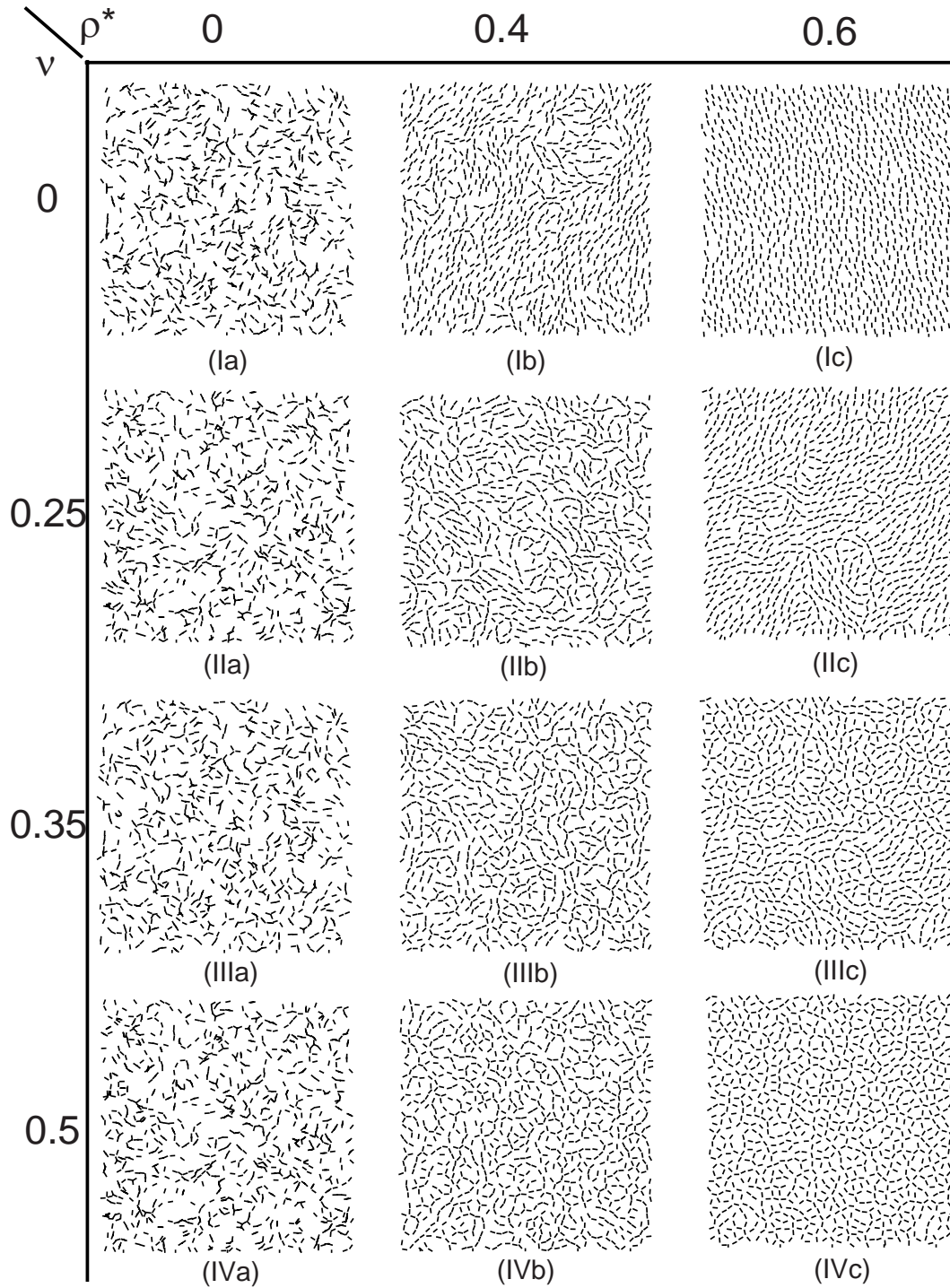


Figure 5.10: Snapshots of MC-simulations at  $T^* = 0.1$  for  $N = 1024$  dipoles on an elastic substrate with  $\nu = 0, 0.25, 0.35, 0.5$ , respectively (top-bottom). The reduced density increases from left to right as  $\rho^* = 0, 0.4, 0.6$ , respectively, while the average density  $\langle \rho \rangle$  remains constant.

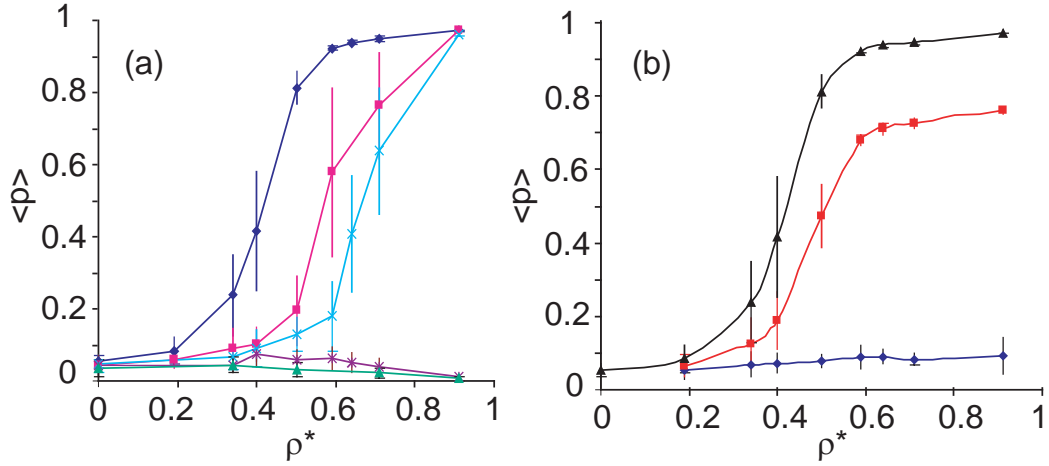


Figure 5.11: Nematic order parameter  $\langle p \rangle$  as function of the reduced density  $\rho^*$  obtained from MC-simulations with 1024 dipoles. (a) Nematic ordering occurs only on compressible substrates and above a critical density. Curves show numerical results for  $\nu = 0, 0.25, 0.3$  (left-right) and  $\nu = 0.4, 0.5$  (bottom), respectively. (b) Nematic ordering disappears above a certain noise level. Results shown were obtained for  $\nu = 0$  at  $T^* = 0.1, 0.6, 1.1$  (top-bottom).

alignment along a common direction is favored and in Fig. 5.10(Ic) we find an aligned structure, which could qualify as nematic structure.

In order to quantify these results, we could calculate the nematic order parameter  $\langle p \rangle$  defined in Eq. (5.7). Computationally,  $p$  is now first thermally averaged for a fixed configuration of the dipole positions and subsequently averaged over at least 20 random position configurations obtained for the same  $\rho^*$ .

In Fig. 5.11a we plot the averaged nematic order parameter  $\langle p \rangle$  at  $T^* = 0.1$  as a function of the effective density  $\rho^*$  for various values of the Poisson ratio  $\nu$ . For completeness we also include our numerical results obtained for the hexagonal lattice structure, which correspond to  $\rho^* \approx 0.907$ . We find that  $\langle p \rangle$  becomes different from zero above a critical density  $\rho_c^*(\nu)$  and below a critical value of the Poisson ratio  $\nu \approx 0.32$ . This indicates the formation of a nematic structure. The degree of structural alignment increases with increasing  $\rho^*$  and approaches 1 toward  $\rho^* = 0.907$ . In contrast, for  $\nu = 0.4, 0.5$  no nematic ordering occurs at any density  $\rho^*$  or temperature  $T^*$ . In this case, the disorder-order transition with decreasing  $T^*$  does not break the orientational symmetry with a two-fold axis and ordered structures remain effectively isotropic, since dipoles form small ring-like structures. Thus,  $\langle p \rangle \rightarrow 0$ .

In Fig. 5.11(b) we plot  $\langle p \rangle$  for  $\nu = 0$  at different values of the reduced temperature  $T^*$ . With increasing temperature, entropy dominates and the ne-

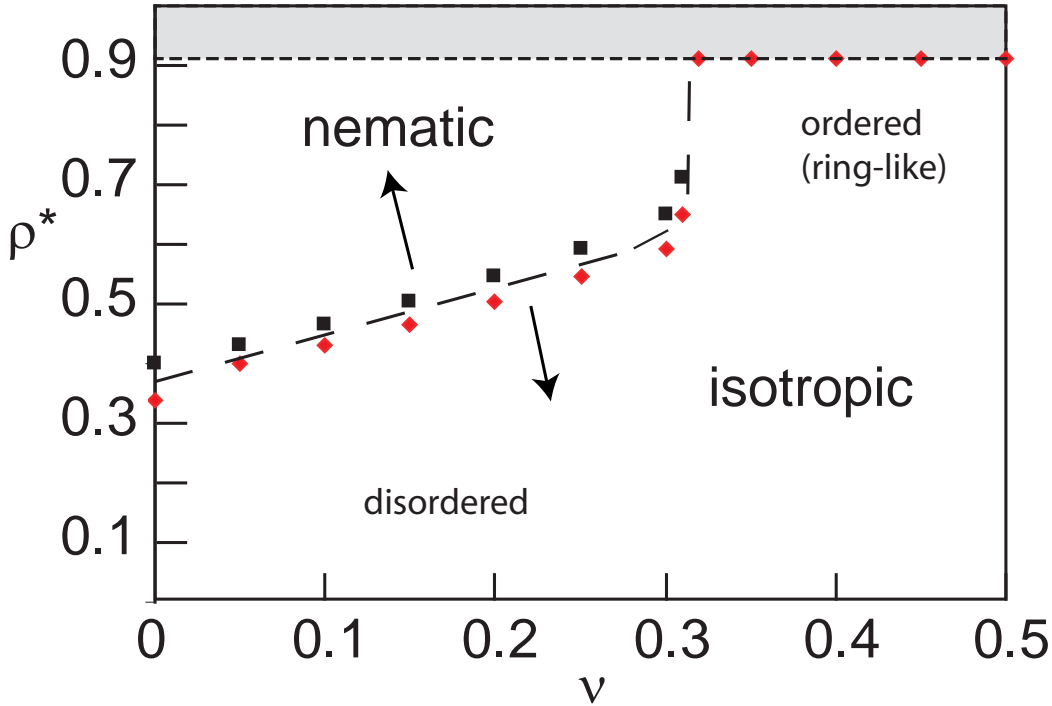


Figure 5.12: Structural phase-diagram for  $T^* = 0.1$  for dipoles on elastic substrates obtained by Monte Carlo simulations. All points below diamonds have  $\langle p \rangle < 0.4$  and all points above squares yield  $\langle p \rangle > 0.4$ . The long dashed line is our estimate for the iso-line with  $\langle p \rangle = 0.4$ . The horizontal dashed line marks the maximal  $\rho^*$  obtained for a hexagonal lattice.

nematic structure is destabilized with respect to disordered isotropic structures, such that above a critical  $T^*$ ,  $\langle p \rangle = 0$ .

We may summarize our results by plotting a schematic structural phase diagram. We do not aim at solving the full thermodynamic problem for our "effective" potential, although this might be interesting from an academic point of view. Instead we aim at providing a quantitative estimate, where to expect nematic or more isotropic structures, experimentally. In Fig. 5.12 we plot our numerical results for  $T^* = 0.1$  as a function of the state variables  $\nu$  and  $\rho^*$ . Diamonds yield  $\langle p \rangle < 0.4$  and squares  $\langle p \rangle > 0.4$ , the dashed line denotes our estimate for an isoline with  $\langle p \rangle = 0.4$ . For substrates with small Poisson ratio, i.e. below  $\nu < 0.32$ , an isotropic-nematic transition occurs above a critical density  $\rho_c^*$ , which increases with increasing  $\nu$ . Above  $\rho_c^*$  strings form and interact to form an aligned nematic structure. Despite low  $T^*$ , structures with  $\rho < \rho_c^*$  become increasingly disordered, with the formation of short uncorrelated strings. The nematic-isotropic transition with  $\rho^*$  represents therefore

an order-disorder transition. When the Poisson ratio comes close to  $\nu \approx 0.3$  the critical density for a nematic structure shoots up and beyond  $\nu = 0.32$  we do not find a nematic structure at any  $\rho^*$ . In contrast to highly compressible substrates ( $\nu < 0.32$ ), the disorder-order transition with  $\rho^*$  towards incompressible substrates ( $\nu < 0.32$ ) retains effectively isotropic material properties because the ordered structures are ring- rather than string-like.

### Conclusion

In conclusion, we identified three state variables which determine structure formation of elastically interacting contraction dipoles on elastic substrates: the reduced density  $\rho^*$ , the Poisson ratio  $\nu$  and the reduced temperature  $T^*$ . For sparsely populated elastic substrates without position correlations  $\rho^* \rightarrow 0$ , the structure formation is independent on the properties of the elastic substrate. In this case pattern formation is robust and characteristic structures expected from elastic interactions is the formation of short strings and sometimes larger rings. At higher densities structure formation at low noise depends strongly on the material properties of the elastic substrate. The model predicts an isotropic-nematic transition beyond a critical density  $\rho$  and below a critical  $T^*$ , but only on highly compressible substrates  $\nu < 0.32$ .

For liquid crystals the isotropic-nematic transition depends on the aspect ratio of the asymmetrically shaped molecules and the reduced density. In this case, the density dependence might be intuitively plausible because the transition is driven by the (short-ranged) excluded volume interaction of the asymmetrically shaped molecules causing the alignment of molecules along the molecules' long axis. Thus, molecules have to be close together to interact with each other. The existence of a critical density to form a nematic phase might be less obvious for elastic interactions, since elastic interactions are in principle long-ranged. However, the formation of a nematic structure for dipoles requires not only the formation of strings, but also correlations and thus, interactions between strings. Since the interaction between strings is effectively short-ranged, strings (or the dipoles forming the strings respectively) have to be close together to cause the common alignment. ("close" means that the distance between cells within the string should be approximately the same as the distance between strings). This explains why short-ranged position correlation between dipoles are necessary to support a nematic structure.

The dependence of the isotropic-nematic transition on the Poisson ratio of the elastic substrate is essentially the same as found for the hexagonal lattice structures and occurs around  $\nu \approx 0.32$ , where string- and ring-like structures in the hexagonal lattice have degenerate values. In fact, the patterns formed on incompressible substrates at high density are ring- rather than string-like and are often reminiscent of the small four-dipole-rings found in the hexagonal

ring-like structure (h-c). The typical angular short range correlation in a liquid are typically hexatic rather than quadratic, i.e. each dipole has approximately six next neighbors at the same distance  $a$ , which is a likely explanation for the resemblance of the high density liquid structures to the hexagonal lattice structures. Besides, for small Poisson ratio, the director field in the hexagonal lattice was less determined by the lattice symmetries, as more string-like structures become equally favorable. Thus, the available phase space for string-like structures increases on highly compressible substrates, which supports the formation of oriented string-like structures with long-ranged orientation correlations.

### 5.3 Discussion and Outlook

In this chapter we focused on structure formation of cells due to elastic interactions and studied orientational patterns of force dipoles on elastic substrates both analytically and numerically by Monte Carlo simulations. We identified three (state) variables which control pattern formation due to elastic effects: the (reduced) cell density  $\rho^*$  or equivalently the geometry of cell positioning, the material properties of the elastic medium, in particular the Poisson ratio  $\nu$ , and the relative strength of elastic signals to the degree of stochasticity involved in cellular decision making specified by  $T^*$ . In principle all state variables are experimentally accessible.

In particular, the combination of microcontact printing with the elastic substrate method to control cell positioning provides a well defined protocol, to test our predictions experimentally. In this case, the spacing between islands should be large enough that our approximation to model cellular force fields as contraction dipoles is valid and on the other hand it should be small enough that elastic cues are strong enough to allow for sufficient self-organizing activity due to elastic signals. In practice, this means that the spacing between islands should be of the order of the cell size  $\approx 100\mu\text{m}$ .

Another important parameter is the reduced temperature  $T^* = \frac{k_B T \pi E \bar{b}^3}{P^2}$ , which determines the relative weight of order and disorder in structure formation.  $T^*$  can be varied in many ways, without altering the degree of internal cellular stochasticity  $T$ . For example, a decrease in the average spacing  $\bar{b}$  between cells results in larger elastic signals and thus decreases  $T^*$ . Moreover, since large strain fields increase the strength of elastic interactions, it could be interesting to increase cellular contractility by applying contractile agents like LPA (lysophosphatic acid) to stimulate Rho-mediated contractility. This will increase  $P$  and thus again decrease  $T^*$ . Another way to access the effective  $T^*$  experimentally is to vary the Young modulus  $E$  of the material. Since  $W \sim 1/E$  elastic signals increase on softer materials (as long as the mechanical

activity of cells is not down-regulated at the same time) and thus effectively decreases  $T^*$ .

Since elastic interactions are propagated via the elastic medium, it might be not too surprising to find that changing the properties of the substrate can alter structure formation. For isotropic elastic substrates there are two constants, the Young modulus  $E$  and the Poisson ratio  $\nu$ . Our results suggest that  $E$  is primarily affecting the reduced temperature  $T^*$  and thus, allows to shift structures between ordered and disordered patterns, but does not affect the ordered structures qualitatively. In contrast, the Poisson ratio  $\nu$  alters ordered structures from string- to more ring-like structures. Most synthetic substrates have Poisson ratio close to 0.5, however, rapid advances in material science could allow to realize smaller values in the future.

In our simulations we excluded effects of cell locomotion to keep our model simple. Cell locomotion is important in many physiological situations e.g. in development or wound healing. Since our model provides also taxis through the position dependence of  $W$ , a simple way to incorporate cell locomotion into our model is to allow for positional degrees of freedom in the Monte Carlo simulations. In this case, one needs to include a repulsive interaction between dipoles, e.g. a hard-core repulsion, to avoid that at low  $T^*$  dipoles collapse onto a single point. In analogy to the so called Stockmayer fluids in electrostatics [105, 106, 129], which are composed of hard spheres with a electrical dipole moment at their centers, one could study a model of hard spheres with an associated contraction dipole interacting elastically with each other. For such a model simulations indicate that typical configurations at low dipole densities involve the formation of strings. At intermediate densities one observes the formation of a connected network of dipoles, similar to the case of electric dipoles. In general, we expect that the phase behavior of such a model at low to intermediate densities is similar to that dipolar fluids [106].

The Monte Carlo method used in this chapter is a convenient way to study the influence of perturbations on optimal cell organization. However, Monte Carlo simulations do not represent any dynamics and the structures predicted here represent averages one expects to find on large time scales. In order to treat the dynamics of structure formation and effects of cell locomotion more explicitly, more quantitative experimental data regarding cell behavior in response to mechanical cues is needed. Of particular interest are the dependence of cellular turning behavior, cell speed, persistence length etc. on rigidity gradients. This will allow us to refine the cellular decision function  $W$  and also to study dynamic aspects of structure formation in the future.

While here we focused on 2D elastic substrates, elastic interactions could also contribute to *in vivo* tissue organization in particular in the connective

tissue, which is sparsely populated by cells of the fibroblast family and rich in extra-cellular matrix proteins. The connective tissue is the major component of skin, tendon, the cornea, cartilage, bone and teeth and its organization is largely determined by the arrangement of collagen fibrils, which is at least partly driven by *self-assembly* of fibrils [1]. However, it is well known that the orientation of e.g. fibronectin fibrils is largely determined by the orientation of the cell secreting it. Moreover, cells use traction forces to actively rearrange the matrix after it has been deposited [51].

Although the modeling of cell behavior in fibrous gels is beyond the scope of this work our model suggests that at low cell density structure formation is largely independent of the exact material properties (as long as they are isotropic) and one expects alignment of cells into short strings or rings, without long-ranged correlation between strings because of the effective screening of elastic signals in the horizontal direction with respect to the string's axis. For dipoles in 3D positioned on a simple cubic lattice, simulations show that the optimal state exhibits a similar transition between effectively isotropic and aligned structures as a function of Poisson ratio as in 2D. In incompressible substrates ( $\nu = 0.5$ ), we find a hedgehog-like structure, where all dipoles at the corners point to the cube's center, see Fig. 5.13(a), while for  $\nu = 0$  spontaneous symmetry breaking along a principal lattice vector occurs, see Fig. 5.13(b). For (isotropic) hydrogels typically  $\nu = 0.5$ , and we therefore do not expect cells to spontaneously align due to elastic interactions in gels with isotropic material properties. However, anisotropic gel properties, e.g. caused by an alignment of collagen fibers, favor cell alignment because the elasticity along the fibers is expected to be larger than in the transverse direction. In this case, cellular traction forces could further stabilize cell alignment by putting fibers under tension. We indeed observe a similar effect in our simulations, when an elastic anisotropy is induced by external strain, see Fig. 5.13(c). The picture shows a snapshot of a Monte Carlo simulations of 100 hard spheres with an elastic dipole moment at their center, where we allowed for both orientational and positional degrees of freedom ( $T^* = 2$ ). In the simulation, we applied a homogeneous strain field along the  $z$ -direction ( $p = 1$ ). We find that cells not only align along the direction of stretch (as discussed in Chapter 3), but also form strings running along the stretch direction due to elastic interactions between them. The formation of cell strings along the direction of tensile strain has indeed been observed experimentally for fibroblasts in a stretched collagen gel [26].

As an aside we may mention that the collective response of fibroblasts to external strain could provide another clue how durotaxis or effective stiffness preference contribute to tissue maintenance. The principle suggests that cells migrate toward high strain areas and orient their mechanical activity in such a way as to pull back in response to external tensile strain. External strain

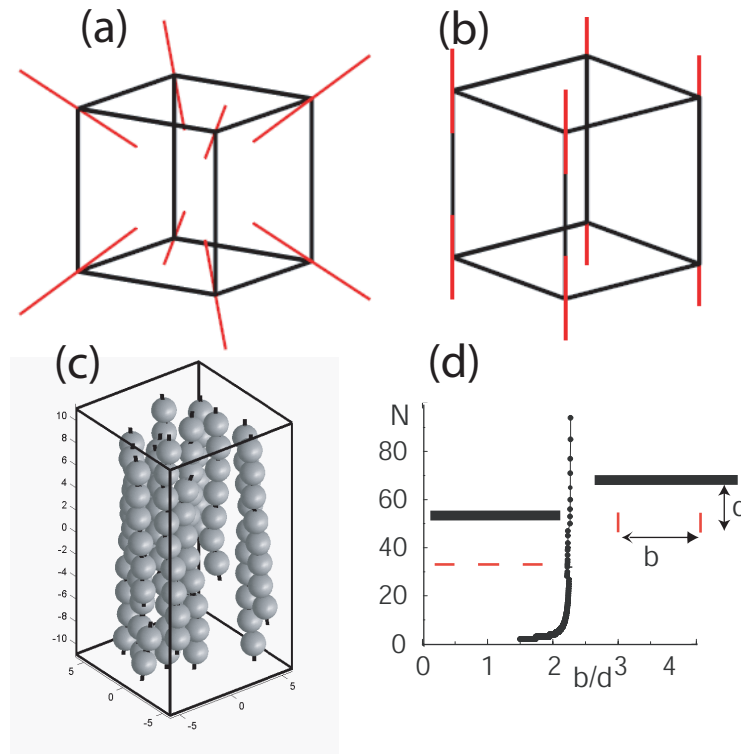


Figure 5.13: Overview about collective effects in 3D elastic substrates. (a,b) The optimal structure in a cubic lattice depends on the Poisson ratio  $\nu$ . In incompressible substrates ( $\nu = 0.5$ ) the isotropic hedgehog structure is most favorable (a) while on highly compressible substrates elastic interactions favor aligned structures (b). (c) Cells in external strain fields form strings running along the direction of stretch due to interactions with external strain and elastic cell-cell interactions. (d) Collective effects can modify preferred cell organization close to a clamped boundary.

is likely to be present in wounded areas. Then fibroblasts are attracted to this area by mechanotaxis (as well as chemotaxis). Moreover, in anisotropic strain fields, cells align along the direction of stretch, i.e. they pull against the external forces, which is probably what one would expect fibroblasts to do in order to close a wound.

Finally, we would like to point out that structure formation in finite 3D samples will also be affected by geometry and boundary condition. The direct interaction of single cells with boundaries given by  $W^b$  has been discussed in Chapter 3, while in Chapter 4 and 5 we focused on elastic interactions between cells without boundaries present. The presence of a boundary modifies the direct elastic interaction between cells  $W^{PP'}$  by boundary induced strain fields, which depending on boundary condition introduce either attractive

or repulsive contributions  $W_b^{PP'}$  to the elastic interaction [48, 54]. In finite sized geometries, like the elastic sphere, the boundary term varies on the macroscopic scale  $R$  and can introduce new maxima and minima into the interaction landscape. In this case, structure formation on elastic and cellular scales will compete with effects on the macroscopic scale  $R$  and we expect the formation of hierarchical structures [48, 54]. A nice example for a competition between the direct interaction with the boundary  $W^b$  and cellular interactions is the elastic half space with a clamped boundary, Fig. 5.13(d). When cells are lined up close to the boundary, the direct interaction with a clamped boundary favors cellular orientations pointing toward the surface. On the other hand, interactions between cells favor the formation of strings and thus, parallel orientations. Our calculations suggest that the transition between these two configurations is a function of the ratio  $b/d$ , where  $d$  is the distance to the boundary and  $b$  is the distance between cells, and the number of interacting cells  $N$ . When  $b/d > 2$  the direct interaction with the boundary always wins and cells are expected to point toward the surface.

To conclude, in this chapter we showed how elastic interactions between cells contribute to large scale tissue organization. We also briefly discussed how collective effects contribute (and sometimes alter) preferred cell organization with respect to other elastic signals like external strain or boundaries. In general many predictions of our model are in good agreement with experimental results [53], and we also proposed new experiments to test our theoretical ideas, for example to use micropatterned substrates to study elastic interactions between cells or to observe the behavior of many cells close to clamped boundaries. We expect that our model will be used to for biomedical applications in the future, for example to optimize protocols for tissue equivalents in regard to optimal sample geometry, boundary condition, material properties or cell density.

# Bibliography

- [1] B. Alberts, A. Johnson, J. Lewis, M. Raff, K. Roberts, and P. Walter.  
*Molecular biology of the cell.*  
Fourth edition. Garland Science, New York (2002).
- [2] A. Curtis and M. Riehle.  
*Tissue engineering: the biophysical background.*  
Physics in Medicine and Biology **46**, R47–R65 (2001).
- [3] D. Lauffenburger and J. Linderman.  
*Receptors: models for binding, trafficking, and signalling.*  
Oxford University Press, Oxford (1993).
- [4] P. Martin.  
*Wound healing - Aiming for perfect skin regeneration.*  
Science **276**, 75–81 (1997).
- [5] P. Weiss.  
*In vitro experiments on the factors determining the course of the outgrowing nerve fiber.*  
Journal of Experimental Zoology **68**, 393–448 (1934).
- [6] P. Weiss.  
*Experiments on Cell and Axon Orientation In vitro - the Role of Colloidal Exudates in Tissue Organization.*  
Journal of Experimental Zoology **100**, 353–386 (1945).
- [7] P. Weiss and B. Garber.  
*Shape and Movement of Mesenchyme Cells as Functions of the Physical Structure of the Medium - Contributions to a Quantitative Morphology.*  
Proceedings of the National Academy of Sciences of the United States of America **38**, 264–280 (1952).
- [8] G. A. Dunn and J. P. Heath.  
*New Hypothesis of Contact Guidance in Tissue-Cells.*  
Experimental Cell Research **101**, 1–14 (1976).
- [9] G. A. Dunn and T. Ebendal.  
*Contact Guidance on Oriented Collagen Gels.*  
Experimental Cell Research **111**, 475–479 (1978).

- [10] S. B. Carter.  
*Haptotaxis and Mechanism of Cell Motility.*  
Nature **213**, 256–260 (1967).
- [11] W. S. Haston, J. M. Shields, and P. C. Wilkinson.  
*The Orientation of Fibroblasts and Neutrophils on Elastic Substrata.*  
Experimental Cell Research **146**, 117–126 (1983).
- [12] R. J. Pelham and Y. L. Wang.  
*Cell locomotion and focal adhesions are regulated by substrate flexibility.*  
Proceedings of the National Academy of Sciences of the United States of America **94**, 13661–13665 (1997).
- [13] C. M. Lo, H. B. Wang, M. Dembo, and Y. L. Wang.  
*Cell movement is guided by the rigidity of the substrate.*  
Biophysical Journal **79**, 144–152 (2000).
- [14] J. Y. Wong, A. Velasco, P. Rajagopalan, and Q. Pham.  
*Directed movement of vascular smooth muscle cells on gradient-compliant hydrogels.*  
Langmuir **19**, 1908–1913 (2003).
- [15] D. Choquet, D. P. Felsenfeld, and M. P. Sheetz.  
*Extracellular matrix rigidity causes strengthening of integrin-cytoskeleton linkages.*  
Cell **88**, 39–48 (1997).
- [16] N. Q. Balaban, U. S. Schwarz, D. Riveline, P. Goichberg, G. Tzur, I. Sabanay, D. Mahalu, S. Safran, A. Bershadsky, L. Addadi, and B. Geiger.  
*Force and focal adhesion assembly: a close relationship studied using elastic micropatterned substrates.*  
Nature Cell Biology **3**, 466–472 (2001).
- [17] D. Riveline, E. Zamir, N. Q. Balaban, U. S. Schwarz, T. Ishizaki, S. Narumiya, Z. Kam, B. Geiger, and A. D. Bershadsky.  
*Focal contacts as mechanosensors: Externally applied local mechanical force induces growth of focal contacts by an mDia1-dependent and ROCK-independent mechanism.*  
Journal of Cell Biology **153**, 1175–1185 (2001).
- [18] A. K. Harris, P. Wild, and D. Stopak.  
*Silicone-Rubber Substrata - New Wrinkle in the Study of Cell Locomotion.*  
Science **208**, 177–179 (1980).
- [19] J. D. Murray, G. F. Oster, and A. K. Harris.  
*A Mechanical Model for Mesenchymal Morphogenesis.*

- Journal of Mathematical Biology **17**, 125–129 (1983).
- [20] J. D. Murray and G. F. Oster.  
*Cell Traction Models for Generating Pattern and Form in Morphogenesis.*  
Journal of Mathematical Biology **19**, 265–279 (1984).
- [21] D. G. Castner and B. D. Ratner.  
*Biomedical surface science: Foundations to frontiers.*  
Surface Science **500**, 28–60 (2002).
- [22] A. S. G. Curtis and C. D. Wilkinson.  
*Reactions of cells to topography.*  
Journal of Biomaterials Science-Polymer Edition **9**, 1313–1329 (1998).
- [23] A. Curtis and C. Wilkinson.  
*Topographical control of cells.*  
Biomaterials **18**, 1573–1583 (1997).
- [24] J. Y. Wong, J. Leach, and X. Brown.  
*Balance of chemistry, topography and mechanics at the cell-biomaterial interface: Issues and challenges for assessing the role of substrate mechanics on cell response.*  
Preprint (2004).
- [25] A. Engler, L. Bacakova, C. Newman, A. Hategan, M. Griffin, and D. Discher.  
*Substrate compliance versus ligand density in cell on gel responses.*  
Biophysical Journal **86**, 388A–388A (2004).
- [26] M. Eastwood, V. C. Mudera, D. A. McGrouther, and R. A. Brown.  
*Effect of precise mechanical loading on fibroblast populated collagen lattices: Morphological changes.*  
Cell Motility and the Cytoskeleton **40**, 13–21 (1998).
- [27] N. Zaari, P. Rajagopalan, S. K. Kim, and J. Y. Wong.  
*Microgradient mechanically-compliant polyacrylamide gels to probe cell response.*  
Abstracts of Papers of the American Chemical Society **225**, U582–U582 (2003).
- [28] J. L. Tan, J. Tien, D. M. Pirone, D. S. Gray, K. Bhadriraju, and C. S. Chen.  
*Cells lying on a bed of microneedles: An approach to isolate mechanical force.*  
Proceedings of the National Academy of Sciences of the United States of America **100**, 1484–1489 (2003).

- [29] C. S. Chen and J. Tan.  
Private communication (2004).
- [30] M. Riehle, A. Csaderova-Sokolikova, A. MacIntosh, and M. Robertson.  
*Effect of microfabricated surface compliance on cells.*  
Biomaterialien **2** (2003).
- [31] E. Bell, B. Ivarsson, and C. Merrill.  
*Production of a Tissue-Like Structure by Contraction of Collagen Lattices by Human-Fibroblasts of Different Proliferative Potential In vitro.*  
Proceedings of the National Academy of Sciences of the United States of America **76**, 1274–1278 (1979).
- [32] K. Takakuda and H. Miyairi.  
*Tensile behaviour of fibroblasts cultured in collagen gel.*  
Biomaterials **17**, 1393–1397 (1996).
- [33] M. Dembo, T. Oliver, A. Ishihara, and K. Jacobson.  
*Imaging the traction stresses exerted by locomoting cells with the elastic substratum method.*  
Biophysical Journal **70**, 2008–2022 (1996).
- [34] M. Dembo and Y. L. Wang.  
*Stresses at the cell-to-substrate interface during locomotion of fibroblasts.*  
Biophysical Journal **76**, 2307–2316 (1999).
- [35] B. Geiger and A. Bershadsky.  
*Assembly and mechanosensory function of focal contacts.*  
Current Opinion in Cell Biology **13**, 584–592 (2001).
- [36] B. Geiger, A. Bershadsky, R. Pankov, and K. M. Yamada.  
*Transmembrane extracellular matrix-cytoskeleton crosstalk.*  
Nature Reviews Molecular Cell Biology **2**, 793–805 (2001).
- [37] U. S. Schwarz, N. Q. Balaban, D. Riveline, A. Bershadsky, B. Geiger, and S. A. Safran.  
*Calculation of forces at focal adhesions from elastic substrate data: The effect of localized force and the need for regularization.*  
Biophysical Journal **83**, 1380–1394 (2002).
- [38] J. Howard.  
*Mechanics of motor proteins and the cytoskeleton.*  
Sinauer Associates, Sunderland, Massachusetts (2001).
- [39] E. Zamir, M. Katz, Y. Posen, N. Erez, K. M. Yamada, B. Z. Katz, S. Lin, D. C. Lin, A. Bershadsky, Z. Kam, and B. Geiger.

- Dynamics and segregation of cell-matrix adhesions in cultured fibroblasts.*  
Nature Cell Biology **2**, 191–196 (2000).
- [40] N. Wang, J. P. Butler, and D. E. Ingber.  
*Mechanotransduction across the Cell-Surface and through the Cytoskeleton.*  
Science **260**, 1124–1127 (1993).
- [41] M. E. Chicurel, C. S. Chen, and D. E. Ingber.  
*Cellular control lies in the balance of forces.*  
Current Opinion in Cell Biology **10**, 232–239 (1998).
- [42] C. G. Galbraith and M. P. Sheetz.  
*Forces on adhesive contacts affect cell function.*  
Current Opinion in Cell Biology **10**, 566–571 (1998).
- [43] S. Huang and D. E. Ingber.  
*The structural and mechanical complexity of cell-growth control.*  
Nature Cell Biology **1**, E131–E138 (1999).
- [44] E. Cukierman, R. Pankov, and K. M. Yamada.  
*Cell interactions with three-dimensional matrices.*  
Current Opinion in Cell Biology **14**, 633–639 (2002).
- [45] H. Wagner and H. Horner.  
*Elastic Interaction and Phase-Transition in Coherent Metal-Hydrogen Systems.*  
Advances in Physics **23**, 587–637 (1974).
- [46] K. H. Lau and W. Kohn.  
*Elastic Interaction of 2 Atoms Adsorbed on a Solid-Surface.*  
Surface Science **65**, 607–618 (1977).
- [47] S. A. Safran and D. R. Hamann.  
*Long-Range Elastic Interactions and Staging in Graphite-Intercalation Compounds.*  
Physical Review Letters **42**, 1410–1413 (1979).
- [48] U. S. Schwarz and S. A. Safran.  
*Elastic interactions of cells.*  
Physical Review Letters **88**, 048102 (2002).
- [49] T. Vicsek, A. Czirok, E. Benjacob, I. Cohen, and O. Shochet.  
*Novel Type of Phase-Transition in a System of Self-Driven Particles.*  
Physical Review Letters **75**, 1226–1229 (1995).
- [50] F. Schweitzer, W. Ebeling, and B. Tilch.  
*Complex motion of Brownian particles with energy depots.*  
Physical Review Letters **80**, 5044–5047 (1998).

- [51] G. F. Oster, J. D. Murray, and A. K. Harris.  
*Mechanical Aspects of Mesenchymal Morphogenesis.*  
Journal of Embryology and Experimental Morphology **78**, 83–125  
(1983).
- [52] V. H. Barocas and R. T. Tranquillo.  
*An anisotropic biphasic theory of tissue-equivalent mechanics: The  
interplay among cell traction, fibrillar network deformation, fibril  
alignment, and cell contact guidance.*  
Journal of Biomechanical Engineering-Transactions of the ASME **119**,  
137–145 (1997).
- [53] I. B. Bischofs and U. S. Schwarz.  
*Cell organization in soft media due to active mechanosensing.*  
Proceedings of the National Academy of Sciences of the United States  
of America **100**, 9274–9279 (2003).
- [54] I. B. Bischofs, S. A. Safran, and U. S. Schwarz.  
*Elastic interactions of active cells with soft materials.*  
Physical Review E **69**, 021911 (2004).
- [55] R.-P. Hirsekorn and R. Siems.  
*Long-range interaction of point defects with arbitrary dipole tensors.*  
Zeitschrift für Physik B - Condensed Matter **40**, 311–319 (1981).
- [56] L. Landau and E. Lifshitz.  
*Theory of elasticity*, volume 7.  
Third edition. Butterworth-Heinemann, Oxford (1999).
- [57] R. Siems.  
*Mechanical interactions of point defects.*  
Physica Status Solidi **30**, 645–658 (1968).
- [58] A. Love.  
*A treatise on the mathematical theory of elasticity.*  
Dover Publications, New York (1944).
- [59] S. Ramaswamy, J. Toner, and J. Prost.  
*Nonequilibrium fluctuations, travelling waves, and instabilities in active  
membranes.*  
Physical Review Letters **84**, 3494–3497 (2000).
- [60] P. Lenz, J. F. Joanny, F. Julicher, and J. Prost.  
*Membranes with rotating motors.*  
Physical Review Letters **91**, 108104 (2003).
- [61] R. A. Simha and S. Ramaswamy.  
*Hydrodynamic fluctuations and instabilities in ordered suspensions of  
self-propelled particles.*

- Physical Review Letters **89**, 058101 (2002).
- [62] J. P. Butler, I. M. Tolic-Norrelykke, B. Fabry, and J. J. Fredberg.  
*Traction fields, moments, and strain energy that cells exert on their surroundings.*  
American Journal of Physiology-Cell Physiology **282**, C595–C605 (2002).
- [63] R. Mindlin.  
*Force at a point in the interior of a semi-infinite solid.*  
Physics **7**, 195–202 (1936).
- [64] G. Giannone, G. Jiang, D. H. Sutton, D. R. Critchley, and M. P. Sheetz.  
*Talin1 is critical for force-dependent reinforcement of initial integrin-cytoskeleton bonds but not tyrosine kinase activation.*  
Journal of Cell Biology **163**, 409–419 (2003).
- [65] C. G. Galbraith, K. M. Yamada, and M. P. Sheetz.  
*The relationship between force and focal complex development.*  
Journal of Cell Biology **159**, 695–705 (2002).
- [66] S. Munevar, Y. L. Wang, and M. Dembo.  
*Regulation of mechanical interactions between fibroblasts and the substratum by stretch-activated  $Ca^{2+}$  entry.*  
Journal of Cell Science **117**, 85–92 (2004).
- [67] K. Hayakawa, H. Tatsumi, and M. Sokabe.  
*Mechanical stress in the actin cytoskeleton activates SA channels in the vicinity of focal adhesions in endothelial cells.*  
Molecular Biology of the Cell **13**, 340A–340A (2002).
- [68] Y. Sawada and M. P. Sheetz.  
*Force transduction by Triton cytoskeletons.*  
Journal of Cell Biology **156**, 609–615 (2002).
- [69] C. Ballestrem, B. Hinz, B. A. Imhof, and B. Wehrle-Haller.  
*Marching at the front and dragging behind: differential alpha-V beta 3-integrin turnover regulates focal adhesion behavior.*  
Journal of Cell Biology **155**, 1319–1332 (2001).
- [70] D. Tsuruta, M. Gonzales, S. B. Hopkinson, C. Otey, S. Khuon, R. D. Goldman, and J. C. R. Jones.  
*Microfilament-dependent movement of the beta 3 integrin subunit within focal contacts of endothelial cells.*  
FASEB Journal **16** (2002).
- [71] F. G. Giancotti.  
*A structural view of integrin activation and signaling.*

- Developmental Cell **4**, 149–151 (2003).
- [72] R. O. Hynes.  
*Integrins: Bidirectional, allosteric signaling machines.*  
Cell **110**, 673–687 (2002).
- [73] K. A. DeMali, C. A. Barlow, and K. Burridge.  
*Recruitment of the Arp2/3 complex to vinculin: coupling membrane protrusion to matrix adhesion.*  
Journal of Cell Biology **159**, 881–891 (2002).
- [74] A. P. Gilmore and K. Burridge.  
*Regulation of vinculin binding to talin and actin by phosphatidyl-inositol-4-5-bisphosphate.*  
Nature **381**, 531–535 (1996).
- [75] V. Martel, C. Racaud-Sultan, S. Dupe, C. Marie, F. Paulhe, A. Galmiche, M. R. Block, and C. Albiges-Rizo.  
*Conformation, localization, and integrin binding of talin depend on its interaction with phosphoinositides.*  
Journal of Biological Chemistry **276**, 21217–21227 (2001).
- [76] J. D. Bjorge, A. Jakymiw, and D. J. Fujita.  
*Selected glimpses into the activation and function of Src kinase.*  
Oncogene **19**, 5620–5635 (2000).
- [77] G. von Wichert, G. Y. Jiang, A. Kostic, K. De Vos, J. Sap, and M. P. Sheetz.  
*RPTP- $\alpha$  acts as a transducer of mechanical force on  $\alpha(v)/\beta(3)$ -integrin-cytoskeleton linkages.*  
Journal of Cell Biology **161**, 143–153 (2003).
- [78] H. B. Wang, M. Dembo, S. K. Hanks, and Y. L. Wang.  
*Focal adhesion kinase is involved in mechanosensing during fibroblast migration.*  
Proceedings of the National Academy of Sciences of the United States of America **98**, 11295–11300 (2001).
- [79] A. D. Bershadsky, N. Q. Balaban, and B. Geiger.  
*Adhesion-dependent cell mechanosensitivity.*  
Annual Review of Cell and Developmental Biology **19**, 677–695 (2003).
- [80] G. Giannone, B. J. Dubin-Thaler, H. G. Döbereiner, N. Kieffer, A. R. Bresnick, and M. P. Sheetz.  
*Periodic lamellipodial contractions correlate with rearward actin waves.*  
Cell **116**, 431–443 (2004).
- [81] H. Döbereiner, B. J. Dubin-Thaler, G. Giannone, H. Xenias, and M. P. Sheetz.

- Dynamic Phase Transitions in Cell Spreading.*  
q-bio/0405008v1 (2004).
- [82] J. V. Small, B. Geiger, I. Kaverina, and A. Bershadsky.  
*How do microtubules guide migrating cells?*  
Nature Reviews Molecular Cell Biology **3**, 957–964 (2002).
- [83] I. Kaverina, O. Krylyshkina, K. Beningo, K. Anderson, Y. L. Wang,  
and J. V. Small.  
*Tensile stress stimulates microtubule outgrowth in living cells.*  
Journal of Cell Science **115**, 2283–2291 (2002).
- [84] G. I. Bell.  
*Models for Specific Adhesion of Cells to Cells.*  
Science **200**, 618–627 (1978).
- [85] T. Erdmann and U. S. Schwarz.  
*Stability of adhesion clusters under constant force.*  
Physical Review Letters **92**, 108102 (2004).
- [86] T. Bickel and R. Bruinsma.  
*Focal adhesions: Physics of a Biological Mechano-sensor.*  
Preprint, cond-mat/0306116v1 (2003).
- [87] A. Nicolas and S. Safran.  
*Elastic deformations of grafted layers with surface stress.*  
Physical Review E **69**, 051902 (2004).
- [88] A. Nicolas, B. Geiger, and S. Safran.  
*Cell mechanosensitivity controls the anisotropy of focal adhesions.*  
to appear in Proceedings of the National Academy of Sciences of the  
United States of America (2004).
- [89] G. Y. Jiang, G. Giannone, D. R. Critchley, E. Fukumoto, and M. P.  
Sheetz.  
*Two-piconewton slip bond between fibronectin and the cytoskeleton  
depends on talin.*  
Nature **424**, 334–337 (2003).
- [90] T. Erdmann and U. S. Schwarz.  
*Adhesion clusters under shared linear loading: a stochastic analysis.*  
Europhysics Letters **66**, 603–609 (2004).
- [91] R. Ananthakrishnan.  
*On the Structural Response of Eukaryotic Cells.*  
Ph.D. thesis, University of Texas at Austin (2003).
- [92] P. C. Dartsch and H. Hammerle.  
*Orientation Response of Arterial Smooth-Muscle Cells to Mechanical  
Stimulation.*

- European Journal of Cell Biology **41**, 339–346 (1986).
- [93] J. H. C. Wang and E. S. Grood.  
*The strain magnitude and contact guidance determine orientation response of fibroblasts to cyclic substrate strains.*  
Connective Tissue Research **41**, 29–36 (2000).
- [94] C. Neidlinger-Wilke, E. S. Grood, J. H. C. Wang, R. A. Brand, and L. Claes.  
*Cell alignment is induced by cyclic changes in cell length: studies of cells grown in cyclically stretched substrates.*  
Journal of Orthopaedic Research **19**, 286–293 (2001).
- [95] K. Naruse, X. Sai, N. Yokoyama, and M. Sokabe.  
*Uni-axial cyclic stretch induces c-src activation and translocation in human endothelial cells via SA channel activation.*  
Febs Letters **441**, 111–115 (1998).
- [96] J. Jackson.  
*Klassische Elektrodynamik.*  
Second edition. de Gruyter, Berlin (1982).
- [97] N. Phan-Thien.  
*On the image system for the Kelvin-state.*  
Journal of Elasticity **13**, 231–235 (1983).
- [98] L. Walpole.  
*An elastic singularity in joined half-spaces.*  
International Journal of Engineering Science **34**, 629–638 (1996).
- [99] F. Grinnell.  
*Fibroblast-collagen-matrix contraction: growth-factor signalling and mechanical loading.*  
Trends in Cell Biology **10**, 362–365 (2000).
- [100] A. Edmonds.  
*Angular momentum in quantum mechanics.*  
Third edition. Princeton University Press, Princeton, N.J. (1974).
- [101] A. G. Moon and R. T. Tranquillo.  
*Fibroblast-Populated Collagen Microsphere Assay of Cell Traction Force .1. Continuum Model.*  
Aiche Journal **39**, 163–177 (1993).
- [102] V. H. Barocas and R. T. Tranquillo.  
*A finite element solution for the anisotropic biphasic theory of tissue equivalent mechanics: The effect of contact guidance on isometric cell traction measurement.*

- Journal of Biomechanical Engineering-Transactions of the ASME **119**, 261–268 (1997).
- [103] T. S. Girtan, V. H. Barocas, and R. T. Tranquillo.  
*Confined compression of a tissue-equivalent: Collagen fibril and cell alignment in response to anisotropic strain.*  
Journal of Biomechanical Engineering-Transactions of the ASME **124**, 568–575 (2002).
- [104] J. T. H. Mandeville, M. A. Lawson, and F. R. Maxfield.  
*Dynamic imaging of neutrophil migration in three dimensions: Mechanical interactions between cells and matrix.*  
Journal of Leukocyte Biology **61**, 188–200 (1997).
- [105] J. J. Weis and D. Levesque.  
*Chain Formation in Low-Density Dipolar Hard-Spheres - a Monte-Carlo Study.*  
Physical Review Letters **71**, 2729–2732 (1993).
- [106] T. Tlusty and S. A. Safran.  
*Defect-induced phase separation in dipolar fluids.*  
Science **290**, 1328–1331 (2000).
- [107] S. Vanni, B. C. Lagerholm, C. Otey, D. L. Taylor, and F. Lanni.  
*Internet-Based image analysis quantifies contractile behavior of individual fibroblasts inside model tissue.*  
Biophysical Journal **84**, 2715–2727 (2003).
- [108] P. B. Allen.  
*Dipole interactions and electrical polarity in nanosystems: The Clausius-Mossotti and related models.*  
Journal of Chemical Physics **120**, 2951–2962 (2004).
- [109] P. B. Allen.  
*Dipole Interactions in Nanosystems.*  
cond-mat/0309392v1 (2004).
- [110] E. Madelung.  
Physikalische Zeitschrift **XIX**, 524 (1918).
- [111] C. Pozrikidis.  
*Introduction to theoretical and computational fluid dynamics.*  
Oxford University Press, New York (1997).
- [112] C. S. Chen, M. Mrksich, S. Huang, G. M. Whitesides, and D. E. Ingber.  
*Geometric control of cell life and death.*  
Science **276**, 1425–1428 (1997).

- [113] K. K. Parker, A. L. Brock, C. Brangwynne, R. J. Mannix, N. Wang, E. Ostuni, N. A. Geisse, J. C. Adams, G. M. Whitesides, and D. E. Ingber.  
*Directional control of lamellipodia extension by constraining cell shape and orienting cell tractional forces.*  
FASEB Journal **16**, 1195–1204 (2002).
- [114] A. Brock, E. Chang, C. C. Ho, P. LeDuc, X. Y. Jiang, G. M. Whitesides, and D. E. Ingber.  
*Geometric determinants of directional cell motility revealed using microcontact printing.*  
Langmuir **19**, 1611–1617 (2003).
- [115] S. W. de Leeuw, J. W. Perram, and E. R. Smith.  
*Simulation of Electrostatic Systems in Periodic Boundary-Conditions .1. Lattice Sums and Dielectric-Constants.*  
Proceedings of the Royal Society of London Series A-Mathematical Physical and Engineering Sciences **373**, 27–56 (1980).
- [116] S. W. de Leeuw, J. W. Perram, and E. R. Smith.  
*Simulation of Electrostatic Systems in Periodic Boundary-Conditions 2. Equivalence of Boundary-Conditions.*  
Proceedings of the Royal Society of London Series A-Mathematical Physical and Engineering Sciences **373**, 57–66 (1980).
- [117] S. Ismail-Beigi and T. A. Arias.  
*Ab initio study of screw dislocations in Mo and Ta: A new picture of plasticity in bcc transition metals.*  
Physical Review Letters **84**, 1499–1502 (2000).
- [118] A. J. C. Ladd.  
*Monte-Carlo Simulation of Water.*  
Molecular Physics **33**, 1039–1050 (1977).
- [119] H. Y. Wang and R. Lesar.  
 *$O(N)$  Algorithm for Dislocation Dynamics.*  
Philosophical Magazine A-Physics of Condensed Matter Structure Defects and Mechanical Properties **71**, 149–164 (1995).
- [120] D. Drasdo, R. Kree, and J. S. McCaskill.  
*Monte-Carlo Approach to Tissue-Cell Populations.*  
Physical Review E **52**, 6635–6657 (1995).
- [121] D. A. Beysens, G. Forgacs, and J. A. Glazier.  
*Cell sorting is analogous to phase ordering in fluids.*  
Proceedings of the National Academy of Sciences of the United States of America **97**, 9467–9471 (2000).

- [122] M. Allen and D. Tildesley.  
*Computer Simulations of Liquids*.  
Oxford University Press, Oxford (2001).
- [123] E. R. Grannan, M. Randeria, and J. P. Sethna.  
*Low-Temperature Properties of a Model Glass*.  
Physical Review Letters **60**, 1402–1405 (1988).
- [124] P. de Gennes and J. Prost.  
*The Physics of Liquid Crystals*.  
Second edition. Oxford University Press, Oxford (1995).
- [125] H. Weber, D. Marx, and K. Binder.  
*Melting Transition in 2 Dimensions - a Finite-Size-Scaling Analysis of Bond-Orientational Order in Hard Disks*.  
Physical Review B **51**, 14636–14651 (1995).
- [126] R. B. Dickinson.  
*A generalized transport model for biased cell migration in an anisotropic environment*.  
Journal of Mathematical Biology **40**, 97–135 (2000).
- [127] D. Bray.  
*Cell movements: from molecules to motility*.  
Second edition. Garland, New York (2001).
- [128] P. Chaikin and T. Lubensky.  
*Principles of condensed matter physics*.  
Cambridge University Press, Cambridge (1995).
- [129] J. J. Weis, D. Levesque, and G. J. Zarragoicoechea.  
*Orientational Order in Simple Dipolar Liquid-Crystal Models*.  
Physical Review Letters **69**, 913–916 (1992).



# Acknowledgements

Many people have contributed to this work—both directly and indirectly—and it is my great pleasure to thank all of them at this point. Special thanks to

- Ulrich Schwarz for much more than being a great advisor, for his strong support and encouragement, for the opportunities to meet people and go to conferences, for arranging and supporting my experimental "intermezzo" at Leipzig University. Thanks for teaching and for learning together about physics and biology. It was fun!
- Professor Lipowsky for much more than the opportunity to become a member of the MPI theory division and for organizing such an excellent interdisciplinary graduate student program in the framework of the IMPRS. This work benefited a lot from all the interesting lectures and classes taken there.
- my M.A. advisor Professor Phil Allen at SUNY Stony Brook, for much more than continuing to be a great advisor, for keeping me updated about the condensed matter physics community, for the financial support for the APS March meeting and for EPENS in 2002, for the ongoing interest in my work and the immediate support whenever I need it. It is a pleasure to thank Phil for his direct contribution to this work by drawing my attention to his recent papers on electric dipoles in nano-systems during a beautifully organized visit at NY in 2004.
- Professor Josef Käs for much more than hosting me for the summer term 2003 in his lab at Leipzig University, for generous support and great advice. I learned a lot about experimental techniques in biological physics both "hands-on" and by watching, especially the BONG-people. I would like to thank in particular Jens Gerdemann for teaching me how to do cell culture, and for learning together about fibroblasts on PAAM-substrates.
- Professor Martin Bastmeyer and Dirk Lehmann from the University of Jena for much more than a fruitful collaboration.

- Professor Alexander Bershadsky from the Weizmann Institute for much more than a private lesson on signaling at focal adhesions during a train trip from Potsdam to a conference at Rostock in 2002.
- Professor Micheal Sheetz for much more than answering my questions on reinforcement during a meeting at Dresden in 2003, for inviting me to his lab, for an awesome day at Columbia University and the opportunity to meet his lab members. Special thanks to Hans Günther Döbereiner and Gregory Giannone for interesting discussions about ongoing work.
- Professor Joyce Wong for much more than organizing a beautiful stay at her lab at Boston University in February 2004, for interesting discussions about durotaxis, for sharing results and sending preprints.
- Professor Don Ingber at Harvard University and Professor Christopher Chen at Johns Hopkins University for much more than giving me the opportunity to visit their labs and discuss with their lab members in particular Amy Brock and John Tan about their respective PhD-work.
- Professor Dale Kaiser for much more than a fun day at Stanford and a great discussion about the similarities and differences between mechanotaxis of animal cells and elasticotaxis of bacteria.
- my colleagues at the MPI in Potsdam, in particular Thomas Gruhn, Jan Kierfeld, Gunnar Linke, Stefan Klumpp, Thorsten Erdmann and Christian Korn, for much more than discussions and criticism. Thanks to Marc Nolte for collaborating on the “Leipzig” project, and to Conny Sinn and Antje Reinecke for help in the lab.
- my office mates Alberto Imperato, Meshfin Ashfaw and Karin Riske and the lunch-and-coffee group, Ulrich, Jan, Thomas, Stefan, Nicole, Christian, Andreas, Gunnar for much more than the “social time” of the day. Special thanks to Gunnar Linke for frequent early morning tea-and-breakfast discussions. Thanks also to Gregoria and Ourida for practicing violine and doing some sports with me once in a while.
- my best friend Yvonne for much more than nice discussions about biology and physics and a great friendship.
- my family, especially my mum and Theo, my twin-brothers Chrissie and Thom(y) and my dad, for much more than their love.
- Thomas for much more than an awesome time, despite the weekly commute between Potsdam and Würzburg, for being patient when I got too enthusiastic about “meine Zellen”, for the great discussions also about this work and for everything else than cannot be expressed in words.